Integrated Disposable Microfluidic Tissue Chips

by

Duncan Allison O'Boyle

Submitted to the Department of Mechanical Engineering
in partial fulfillment of the requirements for the degree of

Master of Science in Mechanical Engineering

at the

MASSACHUSETTS INSTITUTE OF TECHNOLOGY

June 2021

Author .....
Department of Mechanical Engineering
May 14, 2021

Certified by .....
David L. Trumper
Professor, Mechanical Engineering
Thesis Supervisor

Certified by .....
Linda Griffith
School of Engineering Professor of Teaching Innovation, Biological Engineering, and Mechanical Engineering
Thesis Supervisor

Accepted by .....
Nicolas G. Hadjiconstantinou
Chair, Graduate Program Committee

Integrated Disposable Microfluidic Tissue Chips

by

Duncan Allison O'Boyle

Submitted to the Department of Mechanical Engineering
on May 14, 2021, in partial fulfillment of the
requirements for the degree of
Master of Science in Mechanical Engineering

Abstract

This thesis presents the design, implementation, and testing of a new platform for mimicking a wide range of physiological conditions using multi-layer thermoplastic microfluidic chips with integrated elastomeric membranes. The new platform is designed for high-throughput experiments, using disposable thermoplastic chips, and enabling precise control of channel pressures and flowrates. The platform can distribute up to 7 pneumatic signals to 4 microfluidic chips for control of high-throughput experiments in the incubator or on a microscope. The disposable chips are made entirely of Cyclic Olefin Copolymers (COC) and utilize on-chip pumps, pressure regulators, microfluidic accumulators, a novel hydrogel tissue compartment, and a standardized pneumatic interconnect. Channel flowrates are adjustable between 0-3 μL/s and pressures can be controlled up to 2 psi. The 5-layer chips are bonded together using a thin film COC elastomer membrane. The top and bottom layers are laminated using a co-extruded COC film with an easy-to-bond interface. Novel methods for reliable fabrication of these devices are explored, including laser machining of frozen membranes, and infrared bonding in a vacuum chamber. The chips are optically clear, exhibit strong thermal bonds, and display significantly lower levels of hormone absorption than earlier polydimethylsiloxane (PDMS) based devices. The design and analysis of the platform is described in detail, and the biological performance of the system is validated in studies promoting vasculogenesis in a co-culture of endothelial and stromal cells.

Thesis Supervisor: David L. Trumper
Title: Professor, Mechanical Engineering

Thesis Supervisor: Linda Griffith
Title: School of Engineering Professor of Teaching Innovation, Biological Engineering, and Mechanical Engineering

Acknowledgments

I would like to thank Linda Griffith and David Trumper for their support and vision on this project. I am thankful for all of the hours we spent in design reviews and for their mentorship to my personal growth and development. I want to express my gratitude to the MIT Department of Mechanical Engineering, the NIH Tissue Chips Program, and CN Bio Innovations for sponsoring this project. Special thanks to Alex Brown, Juan Gnecco, Ellen Kan, Clara Ives, and the rest of the Endometrium Team for their time and effort with brainstorming sessions and lab experiments. Thank you Allison Lenhard for helping set up experiments, assisting in device fabrication, and making long weeks in the lab more enjoyable. Thank you to Raphael Zonis for talking through wild ideas and brainstorming better ways of doing things. Thanks to Hsinhwa Lee and Tom Donaghey for all of their help around the lab and to all of the Griffith Lab members who have made this such a positive experience.

Thanks to my awesome parents for their love and support and to my brother for all of the encouragement he has provided over the years. I want to thank my friends for all of the outdoor adventures, lockdown phone calls, and lasting memories.

Contents

List of Figures

List of Tables

Chapter 1

Introduction

This thesis describes the need for a new integrated platform for culturing human-derived tissues with precise fluidic control of physiological conditions and processes. The design, implementation, and testing of this new device are presented. This system is able to simultaneously control 4 microfluidic chips with integrated pneumatic pumps, pressure regulators, and a novel hydrogel tissue compartment for vascularization of tissues *in vitro*. The significant contributions of this work include: (1) new materials for reliable boding of multi-layer microfluidic chips with integrated elastomeric features (2) the design of optimized pumps, valves, accumulators, and on-chip pressure regulators for reliable fluidic control (3) a standardized chip format and manifold for running experiments in the incubator and at the microscope (4) and a system configuration adaptable for high-throughput by running many devices simultaneously.

This chapter provides a background on the current state of microphysiological systems developed in academic labs as well as commercially available platforms. Platforms with active and passive fluidic controls will be discussed, and particular attention to the materials of these platforms will be provided.

1.1 Microphysiological Systems

Recent advances in the fields of cellular biology, microfabrication, and microfluidics have enabled the development of advanced microphysiological systems that mimic the behavior of human organs in an *in vitro* environment. These systems use precisely controlled fluidics to culture human derived tissues under complex conditions. These conditions include but are not limited to hormonal treatments, drug therapies, and mechanical stimulation [1, 2]. MPS platforms have gathered widespread attention in academic labs, pharmaceutical industries, and by government institutions such as the NIH, NSF, and FDA. A microphysiological system (MPS) is a system that recapitulates the core functions and cellular mechanics of an organ found *in vivo*. A subset of these systems with smaller fluid volumes are called Organs-on-a-Chip, or OOC, for short. The main advantage of these platforms is that they allow researchers to answer fundamental research questions in a human-derived system. Although mouse models can be used to study many biological processes, they are not always an accurate analogue to a human tissue [3].

MPS systems can be used to study individual tissues such as liver, gut, and kidney tissue, but may also be used to study the combined effects of multi-organ systems. For example, the interactions of gut and liver tissues on an MPS platform has been studied to gain insights into the function of cross-tissue communication pathways on inflammatory response [4]. These types of studies are based on physiologically relevant metabolic profiles and fluidic conditions and are intended to match the function of real human organs [5]. The results of these advanced *in vitro* studies can be then be scaled and translated into useful insights for pharmacological applications [6].

A subset of microphysiological studies involves replicating the microvascular structures of living tissues in a hydrogel based microfluidic system [7]. These microvessels are generated in an *in vitro* system using from human-derived enothelial cells and stromal cells. The most common combination of cell types is co-culture of Human Umbilical Vein Endothelial Cells (HUVECs) and Normal Human Lung Fibroblasts (NHLFs). Fibrin is typically used as an extracellular matrix for these models be-

cause it is a soft, permeable, and human-derived scaffold that has been validated in many microvasculature studies. Other materials, such as PEG-based hydrogels, are being developed to promote vascular network formation using specifically engineered polymers that can be customized for a given tissue or biological model [8].

Ideally, the microfluidic platform should closely match the pulsatility and shear stress conditions of the fluidic conditions found *in vivo*. Many advances in Organ-on-a-Chip technologies, such as new materials, fluidic interconnects, and integrated sensors, help to build more advanced systems that can help to create these conditions [9]. Despite these advances, generating the exact conditions for vasculogenesis can be difficult due to hardware-related limitations. Providing predictable flowrates and pressures to a reliable tissue compartment is a significant challenge and very few integrated platforms come close to replicating the optimal conditions for vasculogenesis [10].

1.2 Platform Overview

The design of a user-friendly and mechanically robust platform for controlling and interfacing with microfluidic chips is central to the aims of this thesis. This platform could be used to accurately control physiological conditions *in vitro* and create a path forward for high-throughput microvascular studies. The ideal Organ-on-a-Chip platform should meet the following criteria:

1. **Compact Form Factor**

   The platform should be small enough that it is easy to handle and carry around the lab. A small footprint also enables a user to run more platforms at a time due to the limited space claim, and helps to reduce the cost of materials.

2. **Microscope Compatible**

   The device should be compatible with most standard lab microscopes. The platform should be easy to mount on the microscope and should be able to be controlled during imaging. The chips should be optically transmissive, and

the platform should not generate optical noise for fluorescent imaging. The platform should not get in the way of the microscope objectives or limit the functionality of the microscope in any way.

3. **High-Throughput**

   Multiple chips should be able to be controlled on an individual platform. This enables high throughput experiments and the ability to design experiments with proper control conditions.

4. **Pneumatic Interconnects**

   Pneumatic interconnects should be provided so that chips may be controlled using pneumatic signals. This is particularly true for chips featuring pneumatic pumps, but may also be true for chips with pressure regulators, pressurized reservoirs, gas exchangers, and heating or cooling systems. This criteria includes the need for a pneumatic connection from the platform to the pneumatic controls as well as a connection from the platform to the individual chips.

5. **Sterile and Disposable Chips**

   The chips should be sterile and disposable so that experiments can be ran without contamination issues from previous experiments. Ideally, the chips feature integrated control features, such as pumps and valves, that can be thrown away at the end of an experiment.

6. **Accommodates New Chip Designs**

   The system should have a standardized interface for connecting to new chips designs. This allows designers to focus on the chip without having to re-consider the chip-to-world connections. This speeds up future chip development and adds to the perceived value of the platform.

Based on this platform design criteria a 4-chip manifold was selected as the platform form-factor. The platform features 7 pneumatic inputs, an aluminum base plate, a low-profile manifold, and a standardized geometry for interfacing with microfluidic

chips. **Figure 1-1** highlights the size and layout of this platform with 4 chips connected to the manifold.

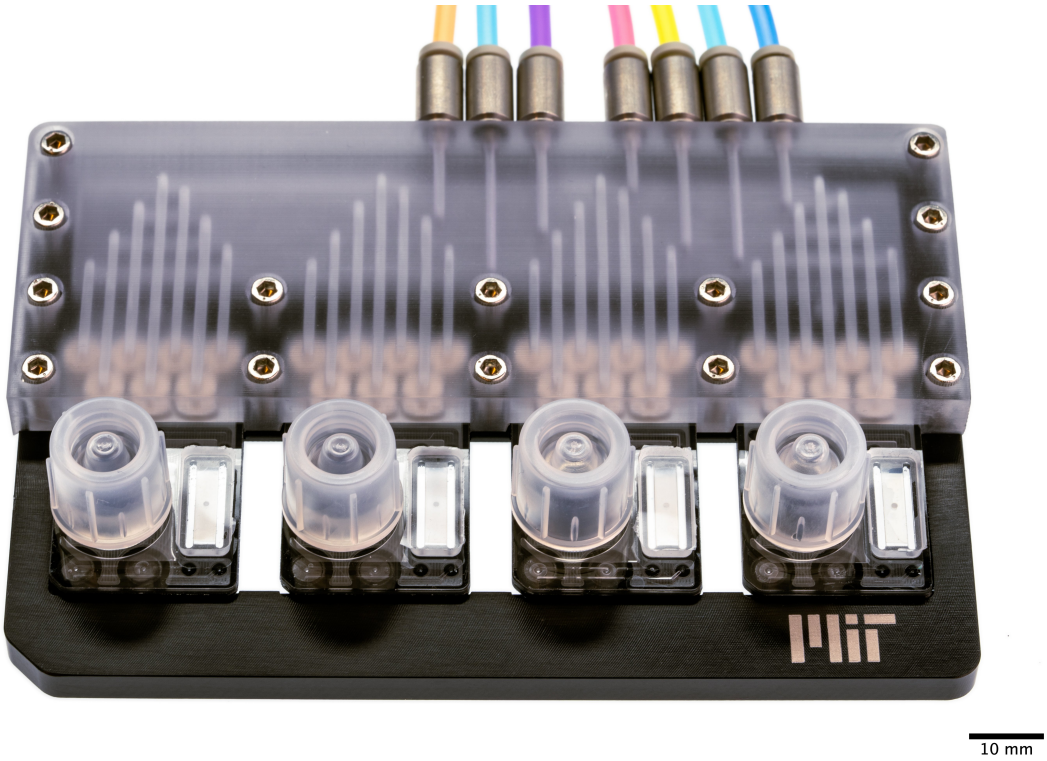

Figure 1-1: A finalized prototype of a manifold that connects 4 microfluidic chips to 7 pneumatic signals.

1.3 Commercial Systems

Many commercially available MPS systems exist, but most of these systems are cost prohibitive, difficult to use, or lack proper biological validation. For widespread adoption, these types of plug-and-play experimental platforms need to be carefully studied and rigorously validated so that they can offer translatable results across research labs.

One commercially available system that meets many of the key requirements for a translatable MPS research platform is CNBio's PhysioMimix (pictured in **Figure 1-2**). The system features 3 individual platforms, onboard pumps, a pneumatic control unit, and easy to use transwell inserts. The platforms can connect and disconnect from the control unit for sampling and analysis and fit most 96-well plate adapters.

The platforms are assembled using a Polysulfone fluidic layer and a PMMA pneumatic manifold that is clamped to a biocompatible elastomeric membrane. The system does have a few downsides. First, the system and its consumables are very expensive and may be cost prohibitive for many academic labs. Second, the unit takes up significant space in the incubator, limiting the device throughput. Lastly, the devices are not image friendly and cannot be observed on a traditional lab microscope.

Figure 1-2: CN-Bio's PhysioMimix microphysiological system (cn-bio.com).

Simpler systems may not have the ability to match exact physiological flow profiles, but may enable higher throughput experiments. The AIM Biotech Chip provides a hydrogel-based 3D cell culture environment that is image friendly and can accommodate a wide variety of cell types. The chip works by pinning a hydrogel meniscus between small posts in the tissue compartment. The meniscus then becomes an interface with the media channels. Cell migration into hydrogel scaffolds and vascularized co-cultures have been observed in the devices and have been used to create relevant tissue models [11]. The chips have been used to study the mechanisms for creating angiogenesis in a hydrogel environment, and the system has been used to create microvascular models of the human blood-brain barrier [12, 13]. The chips are useful for building small tissue models, but are not large enough for mimicking multiple organs or larger systems. In addition, the posts limit nutrient transport into

the hydrogel, prohibit the use of hydrogels with large swelling ratios, and prevent microvascular structures from connecting to media channels. The AIM chip also suffers from trapped bubbles under the surface the optical laminate, a quality control issue that is common in off-the-shelf microfluidic chips. These bubbles are pictured in **Figure 1-3**. A similar platform made by Mimetas allows for higher throughput hydrogel-based experiments using a plate-based assay with as many as 96 hydrogel channels per plate. The devices are bonded together using laser welding, feature phaseguides for constraining the hydrogel, and utilize a rocker plate for generating cyclical flow profiles in the media channels [14].

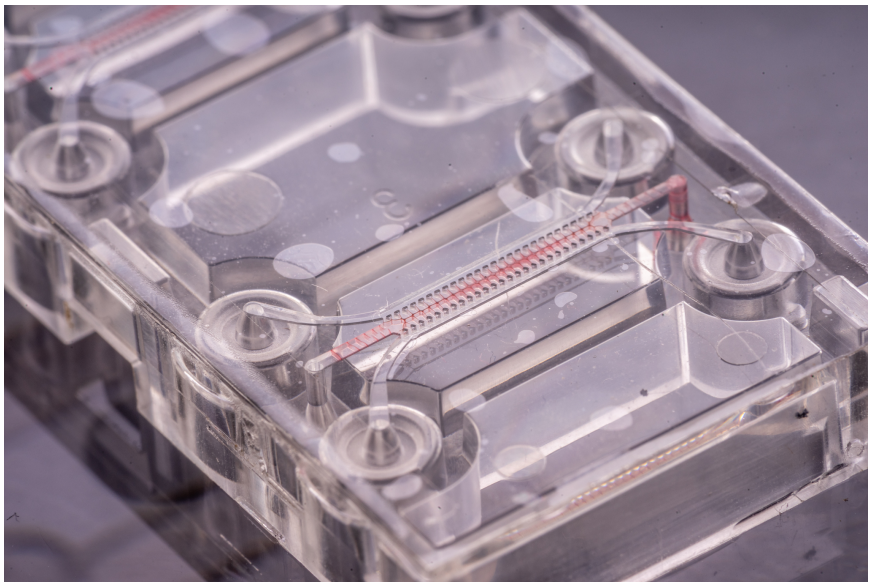

Figure 1-3: Bottom side of the AIM Biotech chip.

Emulate Bio is developing more advanced systems with integrated flow control in PDMS-based chips with tissue specific scaffolds that can induce mechanical stimuli such as tensile forces from the lung [15]. The chips can be imaged and operated for extended periods of time [16]. For example, the lung specific chip has been used to study therapeutic treatments for Intravascular Thrombosis [17]. Competitive systems, such as those made by Cherry Biotech and Tissuse GmBH, have been used to create pharmacological models of the liver, heart, and skin for use in drug development [18].

1.3.1 Challenges with Organ-on-a-Chip Systems

Despite the availability of several commercial systems to choose from, researchers still run into many challenges with Organ-on-a-Chip systems [19]. Namely, there are a number of hardware and instrumentation related challenges with designing, fabricating, and measuring the performance of OOC platforms [20]. These challenges can be organized into three main categories: replication of physiological fluidic conditions, designing a sterile and multiplexed platform, and integrating tissues into well-designed scaffolds.

Recirculation of culture media is one of the most important criteria for a successful OOC platform because cells are responsive to shear stress, concentration gradients, pressure differences, fluid convection, and other forms of mechanical stimuli [21]. Proper fluid flow can enhance biological processes such as vascularization of endothelial cells [22]. Pump are usually used to generate fluid flow, but may not always be required to generate appropriate fluidic conditions. For example, a pump-free system has been developed that rotates a vertically oriented chip with two reservoirs to create a gravitationally induced fluid flow between the two reservoirs [23]. Pumps tend to be a favorable option for generating fluid flow because they make it easier to account for media transport and scale fluid flow in a perfusable chip [24]. Many pumps exist for cell culture applications, but are often external devices that require long lengths of tubing, significant counter space, and limit the amount of chips that can be used at a time [25, 26].

External devices also introduce a concern with sterility. Any additional connection, interface, sealing mechanism, or tube presents an opportunity for contaminants to enter the chip or for fluid to leak out [27]. Maintaining sterility is one of the most fundamental steps in building a reliable platform, but best practices are sometimes overlooked [28]. Systems should be designed with easy to use connections that allow the platform controls to be separate from the sterile device, and should be able to integrate into lab automation equipment [29, 28].

Devices must also accommodate a wide variety of tissues, either with general

purpose hydrogels or tissue specific chip designs with well-designed scaffolds. Cell loading mechanisms should be easy to use and allow for different cell types and media formulations [30]. A hydrogel-based device should allow for any hydrogel to be used including PEG, fibrin, and Matrigel. New hydrogels are still being developed, so the tissue compartment needs to accommodate future gel formulations that might swell or restructure over time [31].

1.4 Material Considerations

Most microfluidic devices made in the lab, and some commercial systems, are made using polydimethylsiloxane (PDMS). PDMS has been extremely important in advancing the field of microfluidic studies. The advantages of PDMS is that is is castable, able to reproduce small features, optically clear, elastomeric and easy to seal, and able to covalently bond to glass via UV-ozone treatment. Unfortunately, the material is difficult to mass produce due to complexity of fabrication and quality control. Further, it suffers from diffusion and absorption properties that make it unsuitable for hormone or drug-sensitive cell culture applications. The primary alternative to PDMS as a material for making microfluidic chips is the family of thermoplastic polymers. Thermoplastics are easier to manufacture and more cost effective at scale and offer some of the same benefits as PDMS. Traditionally used in standard cell culture plates, thermoplastics have seen widespread adoption in the microfluidic industry. Commercially available chips are made from a wide variety of materials. This section will describe the advantages of using thermoplastic materials, and specifically cyclic olefin copolymers, for use in advanced microfluidic systems.

1.4.1 Absorption of Small Molecules

One of the main reason to choose a thermoplastic material for microfluidic assays is due to non-specific absorption (molecules diffusing into the bulk polymer material) and adsorption (molecules binding to the surface of the polymer) of small molecules. PDMS has been observed to absorb drugs, hormones, and other small molecules in

microfluidic systems [32], and has been compared extensively to alternative materials such as polycarbonate (PC), polystyrene (PS), poly-methyl-methacrylate (PMMA), and cyclic olefin copolymers (COC) [33]. PDMS also has a propensity to later release absorbed molecules back into solution, making it an unpredictable and unreliable material for sensitive assays involving small molecules. This is particularly true for studies, such as projects in our lab, which involve sex hormone cycles over a period of weeks in an incubator. Thus, it it important to select a material that predominantly experiences surface adsorption rather than bulk polymer absorption.

The effect of surface adsorption can be remedied or accounted for by priming the polymer surface or by providing some sort of surface treatment. This can be done, for example, by priming the surface with BSA so that that surface is initially saturated with bound molecules. More advanced treatments may also be implemented, for example, PDMS has been treated with a Parylene coating to protect proteins from binding in PCR studies [34]. A conformal CVD coating such as Parylene provides a best-case scenario for PDMS, but coatings are usually impermanent on PDMS and unsuitable for long term studies. Like PDMS, thermoplastic materials also suffer from non-specific surface adsorption, but the problem is more predictable, easier to characterize, and well-studied [35]. By tailoring polymer formulations and surface properties, thermoplastics can be optimized for reduced protein adhesion and binding. For example, a custom grade of polyamine was developed to reduce the binding of specific proteins and bacteria [36]. Thermoplastic elastomers should also be carefully tailored to reduce absorption potential. The COC elastomer used in this thesis, SEBS elastomers, TPU, EPDM, and Viton are all worth consideration [37, 38, 39].

Cyclic olefin copolymers make a great alternative to PDMS because they have a less active surface for binding to free molecules and for this reason have been used to develop sensitive oocyte culture platforms and high performance devices for protein separation and biomolecule analysis [33, 40, 41]. When compared to other materials, COC has low-leachable properties and does not release estrogenic compounds like other BPA-free materials [42]. In general, COC shows limited protein adsorption despite it's hydrophobic properties, and these properties can be changed with surface

modification [43]. Surface modification may include UV-ozone treatment, sequential photographting [44], coating with non-covalent DMA-alkyl copolymers [45], and commercially via single-step application of PEG-like polymer solution [46]. Many other techniques, such as treatment with Paryalene may be used depending on the specific application, and cell adhesion may also be improved with the addition of poly-L-lysine or similar tissue culture treatment if necessary [40]. When properly implemented, these techniques make COC a predictable and reliable material for cell culture and biomolecular assays.

1.4.2 Optical Properties

The ideal microfluidic material provides optical clarity across a wide range of wavelengths. The required range for most fluorescent assays falls between 400-700 nm, but some applications require UV and near-IR imaging as well. For this reason it is preferable to select a material that has 90-100% transmission from 280-1100 nm, providing similar optical properties to glass. Autofluorescence should also be considered so that the bulk material and supporting components do not cause noise in images generated on the device. Most commonly, an optical material is used just as a transparent window into a microfluidic device and the rest of the device may be made of materials with reduced optical clarity.

1.4.3 Manufacturing Methods

A successful microfluidic system must be able to meet mass-production demands. PDMS takes time to cure, requires UV-ozone treatment for bonding, involves precise mixing and casting of two-part curable polymers, and is generally easy to damage due to its low modulus. These factors make it very difficult to produce at scale. Thermoplastics are much easier to mass produce because they can be injection molded, roll extruded, hot embossed, or thermoformed. The most difficult step in creating a microfluidic chip is sealing the device with a thin film. In some applications, the additional challenge of joining the chip with a flexible membrane is also presented. For

PDMS devices, this can be accomplished by using UV-ozone to bond glass coverslips and PDMS membranes to the assembly.

The techniques for joining thermoplastics for microfluidic and medical device applications have been widely studied and well-categorized into widely-cited books and review articles [47, 48]. There are many methods that can be used, but they generally fall into four main categories: plasma bonding, solvent bonding, thermal bonding, and adhesive bonding. Thermal bonding may manifest in many different processes including diffusion bonding, laser welding, friction welding, ultrasonic welding, and heat stacking. Plasma bonding can be used to join elastomeric membranes to thermoplastic devices and has even been shown as a viable method for making doormat valves in COC devices [49]. Unfortunately, these bonds are very weak and the application of UV-ozone treatments is not easy to control or automate in an industrial environment. Thus, the three other methods provide more realistic options for making commercially viable devices.

The first alternative to plasma treatment is to join materials using solvent assisted approaches. By prepping a surface with an appropriate solvent it becomes tacky and the molecules become mobile. The surface can be joined to another substrate (treated or not) and the materials will bond. The requirement for this to work is an overlap in solubility between polymer and solvent; in advanced applications an overlap in solubility parameters for different materials can be used to join dissimilar materials. For example, COC can be joined to SEBS elastomers with an appropriate solvent mixture [50]. Solvents should be evenly distributed onto a surface so that the amount of solvent dissolved into the polymer is kept at a minimum and allowed to escape after bonding [51]. To promote solvent evacuation, smaller exposed surfaces and grooves may be used to evacuate solvent from the device [52]. Solvent may be applied by vapor to generate strong bonds with the added benefit of vapor polishing to reduce surface roughness [53, 39]. Less aggressive solvents should be used if possible to keep the material from getting damaged. This enables solvent to be used more liberally or avoid toxicity for biological assays [54, 55]. Most materials do not need to be broken down chemically to generate a permanent solvent bond. To ensure the best bond

strength UV curing and UV-ozone treatments can be used [56, 49].

The major tradeoffs are toxicity, flammability of the solvent, and the potential for channel deformation if too much solvent is used. The solvent may also generate bubbles in the device after bonding. An example of cyclohexane bubble formation in a COC device is provided in **Figure 1-4**.

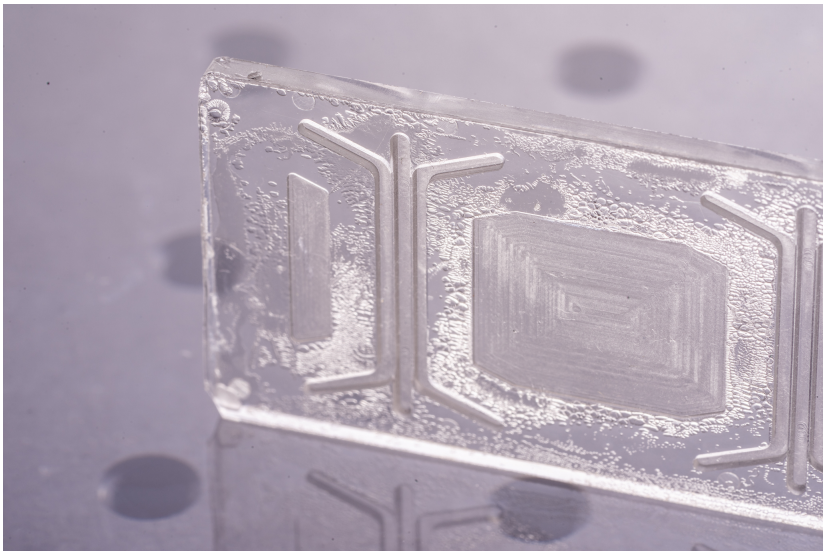

Figure 1-4: Cyclohexane solvent coming out of solution in a bonded COC device.

Adhesives can also be used to join the layers microfluidic devices. A variety of adhesive techniques can be used, but the most common technique is to laser cut thin film adhesives and align them to the layers of a device [47]. Many companies (Takasago Fluidics, Aline Inc., etc.) specialize in this method to produce off-the-shelf and custom microfluidic chips. The benefit to this method is that the adhesives only contact the edges of microfluidic channels, but aligning the layers can be difficult and not all geometries are possible. Further, most thin film adhesives are not solvent resistant and their chemical interactions for biological assays are not well understood. Thin film adhesives are not the only option, for example, a new UV curable adhesive for bonding of optically clear and low toxicity PMMA microfluidic chips has been developed [57]. For prototype purposes, Scotch tape and PCR sealing tape can provide a simple and effective option for sealing microfluidic devices [58].

Thermal bonding is the most common method for joining thermoplastics, and

for good reason. A well-defined thermal process can generate a thermal bond that approaches the strength of the bulk materials and without the need for an additional treatment, solvent, or material interface. COC devices, for example, can be thermally welded for applications that involve biological and/or chemical sensitivities [40, 59]. The factors that contribute to a strong thermal bond in COC devices include time, temperature, and pressure or the thermal process, as well as the glass transition temperature and molecular properties of a specific grade. It is worth noting that the use of two different grades can be beneficial so that channel deformation is limited to one material; typically this implies using a higher temperature grade for the bulk material and a lower temperature grade for the laminate [60].

Thermal bonding can be accomplished in a variety of different ways; the process just needs to involve compatible materials as well as the right time, temperature, and pressure parameters. Devices might be sealed using a roll laminator, a thermal press, or even submerged in boiling water [61]. Ultrasonic welding, friction welding, infrared bonding, heat stacking, are all examples of thermal bonding techniques that might be used depending on the given application. Thermal bonds may also be used to join rigid substrates to elastomer films for applications requiring a flexible biocompatible membrane [62, 38].

1.5 Physiological Fluidic Conditions

An effective microphysiological system must be able to mimic the fluidic conditions found *in vitro*. Cells and organs are sensitive to the flowrates and pressures of of media circulating through the device. The device must also meet specific geometric criteria to allow for the convective and diffusive transport of nutrients and growth factors found in the culture media. For example, the system must be able to supply an appropriate oxygen tension, glucose concentration, and levels of growth factors and hormones. From a mechanical design perspective, these criteria can be accomplished by controlling system pressures and flowrates to match those found *in vitro*. Some previously explored methods for controlling these fluidic properties are discussed be-

low.

1.5.1 Pneumatic Micropumps and Membrane Valves

A significant contribution of the Griffith lab at MIT has been the design and mechanical modelling of a pneumatic micropump that can be used to recirculate culture media between wells of a microphysiological system [63]. The pumps have been employed on a number of platforms and used to study processes such as the gut microbiome, and is the inspiration for the pump designed in this thesis [64]. The pump design is also central to the functionality of the LiverChip and PhysioMimix platforms (CN Bio Innovations, Welwyn Garden City, UK). This is not the only kind of micropump technology that could be employed for MPS systems, so it is worth comparing the different types of pump designs for a given application [65, 66].

Pneumatic micropumps have been widely studied and many different designs exist. These types of pumps have been used in a wide variety of BioMEMS devices and biomedical applications as well [67, 68]. The functionality of these pumps generally relies on a circular diaphragm and pump chamber sandwiched between two valves. The pump chamber is designed to displace a fixed volume for a given stroke of the membrane. The membrane is usually a flat elastomer film displaced by an applied pressure, but this design could be modified. For example, a rolling diaphragm or a dielectric elastomer diaphragm could be used [69, 70]. The membrane material is also a key consideration, as the membrane stiffness, barrier properties, and creep characteristics play a role in performance and reliability [71, 72].

The design of the pump chamber is usually more straightforward than valve design as it is deterministically defined by stroke volume. Valve design presents two additional challenges: the valve must generate a strong seal against head pressure and must be low-volume so that it does not displace additional volume. A valve design made of PDMS may be as simple as a doormat valve [73]. Doormat valves are the simplest valve design, but they do not have well-defined sealing characteristics and can be difficult to produce using thermal or plasma assisted bonds (the membrane bonds to the valve seat because it is contact with the flat surface during the

bonding procedure) [39]. Thermoplastic elastomer valves are possible in a variety of configurations if the correct design and approach are used [74]. Valve designs may be optimized using core mechanical design principles and the fluid structure interactions can be modeled using advanced FEA simulations [75, 76]. An optimized valve design should feature a geometry that concentrates the applied force onto a defined sealing surface [77].

1.5.2 On-Chip Pressure Control

Control of microfluidic channel pressures has traditionally been performed using gravitational head or with external pressure sources and has not been widely studied or explored in different ways. Closed-loop feedback of reservoir height has been used for controlling gravitational head pressure and flowrates, and a wide variety of on-chip pressure sensors have been developed for biological studies [78, 79, 80]. A pressure regulating mechanism has been designed to improve loading of cell-laden hydrogels, but oddly no on-chip pressure regulators seem to exist [81]. Electromagnetic microvalves have been used to control fluid flow properties, and many different valve designs do exist for different applications [82, 74]. External pressure supplies can be used as a pressure pump, and pressure controls for microfluidic chips are getting more refined [83]. Ideally, a flow determined pump could be used and connected to resistive and capacitive elements to determine the channel pressure. Unfortunately these systems are still in their infancy [84, 85]. It is possible that a jet-type regulator or gas-pressure regulator might be considered for microfluidic applications [86, 87]

1.5.3 Control of Flow Stability

Limited work has been done to improve the stability of pneumatic micropumps. Previous work from our lab has used fluidic capacitors for damping fluid pulsations and providing near continuous flow profiles [63]. A similar technique was used by collaborators in conjunction with an electronically controlled pressure regulator for smooth pump chamber actuation [88]. Other researchers have used these techniques, and

validate that compliant membranes can help to damp fluid flow [89]. Other forms of fluid capacitors could be used to help to smooth out fluid flow, but require further exploration [90]. Systems should also be evaluated in the presence of bubbles, elastomers, soft tubing, and other types of compliance [91].

Chapter 2

Platform Design

2.1 4-Chip Manifold

In this Chapter, extensive detail will be provided about the platform that was previously introduced in **Figure 1-1**. This section will describe the design process and key features of the system including the manifold design, base plate geometry, and standardized chip format. Another view of the platform with a different chip design is shown in **Figure 2-1**.

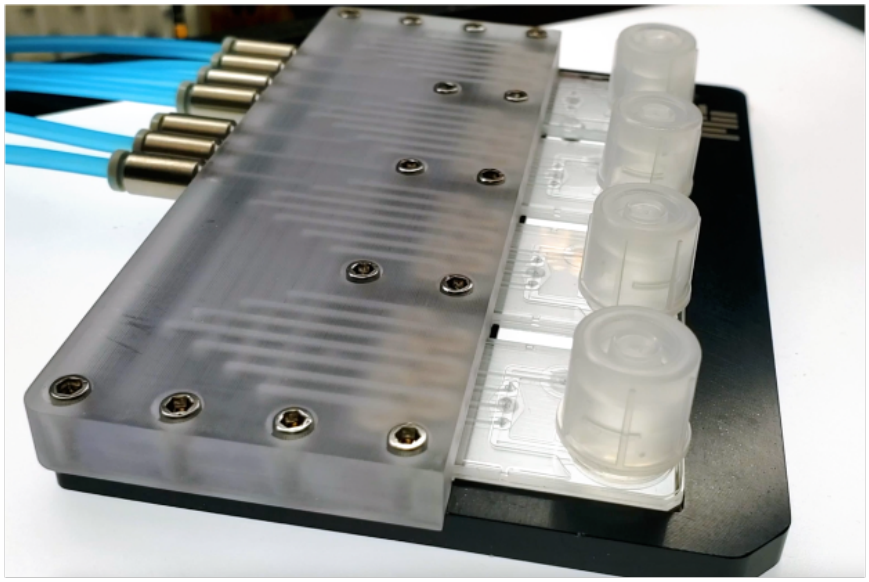

Figure 2-1: A 4-chip platform featuring a low-cost manifold, an aluminum base plate, and 5-layer chips with integrated elastomer membranes.

2.1.1 Standardized Chip Format

To facilitate chip integration and accommodate future chip designs a standardized 5-layer chip format was developed. The chip format includes a fluidic layer and a pneumatic layer separated by a bonded thermoplastic elastomer membrane. The top and bottom of the chip are laminated with a co-extruded film that ensures reliable bonding. Each layer is a well-defined thickness so that the final assembly is controlled to a height of 2.50-2.55 mm. The chips also have a standardized pneumatic interconnect that allows 7 pneumatic signals to be passed into the chip; the interconnect is 7 hexagons that serve to support the compression force of the O-rings and to concentrate pressure for reliable bonding. The bonded areas of the chip are raised surfaces in the fluidic and pneumatic layers that serve to concentrate the pressure for bonding and help to reduce bending loads between the bonded regions. These surfaces are raised 200 μm above open cavities which allow for gases to escape through a series of vents in the sides of the chip. Gasses must be allowed to escape during the bonding procedure and when the platform moves between environments of different temperatures. An exploded view of this chip format is provided in **Figure 2-2**.

The bonded regions vary in size and shape, but are generally 0.8-1 mm in width. The fluidic and pneumatic channels are typically 0.4 mm in width and depth. The chips are 25 mm wide and 40 mm long; future designs will allow for larger chips but the small size and golden aspect ratio make it easier to design chips that are easy to fabricate and assemble. The small size is less sensitive to runout; features are more tightly packed so there is reduced concern with machining tolerances and variations in the stock thickness. The format also reduces the chance of the chip breaking due to bending loads during manipulation of the chips when assembled into a manifold. The chips are not very thick so they can flex quite easily. The aspect ratio is beneficial because it makes it easy to align the layers of the chip by hand and provides a compact form factor for connecting fluidic and pneumatic channels. Larger chips with and high aspect ratios are harder to align and sometimes break or delaminate due to bending.

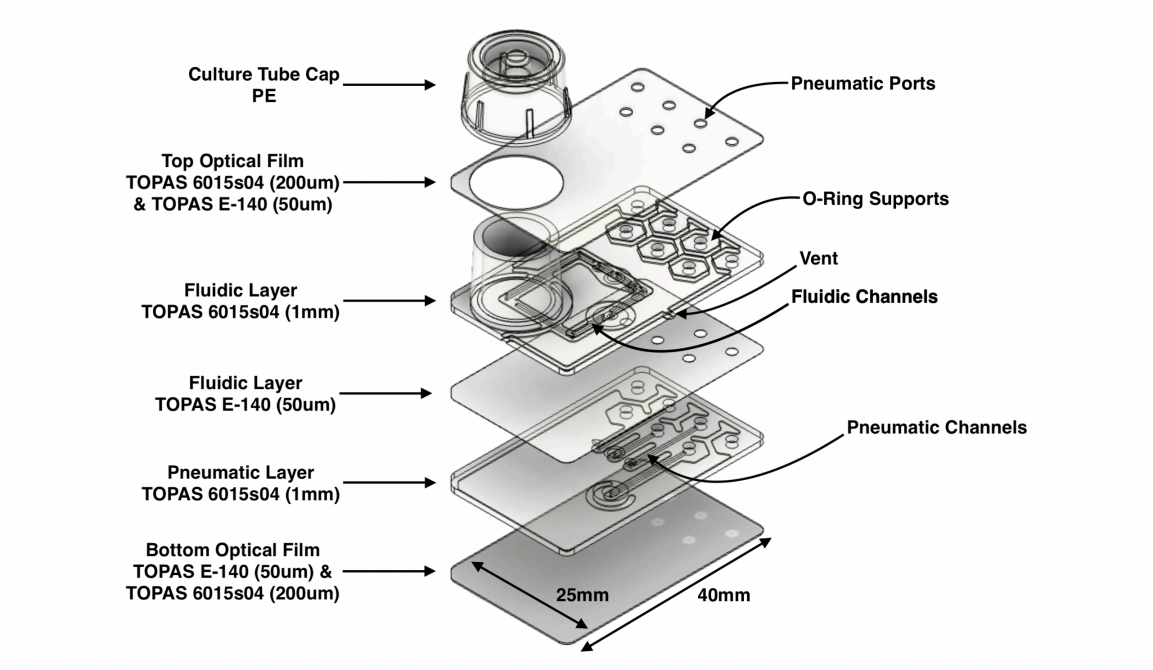

Figure 2-2: Exploded view of the standardized 5-layer chip format with a fluidic layer and 7 pneumatic ports defined by a hexagon pattern at one end of the chip. The culture tube cap allows pipette access to the reservoir. Vents allow for gas to escape the chip during bonding. The material grades of the chip layers are provided but may be changed in future chip designs.

2.1.2 A Low-Cost and Serviceable Pneumatic Manifold

The chips are connected to a pneumatic manifold with integrated O-rings. Typically, pneumatic manifolds are diffusion bonded components and are made of acrylic, polycarbonate, or polyetherimide (PEI, Ultem) for medical and life science applications. Bonded manifolds are used to connect gas and fluid lines to other components and can provide a strategy for eliminating fittings, reducing assembly time, and improving a system's performance [92]. Prototype manifolds can be expensive and hard to produce due the time intensive process and need for layers that are flat and smooth. The manifold designed for this platform is low profile with tightly packed channels so that future iterations could be assembled quickly using a thermal press and a bondable lamination material or by using an adhesive backed film. The manifolds are 9 mm thick and prototypes can can be produced using 3D printing; SLA 3D printing is a preferred method because a variety of medical grade and autoclavable resins exist.

The underside of the manifold is shown in **Figure 2-3**. The bottom of the manifold features a pocket for reduced material use, a hole and slot for alignment to the base plate using dowel pins, and a 0.5 mm skirt that protects contaminates and liquids from getting under the manifold. 14 #4-40 machine screws with low profile washers are used to bolt the manifold to the base plate.

Figure 2-3: A low-cost manifold was 3D printed using a Carbon 3D SLA printer and a proprietary medical grade resin.

2.1.3 O-Ring Gland

The bottom of the manifold includes 7 glands that are used to constrain 7 Viton O-rings into the manifold. The glad uses a 56 degree taper to hold a -004 size O-ring in place. The relevant dimensions of the O-ring gland and an image of their sealing characteristics once compressed are provided in **Figure 2-4**.

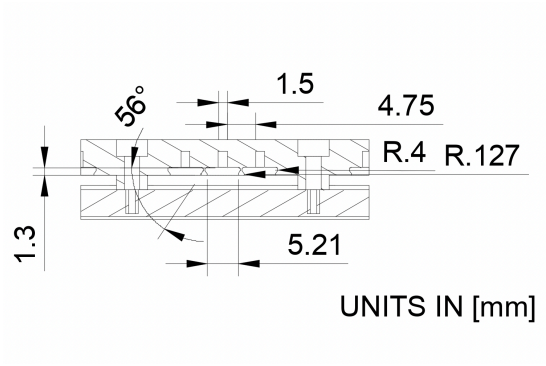

(a) O-ring gland dimensions

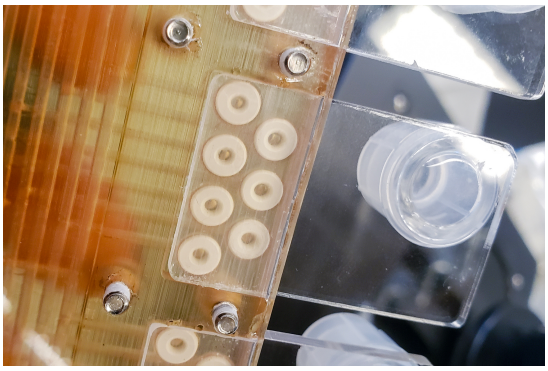

(b) Visible compression of O-rings

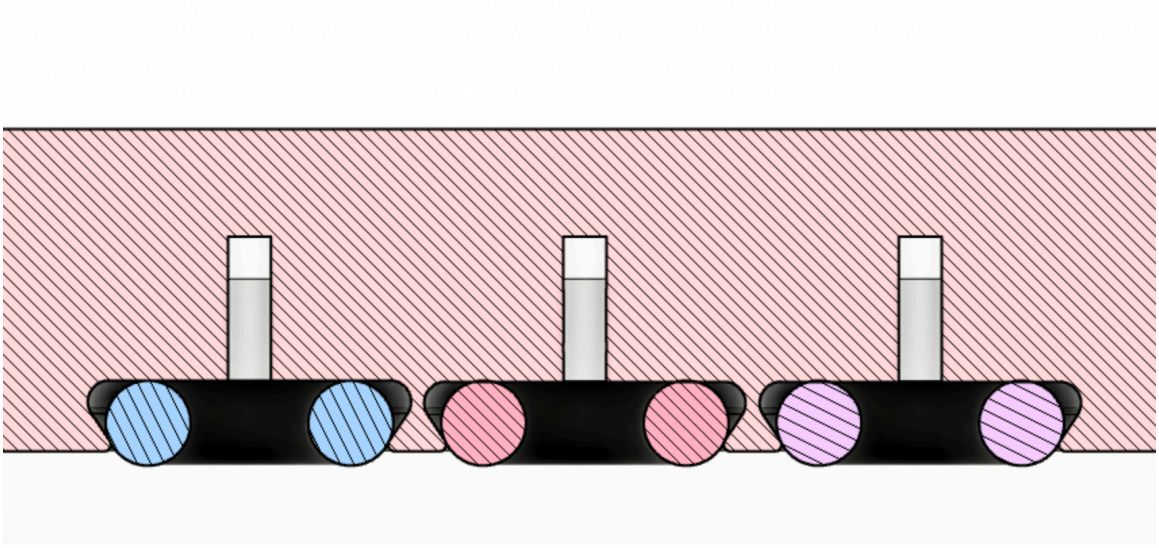

(c) Cross-section of 3 tightly packed O-rings.

Figure 2-4: Retaining and sealing of Viton O-rings is demonstrated with a 3D printed manifold. (a) O-ring gland in cross-section. (b) Sealing of a blank chip. (c) O-rings can be tightly packed using the gland geometry. The O-rings are visibly compressed, verifying their sealing characteristics.

2.1.4 Pneumatic Connections

The manifold is connected to a pneumatic control unit using 7 push-to-connect fittings and 1/16" OD tubing. The 7 tubes are connected to a 10-way valved connector made by Colder Products Company; the valved side of the connector is kept in the incubator so that gasses do not escape when the platform is disconnected. The connectors are shown in **Figure 2-5**. A long-term goal is to develop a manifold that has a quick-release clamp for connecting the chips to the manifold. Additionally, the push-to-

connect fittings will be replaced with a pneumatic coupling that does not require the use of tubes on the platform.

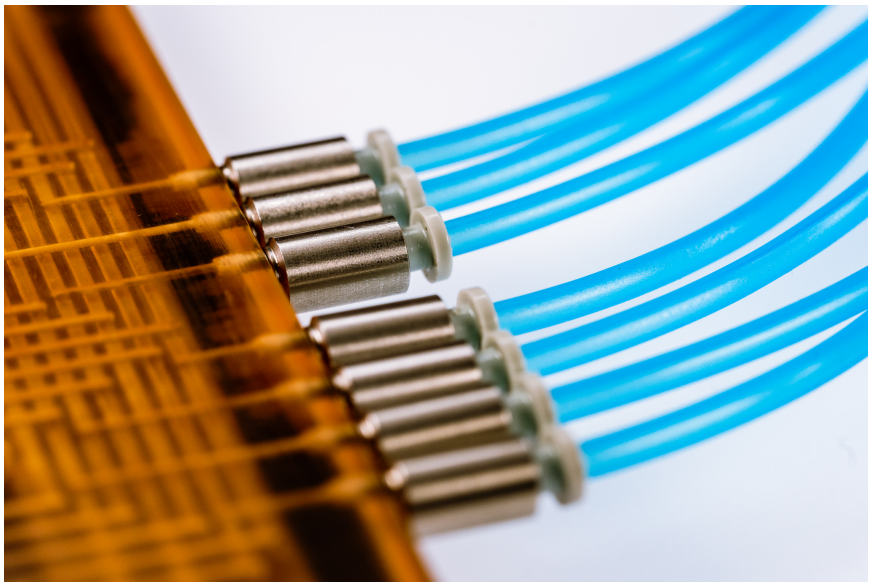

Figure 2-5: 7 pneumatic push-to-connect-fittings are screwed into the side of the manifold and connected to 1/16" OD tubing.

2.1.5 Microscope-Friendly Base Plate

The chips and manifold are connected to a machined aluminum base plate that is anodized black. The plate uses blind taps so that the screws are only visible from one side and so that the platform is easy to clean. The chips are suspended over a rectangular hole in the plate that serves as a viewport for imaging the chips. A taper was added to the underside of the plate to provide clearance for microscope objectives. The plate dimensions are the same as a 96-well plate so that the platform fits into a standard plate reader on most lab microscopes [93]. The platform is shown mounted to a Thermo Fisher EVOS M5000 in **Figure 2-6**.

2.1.6 Incubator Compatibility and Sterilization

The platform and chip materials are ethylene-oxide (EtO) compatible and may be routinely sprayed down with ethanol. The base plate can be wiped down and the

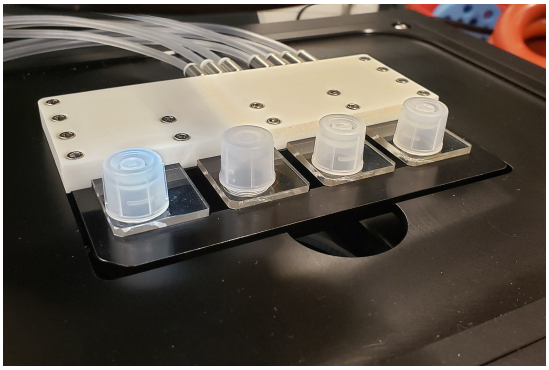

(a) 4-chip platform prototype mounted in a Thermo Fisher EVOS M5000 Imaging System.

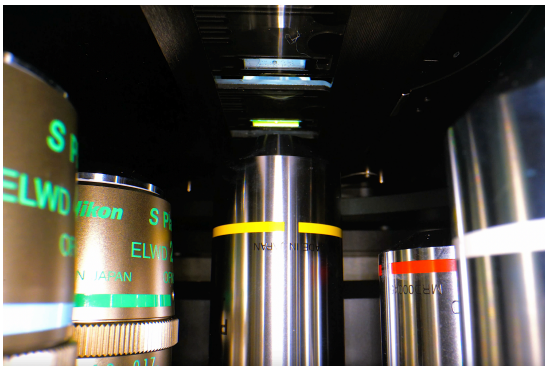

(b) The underside of the platform has a taper that provides clearance for microscope objectives.

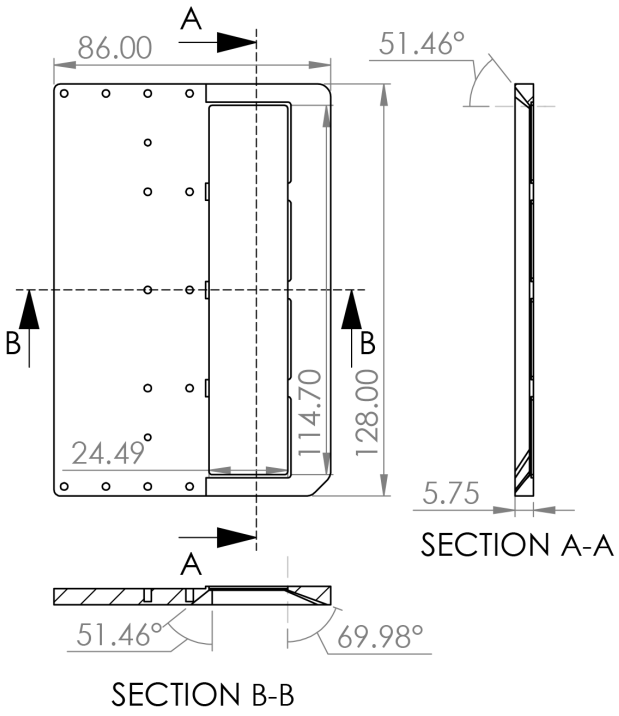

(c) Drawing of Base Plate. Units are in millimeters.

Figure 2-6: The platform fits a standard plate adapter and accommodates most lab microscopes. This format can also accommodate plate rockers, plate holders, autosamplers, and other standard lab equipment.

chips are easily cleaned using a microfiber cloth. The chips are isolated from the manifold, so sterility of the manifold is less important than sterility of the chips. The chips are sterilized separately and assembled into the manifold afterwards. All

materials are compatible with the incubator and feature low water absorption at the elevated temperatures and humidity levels used for cell culture; this is typically 37°C and 90-95% relative humidity for CO_2 tissue culture incubators. This temperature is the same as normal body temperature and the humidity helps to reduce evaporation of culture media.

2.1.7 Lids and Caps

The platform ports exposed at one end of the chip are only used for pneumatic controls so all fluid sampling is done using a pipette. The rationale for this choice is to use standard lab techniques for the chip user. The chips designed in this thesis include a 400 μL reservoir that accommodates a standard 2-position culture tube cap. 400 μL provides sufficient volume for most small-scale tissue samples, but other sizes of reservoirs could of course be used. These reservoirs will become an injection-molded feature in finalized chip designs, but are made of polystyrene and glued to the chip for prototyping purposes. Future reservoirs will have a taper at the bottom so that media will be directed to the inlet and sharp corners will be avoided so that fluid does not get trapped in the corners of the reservoir. The reservoir and its associated cap are shown in **Figure 2-7**.

2.2 Pneumatic Control Unit

Two pneumatic control units are used to drive the platforms in the incubator and at the microscope. These control units were developed in previous lab projects and were purchased from CNBio. The control units use an array of solenoid valves to switch between pressure and vacuum to drive the pneumatic micropumps on the platform [63]. The units connect to the platform via 1/16" OD tubing that is passed through a port in the incubator. The pumps can be driven from 0-3 μL/s and are regulated at $\pm$9 psi. Other pressure sources may be connected to the platform to accommodate different chip designs. A LabView interface is used to control the pumps from a dedicated laptop. A portable unit with an integrated pressure and vacuum source is

Figure 2-7: Injection-molded polystyrene reservoir that accommodates a two-position culture tube cap and can hold up to 400 μL of culture media. These reservoirs will eventually be a molded feature in future chip designs but are glued to the chips for prototyping purposes.

also used to control the platform at the microscope or in a tissue culture hood.

Chapter 3

Cyclic Olefin Copolymers

Cyclic Olefin Copolymers are a relatively new class of polymer with applications in, for example, the medical, pharmaceutical, packaging, and optical industries. COC polymers are high purity thermoplastics with optical properties similar to glass and mechanical properties that can be tuned for specific applications and manufacturing processes. Despite these traits COC polymers have been slow to gather widespread use. Many part manufacturers are still relatively unfamiliar with the material, and raw stock can be difficult to acquire. The first commercial COC resin grades debuted in the year 2000 and only a few other manufacturers have started to produce competitive products since. The lack of widespread adoption may be explained in part by the lack of raw material suppliers and due to the high cost of COC when compared to competitive polymers.

COC is a co-polymer chain produced from norbornene and ethylene in varying proportions. Grades with a higher proportion of norbornene tend to be mechanically stiff with higher glass transition temperatures. The polymers are typically amorphous and their melt-flow characteristics can be tailored via molecular weight. Most grades are good electrical insulators which can be metallized with no pre-treatment. COC tends to exhibit low water absorption and excellent barrier properties making it an ideal packaging material [94]. COC is resistant to most solvents and chemically inert relative to other polymers. The main exceptions are solubility in non-polar organic solvents (i.e. cyclohexane, toluene) and surface interaction with lipids and fats [95].

Adjusting the thermal properties and molecular weight enables many production capabilities as well. COC can be readily produced film extruded (including co-extrusions), injection molded, hot embossed, thermoformed, blow molded, and machined. Different grades from the same manufacturer can also be combined into custom blends for advanced applications. These properties make it a suitable and desirable alternative to competitive plastics such as poly-methyl-methacrylate (PMMA), polystyrene (PS), and polycarbonate (PC).

The COC resins in this thesis were produced by TOPAS Advanced Polymers GmbH. Any COC manufacturer could have been used, but many of the components designed in this thesis were produced with an elastomeric grade of COC (TOPAS E-140) that is only available from TOPAS. TOPAS polymers were used for the sake of consistency and under the assumption that better bonding characteristics and adhesion would be observed in devices made with grades from the same supplier. Specific grades will be addressed in detail below.

3.1 Material Properties and Resin Grades

When compared to PDMS and alternative thermoplastics for microfluidic applications COC offers a number of useful benefits. First, COC has similar optical properties to glass and PMMA; it is non-fluorescing, with optical clarity aross the UV to near-IR range. This property makes it suitable for advanced imaging techniques commonly used in the microfluidic field. All resin grades produced by TOPAS exhibit these properties with only a slight degree of variation, but some are better suited for medical and biological applications due to their purity and surface properties. Three resin grades are commonly found in the industry: TOPAS 5013f04, 6015s04, and 8007s04. TOPAS 5013 is commonly used in food and packaging applications and 8007s04 is often used for accurate feature reproduction and low temperature bonding applications. TOPAS 6015s04 was selected as the bulk material for this project due to previously studied optical properties as demonstrated in **Figure 3-1** [96].

TOPAS 6015s04 is a unique grade in that it can be produced by both film extrusion

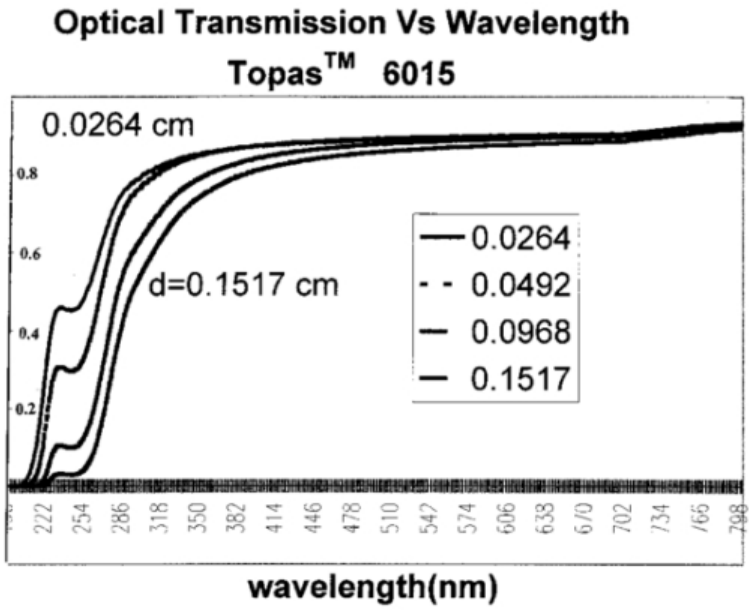

Figure 3-1: Optical Transmission of TOPAS 6015s04 grade COC with varying thickness, from [96].

and by injection molding. The material is also mechanically stiff as compared with other grades, so assembled chips are less likely to deflect under load and delaminate. The material is comparatively scratch resistant for its class, though this is not a major selling point for COC polymers [97].

TOPAS 8007s04 was also considered as an alternative material for the fluidic layers of the microfluidic devices but the low glass transition temperature and ductility caused significant challenges when machining prototypes, as well as issues with surface finish and thermal instability during bonding procedures. The split personality of different grades meant that the 8007s04 parts would deform during the bonding process and residual stresses would cause the parts to warp after cooling. This grade may be reconsidered for future projects where low-temperature bonding is required, or when nano-scale feature reproduction is required.

An elastomeric grade of COC can also be produced by creating a semi-crystalline structure in the polymer matrix, typically by increasing the fraction of ethylene and by reducing the molecular weight. TOPAS produces an elastomeric grade, TOPAS E-140, which can be produced using similar methods as the other grades. Further,

E-140 can be blended with 8007s04 due to closely matched thermal properties and used to modulate the stiffness of COC components. Most importantly, E-140 can be produced using a roll extrusion process. The grade has no direct competitors, though other materials, such as TPU and SEBS elastomers, could be used as alternatives. E-140 offers a unique advantage in that it has similar optical and barrier properties to rigid COC grades. The resin is non-fluorescing, but has some haze when produced in thicker layers. The grade has similar (often improved) solvent resistance to other grades and also exhibits low water absorption. Due to the elastomeric nature, the grade has increased free volume and higher gas permeability than rigid COC (similar to other low density olefins) [98]. The material has been used in limited industrial applications and is difficult to work with [49, 99]. It is notably sticky, quick to gather static charge, and very easy to melt. When properly processed, the material holds significant promise for the development of medical tubing, containers, and packaging materials [100]. These same properties make it an ideal candidate for fabricating advanced microfluidic devices.

3.2 Custom Thin Film Extrusions

A 2 mil (50 μm) thick film of E-140 was successfully extruded onto a controlled thickness 10 mil PET carrier film using an external supplier. The film was produced in an experimental facility, so it is worth noting that some impurities may be present in the material including trace amounts of other polymers, dissolved gasses, and small particles of dust and other contaminates. The produced film was cut into 2 rolls that were each 0.5 meters wide and 100 meters long. Over time at room temperature the rolls became self adherent; to avoid this, the rolls are cooled to 4°C to keep the low molecular weight species from interacting. This prototype roll was produced on a backing layer of standard PET material, but it would have been preferable to use a higher temperature grade of PET for reasons that will be explained later.

The thickness of the film was selected as a good balance between flexibility and toughness. A 1 mil thick film would be possible to produce, but more difficult to

work with. Making the film slightly thicker makes it mechanically robust and easier to handle. A thicker film would have reduced flexibility and membrane elements would be more difficult to design and produce.

The roll of TOPAS E-140 is used to make thin elastomer membranes that are optically transmissive in the UV to near IR spectrum with a small degree of haze [101]. The optical clarity of a 50 μm thick laser cut membrane is shown in **Figure 3-2**. For some applications these membranes can be directly mechanically clamped between 2 substrates, but a preferable method is to thermally weld the membrane between substrates. The membranes were initially validated by installing them into a previously developed pump that utilized a polyurethane membrane. The pump flowrates were measured in both forward and backward pumping directions. The pump flowrate was accurate and stable for several days showing that E-140 could be used to design membrane-based pumps. The flowrate data is provided in **Figure A-1**.

Figure 3-2: A laser cut elastomer membrane made with TOPAS E-140.

TOPAS E-140 has a melting point of 84°C and has very good adhesion to other grades of COC. E-140 can be bonded to other COC materials using a UV-ozone treatment or by thermally joining the material to other grades. For best results, a thermal process should ensure that the E-140 grade reaches or exceeds its melting

point. Bonding can occur in the glass transition region, but the bond is usually weak and reversible without prior surface treatment. By melting the E-140 a bond strength nearing the strength of E-140 can be achieved, creating a weld that can only be broken by destroying the E-140 component in the process. The bond strength can be further improved if the thermal process approaches the glass transition temperature of target substrate. For example, bonding TOPAS E-140 to TOPAS 6015s04 should be done above 84°C and below 158°C. This upper limit is just below the glass transition temperature of TOPAS 6015s04 (T_g=158°C) and the lower limit is beyond the melting point of E-140 (T_m=84°C).

One concern with this bonding approach is that the E-140 can easily deform in its melted state. The material is observed to be stable up to 94°C for extended periods of time, but begins to warp and deform at higher temperatures. If a disturbance force is applied to the material it will conform by means of plastic deformation. This disturbance could be a directly applied force, pressure from the expansion of a gas, or even the weight of the membrane material. For this reason the E-140 should be supported as much as possible during the bonding procedure and the bonding process should be fast. A faster process ensures that the material does not displace in the melted state; this helps to preserve channel and membrane integrity during the bonding process.

An early experiment was conducted to see if the E-140 film could be laminated onto a microfluidic chip to create a flat and unsupported surface. A set of 10 injection molded COC chips with 1 mm wide channels were bonded to a laser cut 25x75 mm sheet of the E-140 film using a thermal press. With a proper mechanical support, in this case provided by the 10 mil PET, the material could be successfully joined without warping into the COC chip. To further explore the thermal stability, a few of the chips were placed in an oven at 94°C for a day and it was found that the membranes could be preserved even at these high temperatures. A photograph of one of these laminated chips is provided in **Figure 3-3**.

The thermal bonding characteristics of E-140 are so promising that it became our main candidate for a novel and easy to bond optical film. An optical film comprising

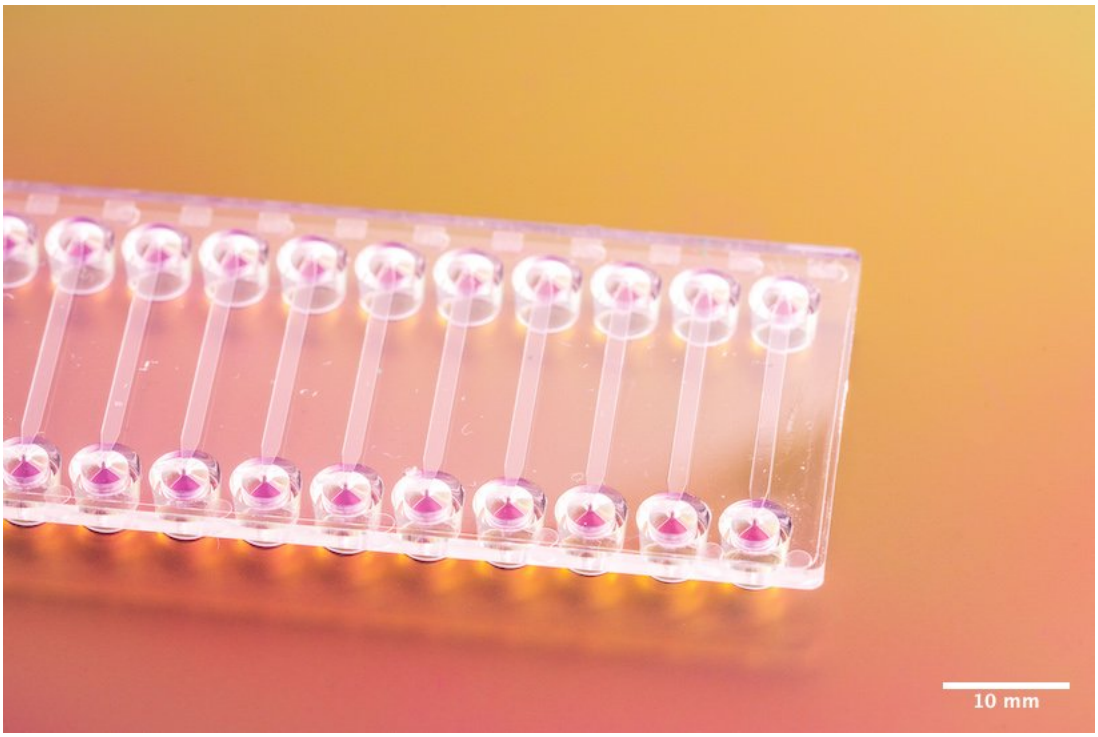

Figure 3-3: A COC chip laminated with a 50 μm thick film of TOPAS E-140 after being held at 94°C. Small dust particles can be seen trapped under the surface of the laminate, but no warping is observed in the E-140.

a clear and scratch resistant material on one side with a thin layer of E-140 on the other side is easy to selectively melt and seal onto another surface. This concept is similar to how a document laminator works; a higher temperature grade of PET is coated with EVA on one side to use as a hot-melt adhesive for joining the PET to a document. The EVA is very sticky and melts at a lower temperature than the PET. When passed though a laminator, the EVA rapidly melts and thereby creates a permanent bond between the PET and paper. A similar approach with COC materials was performed by spin coating a lower temperature grade of TOPAS polymer onto a higher temperature grade [102].

Based on this concept, a small section of a 240 μm thick TOPAS 6015s04 film was aligned to the E-140 film by hand. The E-140 creates a tacky union with the TOPAS 6015s04, so many bubbles were created between the two films. The PET carrier was then removed from the E-140 film and replaced with a red laminator sheet for temperature resistance. The 3 layer assembly was then passed through a Scotch brand

document laminator as shown in **Figure 3-4a**. The laminator generates enough heat to melt the E-140 and permanently bond it to the 6015s04. Due to trapped bubbles initially under the surface, the first laminate was hazy and full of bubbles (**Figure 3-4a**). By using a metal rod to roll one film onto another the films could be aligned without any trapped bubbles; this method has proven to be repeatedly useful for aligning one thin film to another. With this approach, and by varying the speed of the laminator, a significant improvement to the film quality can be achieved. The final film sample can be seen in **Figure 3-4c**

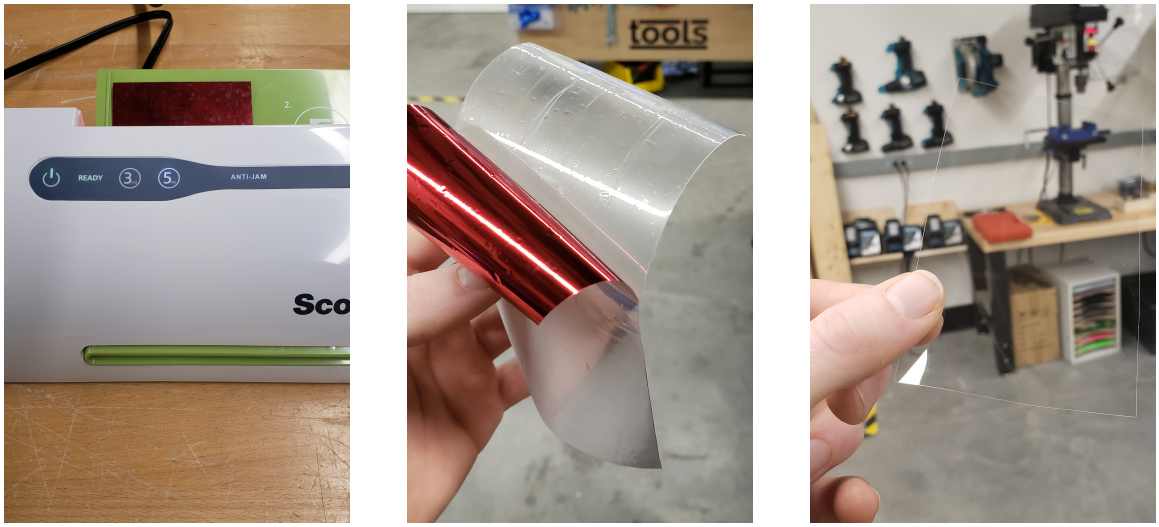

(a) Scotch Laminator (b) Original Laminate (c) Improved Laminate

Figure 3-4: A Scotch brand document laminator was used to create an optically clear and easy to bond film by combining a 240 μm thick TOPAS 6015s04 film and a 50 μm thick TOPAS E-140 elastomer film. (a) A desktop document laminator is used to melt layers of TOPAS 6015s04 and E-140 together. (b) The original laminate was hazy due to trapped bubbles and too much applied heat. (c) The laminate is improved by removing the bubbles prior to lamination using a roller.

This optical film design was then used to laminate many of the prototype chips in this thesis. The film can be cut to size using a laser, CNC milling machine, or vinyl cutter, and bonded using a variety of thermal processes. Although these handmade films are good enough for prototyping purposes, they are time consuming to make and the process has low yield. For this reason a co-extruded film of TOPAS 6015s04 and E-140 was produced by an external vendor. The material was specified to have an 8 mil (200 μm) thickness layer of TOPAS 6015s04 and a 2 mil (50 μm) thickness

layer of E-140. To protect the E-140 surface, a high temperature PET carrier film was added to the extrusion. The same PET carrier film was wound on the 6015s04 side as well, but this was unsuccessful, as the PET film showed little adhesion to the rigid 6015s04 COC substrate. A 100 meter long and 0.5 meter wide roll of the co-extruded optical film was produced and split into 3 rolls for easy storage.

The mass-produced film is of high quality and contamination free. The carrier film separates from the E-140 without much force, but stays on well enough to not delaminate by accident. Some initial bonding trials were performed by laminating the film onto a COC microscope slide using a thermal press for 120 seconds at 94°C. In this process bubbles were produced under the surface of the bond as shown in **Figure 3-5a** on a microscope slide and on a prototype microfluidic chip in **Figure 3-5b**. These bubbles form at the interface of the COC slide and the E-140 layer of the optical laminate.

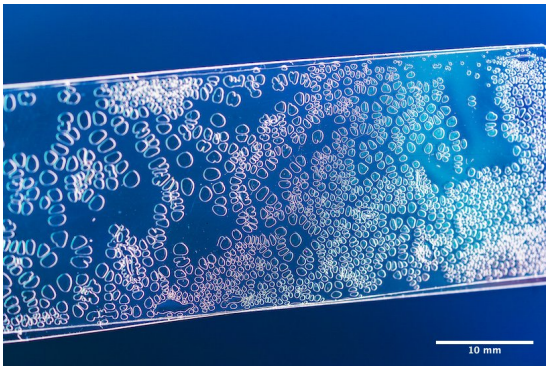

(a) Laminate on a COC microscope slide

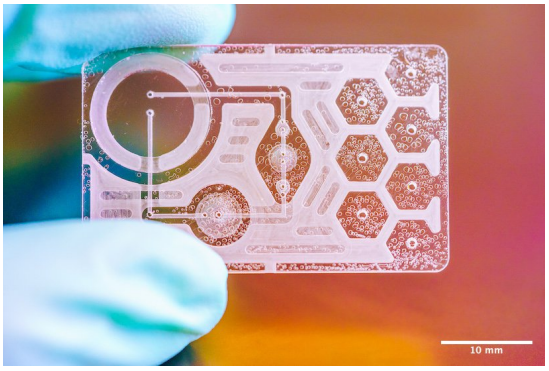

(b) Laminate on a COC chip

Figure 3-5: Bubbles form under the optical film after bonding at 94°C for 120 seconds. (a) Dissolved gasses escape from the optical film during the thermal bonding procedure and get trapped between the film and the bonded substrate. This is demonstrated by bonding the film to a COC microscope slide for 120 seconds at 94°C. (b) Bubbles also form when the optical film is laminated onto a microfluidic chip.

It was hypothesized that these bubbles were a byproduct of the manufacturing process used to produce the film. No vacuum degassing step was performed at the point of extrusion, so an experiment was performed to compare the degassing potential of the films in a vacuum oven. 25x50mm samples of the film were cut with scissors and placed in a vacuum oven at 65°C for 24 hours. A sample of the original optical

film made at MIT was also included in the study. The PET carrier was removed on one sample to see if the carrier film impedes gas from escaping. After degassing in the vacuum oven, the samples were removed and bonded to a COC microscope slide using a thermal press at 94°C for 120 seconds.

The bonded film samples are shown in **Figure 3-6**. The original optical film and mass produced films show a similar degree of bubble formation. These samples are essentially unusable. The degassed sample with a PET carrier film shows significant improvement, and in most bonding procedures these bubble would not appear at all; most bonding procedures will be shorter and the small landings on the chip help to evacuate the gasses that form during the bonding process. The sample without a carrier film performed even better, but it is likely better to leave the carrier on for sterility and contamination purposes. A longer degassing procedure of 72 hours (minimum) at 65°C with the PET carrier film combined with a less aggressive bonding procedure of 94°C for 20 seconds yields excellent results as described later in the thesis.

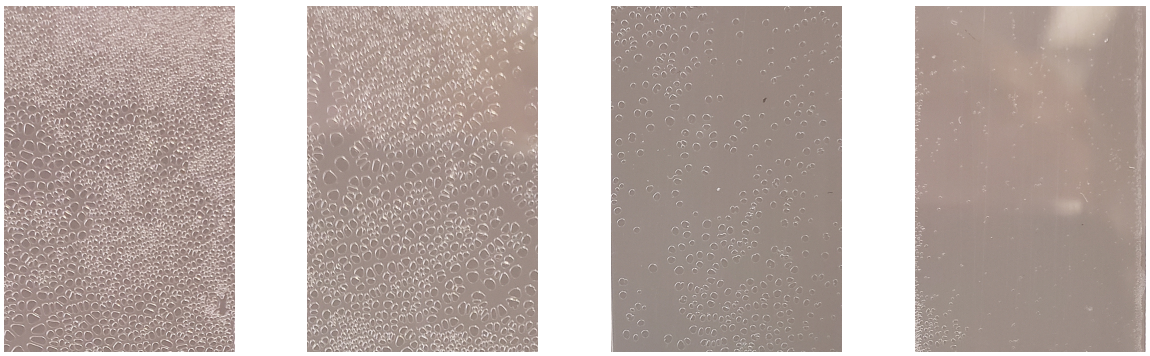

(a) Original optical film with no degassing step.

(b) Mass produced film with no degassing step.

(c) Sample with PET carrier and a degassing step.

(d) Sample no PET carrier and a degassing step.

Figure 3-6: Degassing the optical film for 24 hours in a vacuum oven at 65°C in vacuum oven shows promise for degassing the films and reducing bubble formation during lamination. Images shown are cropped to 20x30mm. The PET carrier film does inhibit gas from escaping, but longer periods (72 hours or more) of degassing can compensate for this tradeoff.

The degassing procedure also helps to smooth out the E-140 surface of the optical laminate. The original roll of material was slightly warped from the manufacturing process and small ripples can be observed on the material surface. By annealing the

material at 65°C the E-140 gradually levels out and creates a flat plane to match the reference surface of the PET carrier film. This effect can be qualitatively observed in **Figure 3-7**. The ripples in the surface go away and produce a surface that is clear and smooth.

(a) Before Annealing (b) After Annealing

Figure 3-7: Annealing the optical film under vacuum at 65°C with a PET carrier film provides a reference surface that smooths out the E-140 surface of optical film. Samples are shown with the carrier film removed after the vacuum degassing procedure.

The result of these procedures is an optical film that can readily melt to a COC substrate and create an optical window for a microfluidic chip. It is worth noting that these materials can also bond to PMMA, glass, and most olefinic polymers. For example, a prototype PMMA chip bonded with the COC optical film can be seen in **Figure 3-8**. The best bond strength is achieved by bonding to COC. With the right thermal process, discussed in Chapter 4, the material can be used to bond features of a variety of sizes and shapes. A laminated sample with excellent optical clarity and no bubble formation is shown in **3-9**.

Figure 3-8: A PMMA chip laminated using the COC optical film bonded at 105°C.

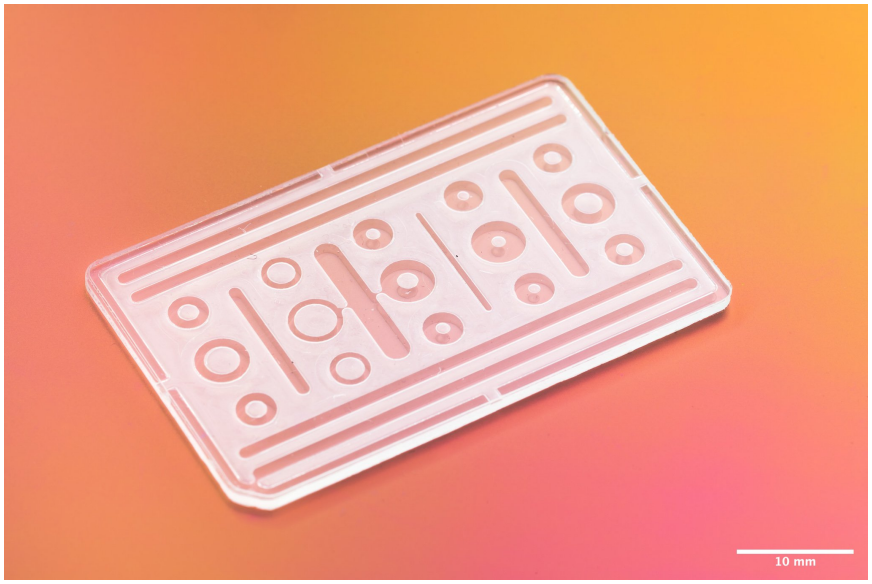

Figure 3-9: The film can be used to laminate a wide variety of shapes and sizes while preserving channel dimensions and optical clarity, as shown in this chip.

Chapter 4

Manufacturing Methods

A wide variety of manufacturing processes and techniques have been employed to develop the platform presented in this thesis. These fabrication methods are critical for producing a functional multi-layer microfluidic device and the key aspects of each process are described in detail in this chapter. This chapter also discusses the factors for reliably bonding multi-layer COC chips and highlights the future steps required to enable production at scale.

4.1 Micromachining

Moving away from PDMS presents a clear need for low cost prototyping of microfluidic chips [103]. Without the ability to easily mold and bond devices, other methods of fabrication must be employed. In most cases, CNC machining presents a low cost method for making plastic chips of a variety of materials with good surface finishes [104]. Desktop milling machines are even suitable for prototyping of small plastic devices [105]. Even with a low quality CNC machine, proper setup and tool paths can make for quick and accurate prototypes [106].

The majority of microfluidic chip prototypes developed in this thesis were first produced by machining on a Bantam Tools Othermill V2, a 3-axis PCB milling machine. The machine has a small work volume of about 5x4x3 inches with a maximum spindle speed of 26,000 rpm. The maximum resolution of the machine is 10um in all

dimensions due to the stepper motor drives, and the smallest recommended channel width is 300 μm based on the smallest tool diameter of 1/100". Channel depths as small as 50 μm have been produced, but smaller channels may be possible. There is no means to tram the head or spindle of the machine, so instead the machine's spoilboard was machined flat using a 1/32" flat endmill and a small stepover of 0.1 mm. This process takes several hours, but results in a surface that conforms to the machine x-y axis, and is polished flat.

Individual chip layers were machined by mounting a 25.5x75.5 mm COC microscope slide onto the machine using Nitto P-02 tape [107], a paper backed tape with good lateral stiffness, reliable thickness, and strong yet reversible adhesion to COC. For chips that need to be machined on both sides the chip perimeter is machined out of the microscope slide in the first operation. This ensures that all machined features are properly located with respect to the edges of the chip rather than a feature on the machine or microscope slide.

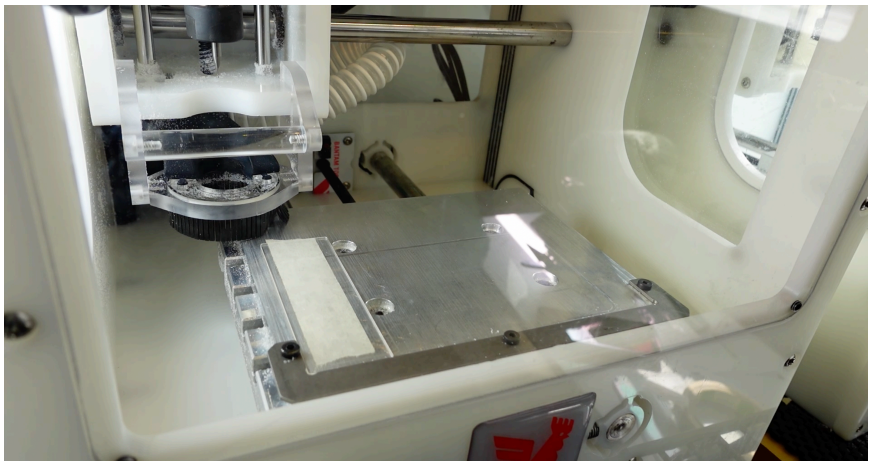

Figure 4-1: A microscope slide fixtured to the Othermill V2 PCB milling machine using Nitto tape.

There is some variation in the Nitto tape thickness, so as an alternative approach, a vacuum chuck was developed to hold 4 microscope slides directly to the bed of the machine. The vacuum chuck has precisely located pins for aligning the microscope slides and 4 valves for choosing which chip holders are active. This prevents vacuum leaks from the fixtures that are not in use.

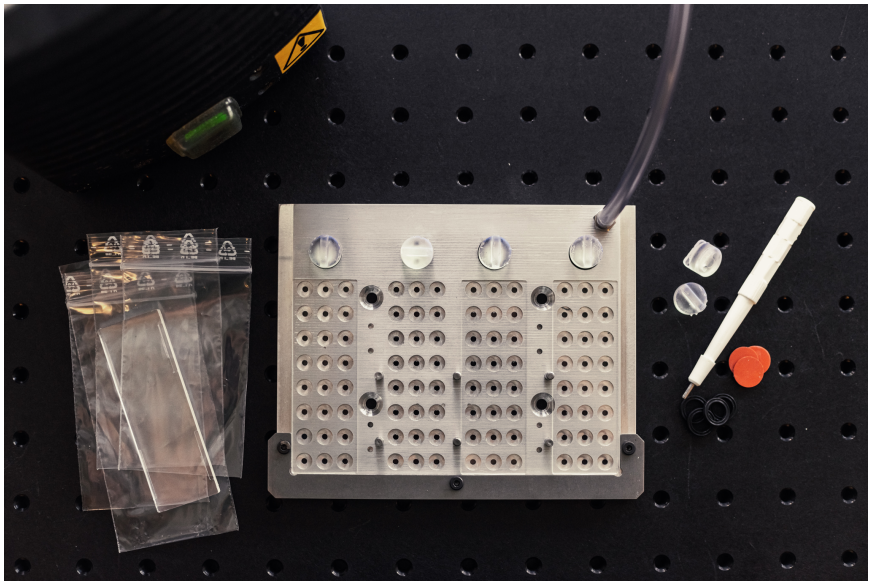

Figure 4-2: A custom vacuum chuck for machining multiple chips.

COC is notoriously difficult to machine. The material is has a tendency to rub against the tool and generate heat. Some grades, TOPAS 8007s04 in particular, have low glass transition temperatures and melt almost immediately in the machining process. This results in broken tools and damaged parts. Professional CNC machines can use machining coolants, but these must be carefully evaluated for use in biological applications. Using Dawn soap as a lubricant or using a vacuum port to draw air and remove chips of material can help to reduce the heat load.

A set of general-use machining parameters are provided in **Table 4.1** below. These parameters generally provide good results, but may need to be adjusted depending on part geometry and material grade. These feeds and speeds, as well as validated toolpaths, have been embedded into the CAD files for the standardized chip templates so that toolpaths can be generated quickly and with confidence that the materials will not melt. Steep and shallow passes are recommended for best surface finishes and dimensional accuracy. Drilling operations should done with small pecking depths and at significantly lower spindle speeds.

The quality of machined parts using these strategies is consistent and it is possible to produce duplicate parts. A picture of some identical machined chips is provided in **Figure 4-3**.

Tool Diameter	Spindle Speed (RPM)	Feedrate (in/min)	Stepdown (in)	Stepover (in)
1/100"	26,000	21	0.001	0.001
1/64"	26,000	31	0.003	0.003
1/32"	26,000	57	0.009	0.009
1/16"	26,000	100	0.021	0.021
1/8"	16,500	100	0.021	0.021

Table 4.1: General feeds and speeds for machining microfluidic devices made of PMMA or COC on a desktop CNC machine. More aggressive feeds and speeds may be used on professional machines with polished tools and coolants.

Figure 4-3: Duplicates of a prototype chip produced on the Othermill V2.

The CNC process was also employed to produce precise geometries for the optical laminates. To produce these parts, the optical film was cut into 2"x2" squares using a handheld passport photo punch and mounted onto a 3/16" thick acrylic spoilboard using 3M 8211, a double backed 25 μm thick roll of acrylic based optical adhesive. The parts are placed onto the adhesive with the TOPAS 6015s04 side down; this makes

sure that the PET and E-140 layers are cut first. This adhesive bonds permanently to the acrylic sheet but the COC parts can be easily removed without residue. A 1/64" flat endmill was used to cut a the part using a 1 degree ramp angle and the feeds and speeds provided in 4.1. A conventional cutting toolpath is used so that the PET film does not delaminate; climb cutting produces cutting loads that push against the part and lift it from the fixture. The contour toolpath is set to a cutting depth that exceeds the part thickness and cuts into the acrylic fixture. Parts are lifted from the acrylic adhesive using a razor. Any burrs remaining on the part can be removed using a scalpel or razor. The acrylic spoilboard is single-use and thrown away after machining. 4 parts were machined at once using this method. An example of one of these films with the PET carrier film preserved can be seen in **Figure 4-4**. The parts are washed with DI water after machining and degassed with the carrier film in a vacuum oven.

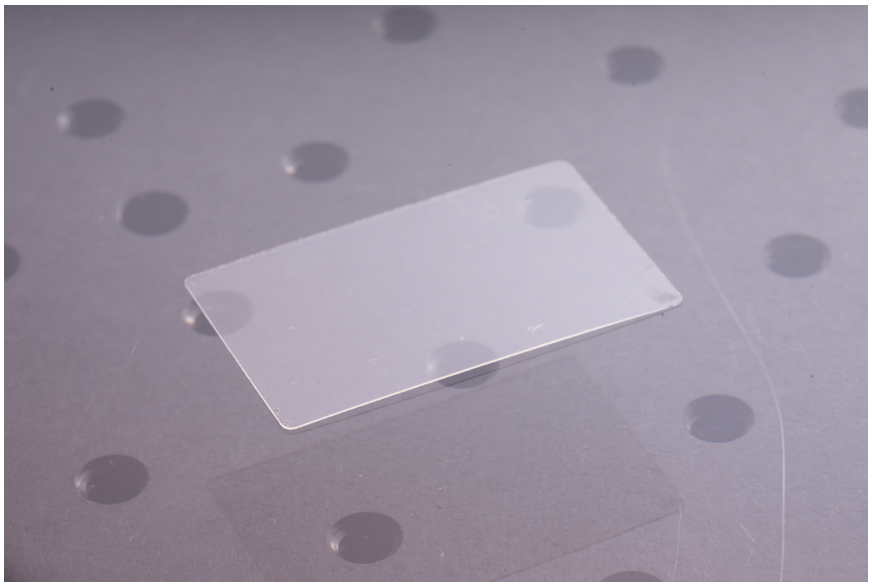

Figure 4-4: A machined optical film.

The CNC process is adequate for making prototypes but not recommended for production parts. A better production strategy would be die cutting or vinyl cutting process. These processes avoid the use of adhesives and additional fixtures. They are also better candidates for producing parts directly from the roll of material.

4.2 Laser Cutting

Many of the chip designs in this thesis require the use of a flexible membrane layer. Some microfluidic chip designs may require fluid to pass through a hole in the flexible membrane layer, and future designs may even incorporate channels that are etched or embossed into the membrane layer. To accomplish these designs, there needs to be a method for cutting the elastomer film into precise geometries. Such geometries may require sharp corners, small holes, as well as large aspect ratio slots. There are a variety of ways that this can be accomplished, including die cutting, vinyl cutting, or even micro-waterjet. Even the use of desktop tools, such as a digital craft cutter, can be sufficiently accurate for chip prototypes [108]. For this project, a CO_2 laser cutter was employed as the primary method for making these parts. CO_2 lasers do not produce the ideal wavelength for thin elastomer materials as the materials do not absorb sufficiently at this wavelength, but can still produce good results for making micropump membranes when configured properly [109].

A Glowforge Pro laser cutter was selected as the main tool for cutting the elastomer film. This machine is ideal because the tool has an office-friendly ventilation system, easy to use software, and a relatively low power laser, making it more suitable for cutting thin polymer films. To cut elastomer films on a laser the films must first be secured into a stretch ring, a drum-like fixture that is used for holding flexible materials taut. This fixture is functionally similar to an embroidery ring.

In these initial experiments, thin layers of the elastomer film were observed to experience significant melting at the edges of the material. Further, the material would move during and fly away when the cutting operation was complete, due to air currents from the ventilation system. The material was next fixtured to a cookie sheet made of medical grade stainless steel with a thin layer of water using capillary action. This process is outlined in **Figure 4-5**. The layer of water acts as a heat sink and as a workholding element for the material. This is not an entirely new concept as some water-assisted laser cutting methods have been used before [110]. Although this method yields promising results, the material still melts slightly and becomes hazy

due to stray particle emission from the material during the laser machining process. Some other samples fixtured to a pane of glass instead of the cookie sheet were also evaluated and displayed in **Figure 4-6**. This method results in bubble formation from water vapor as well as the production of small glass crystals that get embedded into the edges of the film. It is suggested that medical grade stainless steel, which does not reflect the laser beam, or germanium, which transmits long IR wavelengths, should be used as a supporting material for this technique.

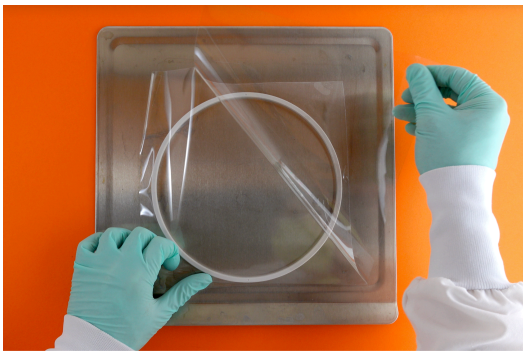

(a) Remove PET Carrier

(b) Press Retaining Ring

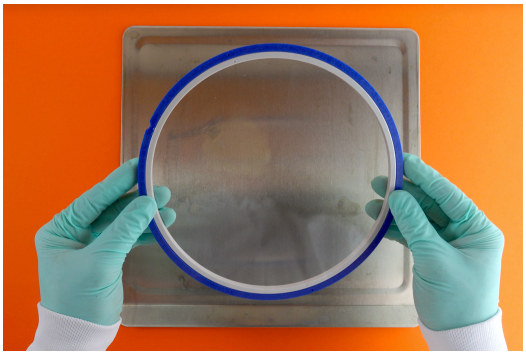

(c) Trim excess material from the edges of the stretch ring.

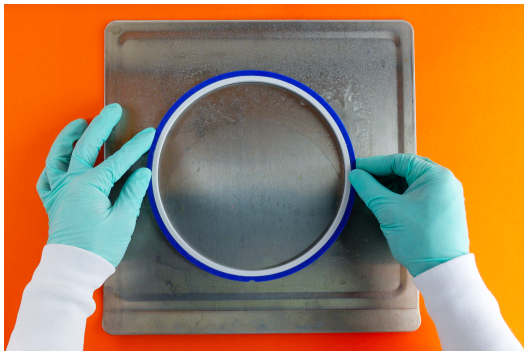

(d) Wick water under the film to hold it in place.

Figure 4-5: Preparing the E-140 Film for laser cutting. Some contrast was added to these images to better show the clear film and water.

To further improve the quality and accuracy of the laser cutting process the elastomer films are frozen to the cookie sheet at -84°C. Once frozen, the material is removed and a thin film of ice can be formed on the top of the elastomer by breathing slowly and letting the condensation freeze. This seals the elastomer into a protective sheet of ice that protects it from laser cutting byproducts. The ice also helps to keep the material fixed in one place so the parts are much more accurate than those

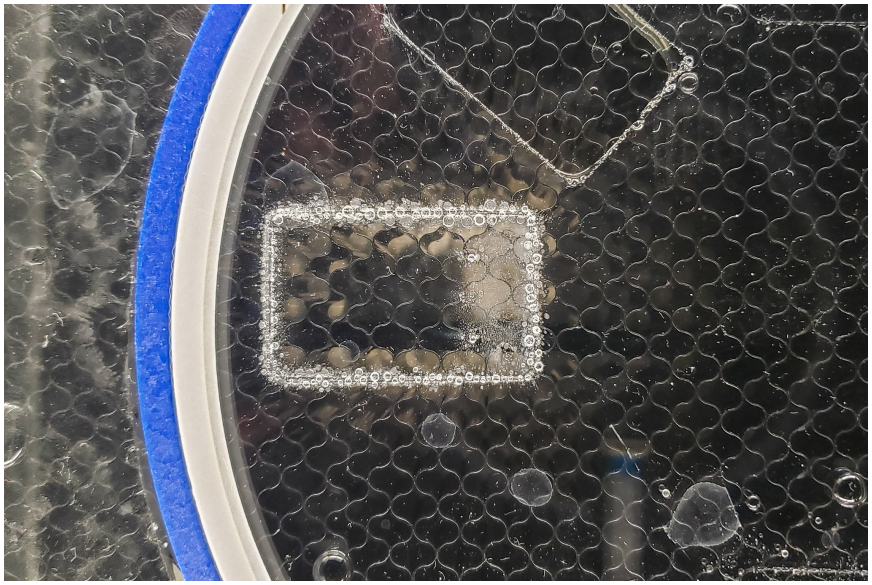

Figure 4-6: E-140 membrane suspended on a thin layer of water over a glass pane and laser cut. The laser machining process results in vapor bubble formation and the production of tiny glass shards.

suspended on water. A picture of the frozen sheet and a laser cut part using this method is provided in **Figure 4-7**. Holes as small as 0.4 mm have been produced, but the kerf of cut determined by the laser beam diameter must be considered for most accurate results. One limitation of this configuration is that the laser machining must happen quickly so that the material does not thaw. Since the laser adds heat to the system, only a few parts can be machined at one time. This process might be improved by using a thicker sheet of supporting material to add thermal mass, reducing the temperature of the machining environment, or by replacing the water with a phase change material so that the process is isothermal.

The frozen membrane method enables the fabrication of accurate prototypes in the lab, but may not be suitable for mass manufacturing. To explore the possibilities of laser manufacturing in a commercial facility, 3 stretch rings with the E-140 elastomer film were sent to a nearby laser manufacturing company to see whether the material could be cut using an ultrafast laser machine. An alternative method is to use a 193 nm wavelength laser on a quartz substrate. A femtosecond laser system (made by IPG Photonics) was used to cut a variety of slots and holes into the samples. The results were evaluated on a Thermo Fisher EVOS M5000 microscope and it was found

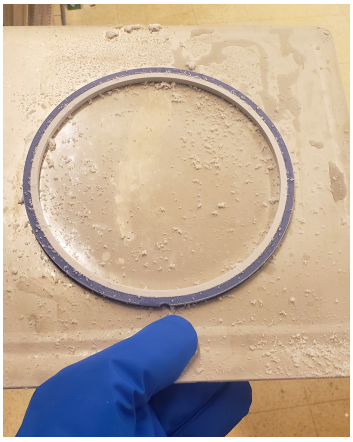

(a) Membrane frozen to a cookie sheet.

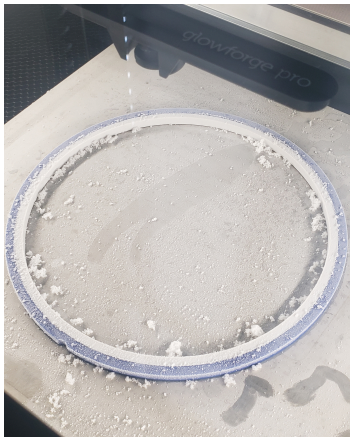

(b) Mounted in the laser cutter

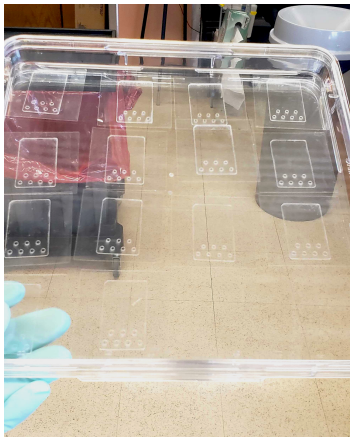

(c) A tray of laser cut membranes.

Figure 4-7: The frozen films are laser machined in a batch process to produce trays of laser cut parts.

that features of 0.5mm could be achieved. Additionally, the lasering process does not create fluorescent byproducts in any of the primary fluorescent channels as seen in **Figure 4-8**. This is important because the membrane cannot contribute fluorescent noise to the images of tissues in the chips. Further, fluorescent components in the membrane would be an indicator of new species being produced by the machining process. These byproducts might be toxic to cells or alter the bonding characteristics of the material.

4.3 Thermal Bonding

Assembly of the 5-layer chips was performed primarily using thermal bonding techniques. The materials developed for the thesis were designed to be easy to melt and bond to COC substrates. The use of TOPAS E-140 (T_m=84°C) makes it easy to design a bonding procedure that selectively melts the elastomer and does not deform the rigid layers of the chip. In **Figure 4-9** a TOPAS 8007s04 (T_g=78°C) chip is shown to undergo significant warping after a bonding procedure with too much heat and pressure; this implies that a higher temperature grade of COC, such as TOPAS 6015s04 (T_g=158°C) will be preferred.

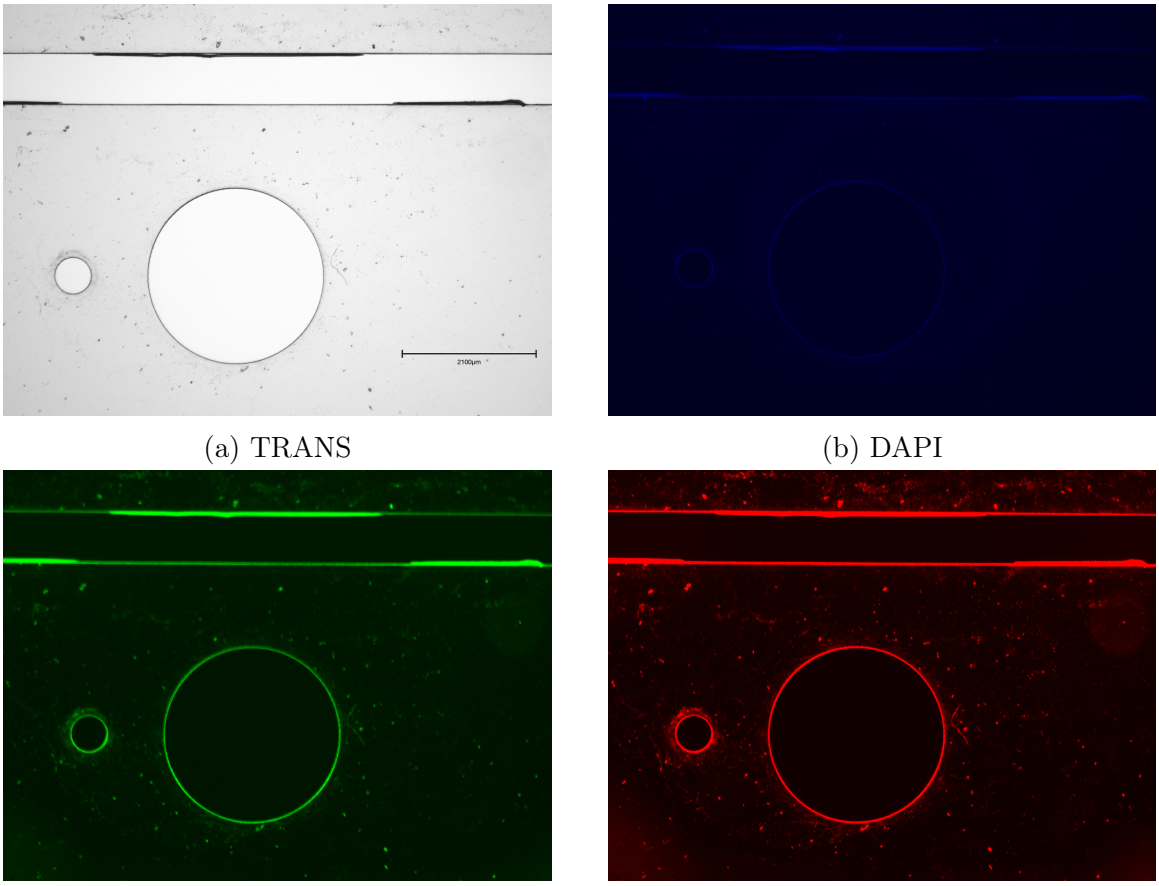

(a) TRANS (b) DAPI

(c) GFP (d) TX Red

Figure 4-8: Fluorescence evaluation of E-140 membranes fabricated using a femtosecond laser. A sample with a 1 mm wide slot, a 0.5 mm diameter hole, and a 2 mm diameter hole is shown and imaged with the excitation wavelengths of common biological assays: DAPI, GFP, and TX Red. There is some fluorescence at the edges of the cut, but this does not affect the surrounding regions. (a) White light image at 10x magnification. (b) Little to no fluorescence at 357 nm excitation. (c) Fluorescence at the edges of the cuts at 470 nm excitation. (c) Fluorescence at the edges of the cuts at 585 nm excitation.

Generally speaking, the E-140 films do not require much pressure to ensure a reliable bond; gently pressing devices to a hot plate at 84-100°C by hand can provide sufficient pressure for a bond. The bonding procedure should be hot (around 100°C) and fast. This makes it possible to melt the elastomer so that it becomes tacky and conforms to the bonding surface. The pressure should be applied uniformly so that all regions of the device are bonded. The process must be fast so that the elastomer material does not begin to flow in the melted state, which can cause migration of

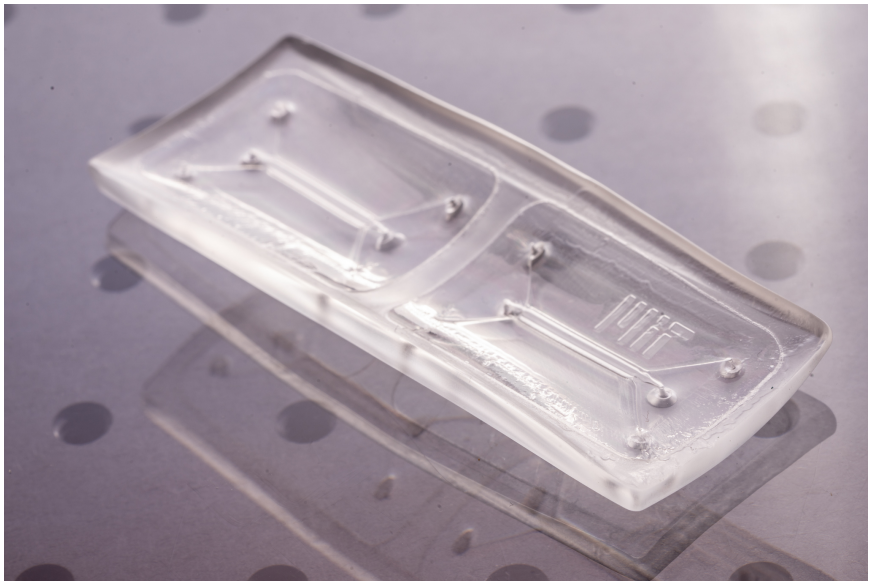

Figure 4-9: Warping of lower temperature grades of COC occurs if too much heat or pressure is used.

the elastomer material into the channels of the device as well as warping of any diaphragms in the device design.

The three main techniques for bonding these materials are (1) roll lamination, (2) bonding on a heat press, and (3) infrared bonding. Each technique has advantages and disadvantages that will be discussed below. It is worth noting that any other thermal bonding process can work provided the COC substrates are in contact and the E-140 layer reaches 84°C for a few seconds.

4.3.1 Roll Lamination

Roll lamination is the process of joining a thin film to another thin film or thicker substrate using rollers as a means to provide pressure to the bonding interface. The use of rollers creates a defined line of contact that forces bubbles out of the sealing interface and creates a stress concentration that results in strong bonds. This process can be used to join adhesive layers, and heat can be added to enable bonding thermoplastic materials.

A thermal laminator can also be used for joining thermoplastic elastomers onto a layer of a microfluidic device. For the lamination to work, the material must be

supported in some way throughout the bonding process. In this project, an elastomer membrane is used to create diaphragms for a microfluidic device. These diaphragms are ultimately freely supported members in the chip, and thus some sort of external support must be provided. In addition, a releasable carrier film should be used to prevent the material from sticking to the laminator or to the supporting materials. The laminated membranes should be flat and of uniform thickness, so a silicon wafer is suggested as a support material. A silicon wafer is uniform in thickness, adds minimal thermal mass to the system, and is thin enough to pass through a laminator.

For the chips in this thesis the laser cut E-140 membranes are first washed using 7X detergent (or Windex for mechanical prototypes) and DI water. They are then placed on a sheet of Parafilm and left to dry. Once the membranes are dry, they are transferred to 2 mil thick PET carrier film on top of a silicon wafer. Any trapped bubbles can be removed with a rubber roller as demonstrated in **Figure 4-10**. The membrane is then placed into a plastic dish and left to degas in a vacuum oven for a minimum of 72 hours at 65°C for reasons explained in Chapter 3.

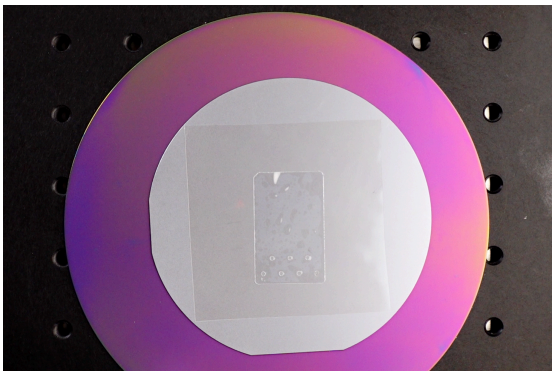

(a) Membrane transferred to an oversized high-temperature PET carrier film.

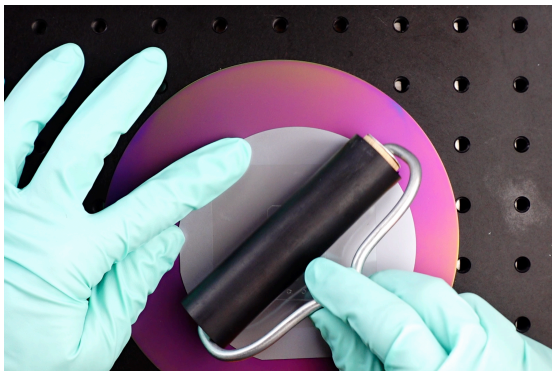

(b) Bubbles are removed with a handheld rubber roller.

Figure 4-10: Membrane is prepped for lamination by transferring the material onto a PET carrier on top of a silicon wafer. Parafilm may be placed between the membrane and roller to protect the membrane. The wafer is upside down in this demonstration to remove unwanted reflections and to better demonstrate the process; typically the polished side of the wafer is used to provide the smoothest surface for supporting the membrane.

After 72 hours the membranes can be removed from the oven. The pneumatic side of the chip is placed onto the membrane and visually aligned; this process is

made easier by looking at the reflections on the wafer. The pneumatic side of the chip is then passed through a GBC thermal laminator (**Figure 4-11**) 4 times; twice using the 3 mil setting and twice using the 7 mil setting. This setting does not change the temperature or pressure of the rollers, but rather the speed that the device passes through the machine. These settings will be similar for all brands of document laminators.

Figure 4-11: A chip getting sent through the thermal laminator.

Once the chip has been laminated, the part is left to cool. This only takes a few seconds and the part can then be lifted off of the wafer. The PET carrier film should remain on the chip until the next bonding procedure to protect the chip from collecting dust or getting contaminated. This process is very reliable, but the operator should take care to properly align the membrane. If the membrane is not aligned properly there will be loose fringes that could become a point of failure in subsequent manufacturing steps. An example of these fringes can be seen in **Figure 4-12**.

When assembled properly, these membranes are bonded with a strength near the tensile modulus of TOPAS E-140. To get an idea of the bond strength a laminated chip was connected to an air pressure regulator. The pneumatic line was connected to a 5 mm diameter diaphragm on the chip and pressure was gradually increased

Figure 4-12: A TOPAS E-140 membrane laminated to a TOPASE 6015s04 chip. The gray fringing is caused by poor alignment of the membrane.

from 0 psi until the membrane burst. At 28 psi the membrane started to plastically deform, but the membrane did not delaminate. At 29 psi the membrane ballooned up and finally delaminated from the chip. This test was recorded on video and some individual frames are shown in **Figure 4-13**. It is likely that these membranes could hold even more pressure if supported on both sides, but pressures exceeding 15 psi for microfluidic applications are very unusual. For all practical purposes this bond strength is more than sufficient for making reliable pumps, valves, and other diaphragm-based on-chip components.

4.3.2 Thermal Press

The optical film described in Chapter 3 was designed for fast and reliable bonding using a heat press. This material is designed to allow bonding at moderate temperatures and with a quick assembly process. More detail is provided in Chapter 3, but generally the material requires direct pressure from a heat press at 94°C for 22 seconds. The applied pressure should be around 5-10 MPa to avoid significant deformation of the elastomeric layer of the optical film. This pressure was determined by adjusting the applied torque on the #4-40 screws in the clamping fixture introduced

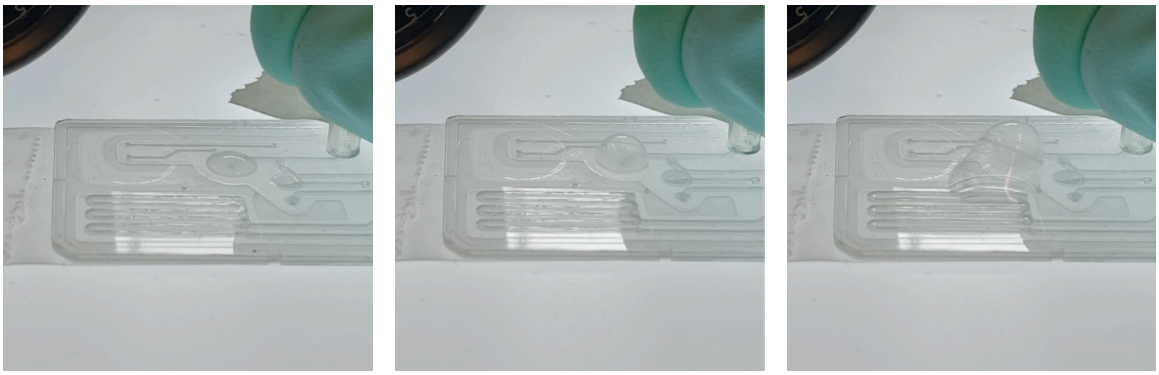

(a) 5 mm diameter membrane stable at 15psi.

(b) 5 mm diameter membrane deforms at 28 psi.

(c) 5 mm diameter membrane delaminates at 29 psi.

Figure 4-13: Pressure burst test for an unsupported 5 mm diameter E-140 diaphragm laminated to a COC chip.

in the section below and approximating the resulting clamping force. These values were also used to design the vacuum bonding fixture developed in Section 4.3.3. More testing should be conducted to identify the exact pressure, but this bonding pressure is far less important than the temperature.

A variety of heat press methods were used to bond the COC chips in this thesis, but the majority of early prototypes were assembled in a toolmaker's vise or in a custom metal clamp shown in **Figure 4-14**. The metal clamping system consists of a precision ground stainless steel plate with an array of #4-40 tapped holes. These holes are used to mount a 1.5 mm thick acrylic alignment bracket to the plate and the remaining holes are used to clamp another stainless steel plate onto the top of the chip. The alignment bracket also has room for high temperature magnets that can be used to push the chips into the corner of the alignment bracket. Tightening the 6 screws on each top plate clamps the layers of the chips together. Using a torque wrench and a washer under each screw helps to provide a uniformly distributed load onto the top of the chip. Up to 6 plates can be used at once to bond 6 chips at a time; an assembled clamp is shown in **Figure 4-14** with all 6 plates and the alignment bracket in use. The best bonded chips produced using this device were made by holding the chips at 84°C for 45 minutes in a convection oven. This allowed the system enough time to reach the melting point of TOPAS E-140 and then the parts were removed and left

to cool to room temperature.

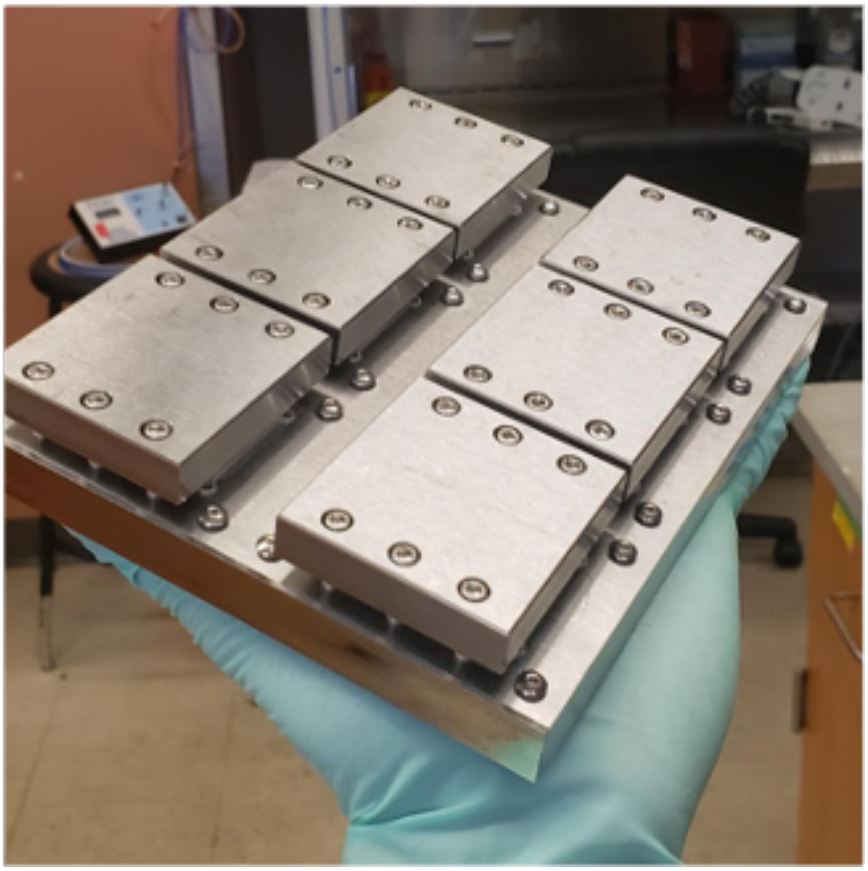

Figure 4-14: A fixture used for clamping and bonding 6 chips in an oven. The chips are aligned to an acrylic bracket with 3 magnets and then clamped between 2 stainless steel plates using 6 #4-40 screws.

Although this clamping mechanism was used to create a number of reliably bonded prototypes, it suffers from a number of flaws. First, getting the torque on the screws right is not an easy or consistent process. Usually one or more screws will end up at a higher torque than the others. Second, the fixture does not resist bending loads induced by the clamping force; as the screws are tightened down they cause a small deflection of the top plate that results in less pressure at the center of the chip. This effect is exaggerated as shown in **Figure 4-15** by using an acrylic top plate instead of tool steel. The lower modulus material deforms significantly and leads to bonding at only the edges of the chip. This effect occurs to a smaller degree in the steel plate.

This style of clamp is also high in thermal mass, and thus slow to reach an elevated temperature and takes a long time to cool down. This prolongs the heat exposure to

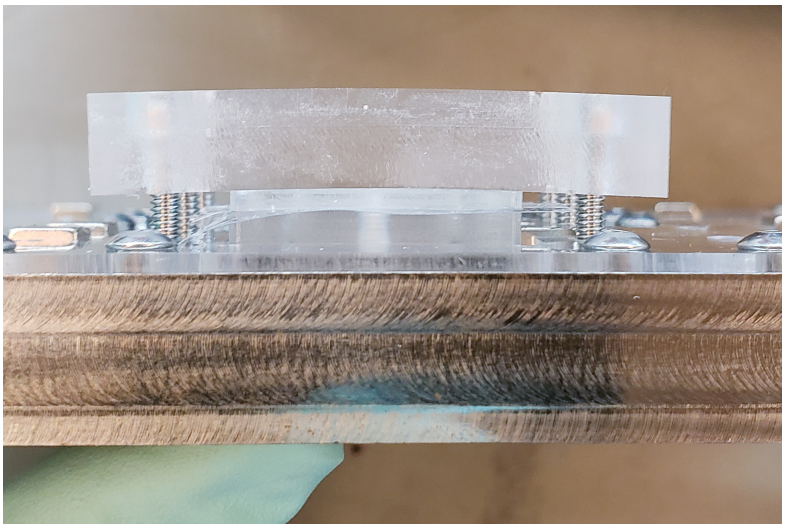

(a) The clamp is subject to bending loads and uneven pressure distribution. This produces higher pressure on the outside of the chip.

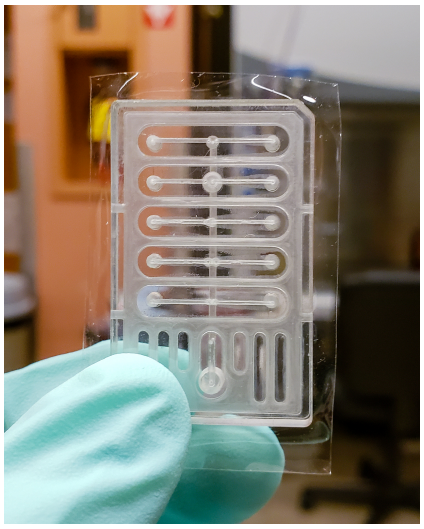

(b) Poor stress distribution causes bond failure at the center of the chip.

Figure 4-15: Uneven pressure distribution provided by the clamp results in poor bond strength and inconsistent results. (a) The effect of bending loads is amplified for illustration purposes by using an acrylic plate instead of steel. This bending leads to stresses. concentrated at the edge of the chip. (b) Bonding chips using this fixture results in weak or unbonded regions in the center of the chip.

the chip and can cause excessive displacement of the elastomeric layers. An example of this issue is shown in **Figure 4-16** where the deformation of the E-140 material can be observed. This can be avoided by using a faster heating and cooling process or by applying less pressure.

One of the biggest issues in thermally bonding chips with internal membranes is that any gasses trapped in the chip will expand when heated and produce a pressure that acts on the surface of the diaphragm. This pressure can cause the membrane to bond undesirably to other regions of the chip. For example, the diaphragm may get pressed up against a valve seat and create a permanent bond on the sealing surface. To eliminate this problem the gas can be allowed to escape through the venting system or through a porous part of the clamp such as a foam pad. The chip may also be bonded in vacuum so that no gasses are present in the chip.

Once some of these issues were identified it was decided that a thermal sublimation press might provide a good alternative to the steel clamping system. A thermal

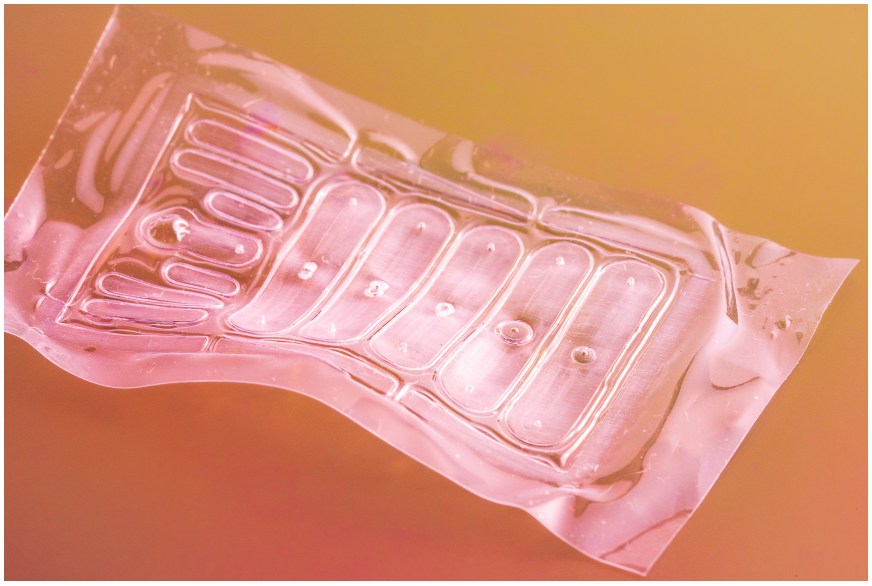

Figure 4-16: An E-140 membrane separated from a bonded chip shows significant displacement of the E-140 material in the bonded regions and warping of the diaphragms.

sublimation press is simply a compliant heating pad that presses down onto a foam pad. The heating element is stiffer than the foam pad and is mounted to a series of springs that help to level the clamp. The height of the heating element is adjustable to accommodate different thicknesses of materials and to change the clamping force.

A thermal sublimation press was purchased for around $200 and used to laminate all of the finalized chip designs produced in the later parts of the thesis. The press is set to 94°C and it takes a few minutes to heat up. The optical window is manually aligned to the top of the chip so that the edges of the window are slightly offset from the edges of the chip. The window is slightly tacky and temporarily holds to the chip. A close-up of this alignment procedure is shown in **Figure 4-17a**. The chip is then placed onto the foam pad of the sublimation press and centered under the heating pad with the optical film on top. The heating pad is then pressed down onto the chip via a toggle clamp mechanism (**Figure 4-17b**) and a timer is set for 22 seconds. The pressure from the mechanism is set to very light but higher pressures may be used be adjusting the press.

When bonding a membrane between 1mm thick layers of a chip the timer is set to 91 seconds; this is roughly 300% increase in bonding time to account for the 300%

increase in distance that that heat needs to travel to reach the bonding surface. These values may change slightly for future device designs but have been shown to work well for all of the finalized chip designs in this thesis. The sublimation press does a satisfactory job at allowing gasses to escape during the bonding procedure but occasionally the membranes will stick to unwanted surfaces in the chip. Typically, to solve this problem, the membrane is bonded first and then subsequent laminations of the optical film are fast enough to not heat the center of the chip.

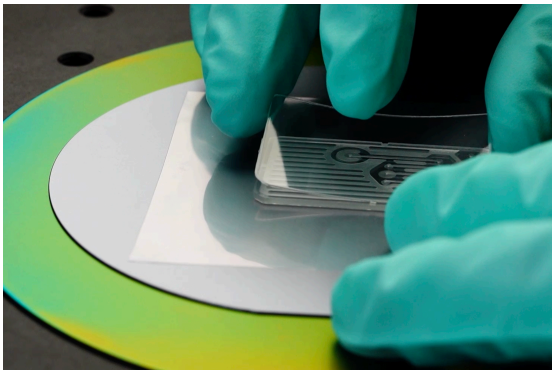

(a) Manual alignment of the optical film to a layer of the chip.

(b) Bonding the chip at 94°C for 22 seconds using a gentle amount of pressure.

Figure 4-17: Alignment of the optical film and bonding the chips on a sublimation heat press.

4.3.3 IR Bonding

A sublimation heat press works well for bonding the optical laminate to the top and bottom of the chips but a better process is desirable for improved reliability and yield. In particular, a more controlled process would allow for higher quality membranes as well as diaphragms of larger sizes due to better thermal control. An ideal manufacturing process would selectively deliver heat to the rigid substrate of a chip and the membrane would melt to it without excessive heating. Further, the bonding process should occur in vacuum so that no gasses are present in the bonding procedure.

One option for selectively delivering heat to the bonding surfaces is to use IR light as a heat source. The COC materials used in this thesis are IR transmissive up to

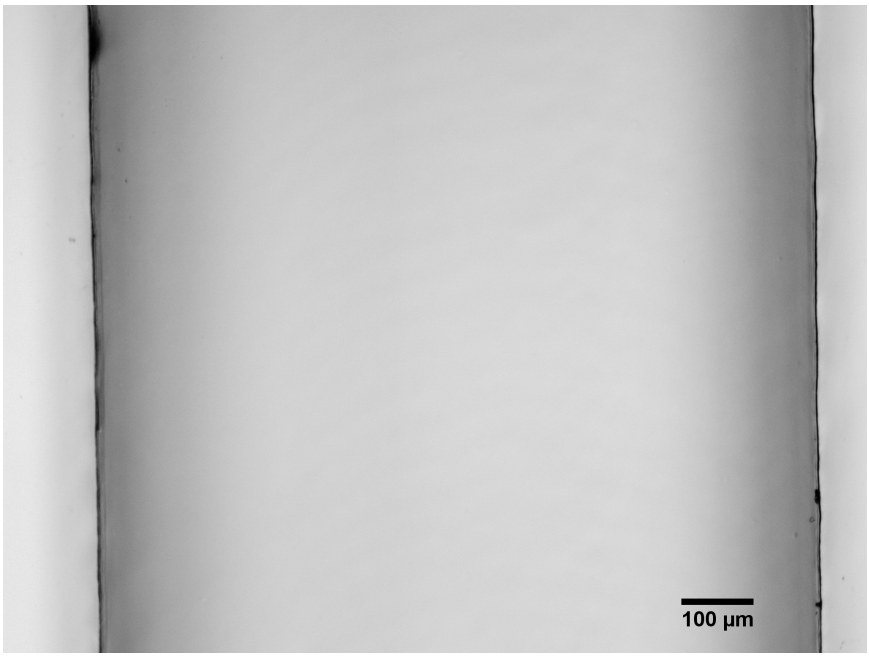

Figure 4-18: An image of a 1 mm wide channel with the bonded plane in focus. Optimal bonding parameters produce clear channels and preserve the channel edges.

1100-1200 nm wavelengths and thus do not heat up when exposed to IR wavelengths. To make one of the layers absorb IR, carbon black or Clearweld (an IR absorbing additive) can be added to the bulk polymer composition. This allows for one layer of the chip to absorb IR and heat up via radiation. By projecting IR through the clear layers the black layer will get hot and thereby melt the elastomer interface.

An initial experiment was conducted to see if this technique could be used to bond the COC optical laminate to a chip impregnated with carbon black. A black acrylic part was machined to have 2 thru-hole pockets with an 800μm wide and 200μm deep groove that is used as a datum for a 0.5" diameter COC optical film window. The optical windows were then aligned to the groove with the elastomer side down. The chip is then placed with the windows facing up into a vacuum press made of an aluminum vacuum chuck, a foam gasket, and a quartz window placed on top. When vacuum is applied to the chuck, the quartz window seals onto the gasket and presses down onto the chip as seen in **Figure 4-19a**. This proves a clamping force that puts the elastomer material into contact with the acrylic chip. An R40 IR heat lamp was then placed above the assembly for 45 seconds. At this point the acrylic/elastomer

interface appeared black, indicating a weld between the two materials. The part was then left to cool for several minutes before the vacuum was released. The bonded chip is shown in **Figure 4-19b and 4-19c**.

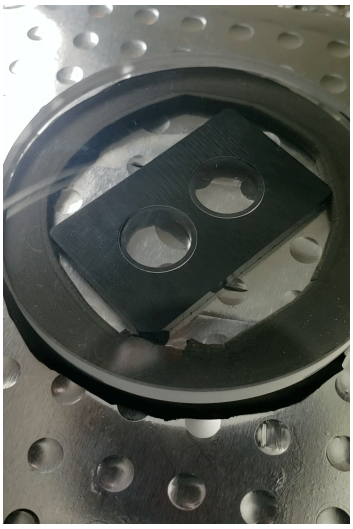

(a) Quartz vacuum press with a foam gasket.

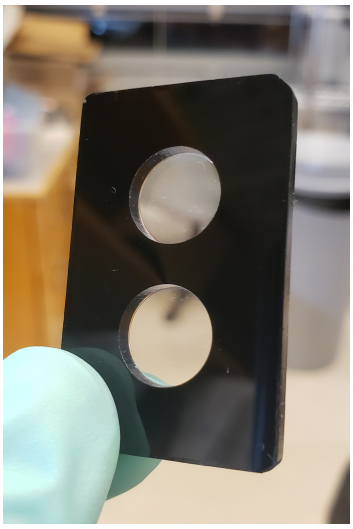

(b) Top view of finished chip.

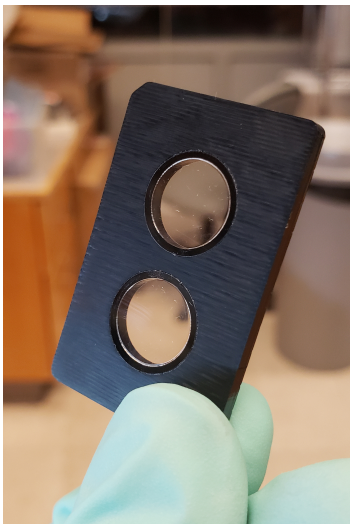

(c) Bottom view of finished chip.

Figure 4-19: COC windows bonded to a black PMMA chip using and IR heat lamp for selective heating through a vacuum clamped quartz disc.

This bonding process creates a clear and strong weld between the two dissimilar materials. This technique could be used to weld COC optical windows to a variety of materials, for example, to bond an E-140 membrane between two thick polymer substrates. Further, with the process done in vacuum unwanted pressurization of internal diaphragms is much easier to avoid. As a demonstration, a 10mm diameter E-140 membrane was welded between black and clear rings machined out of TOPAS 6015s04 wafers. The same bonding process was used to create this weld, and the result is pictured in **Figure 4-20**. This sets a foundation for being able to bond larger diameter membranes, as well as membranes with thermoformed geometries without risking damage to the membrane material. This may be desirable for larger pump chambers, fluidic capacitors, and for bonded elastomeric scaffolds.

The IR bonding fixture was then modified to have a larger quartz window and an acrylic bracket that the window fits into. This generates a partial seal around the window and removes the need for a gasket that undesirably resists the clamping force.

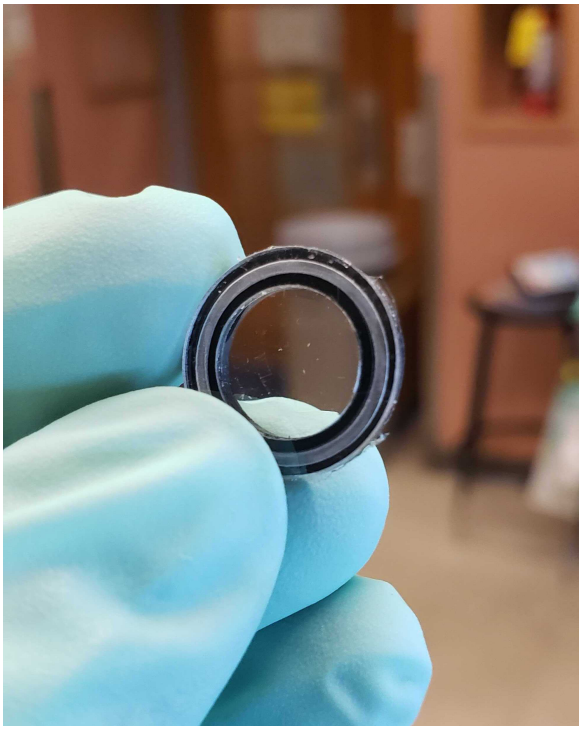

Figure 4-20: A 10mm diameter E-140 membrane bonded between 2 COC rings.

In addition, a 1/16" thick IR transmissive silicone sheet was added under the quartz window to distribute the applied pressure onto the chip. A diagram of this setup is provided in **Figure 4-21**. The setup was then used to bond a few COC chip designs with integrated pumps and valves. The bonding procedure is fast, and consistently delivers bubble-free bonds in the middle of the chip without deforming the top and bottom layers. A view through the quartz window and an example of a chip bonded using IR are provided in **Figure 4-22**

This bonding process is not yet perfected and the IR heat lamp often generates too much heat for a well-controlled bonding process. The silicone sheet and flatness of the vacuum chuck also prevent gasses from escaping the chip and sometimes results in warped or welded diaphragms. A more controlled process will likely use a wavelength of 980nm and leverage a photomask for protecting the diaphragms. Eventually the IR bonding process is a promising candidate for joining a laminated pneumatic layer of a chip to the fluidic side of the chip. With more refined equipment and more trials these bonding parameters can be optimized and should lead to more consistent

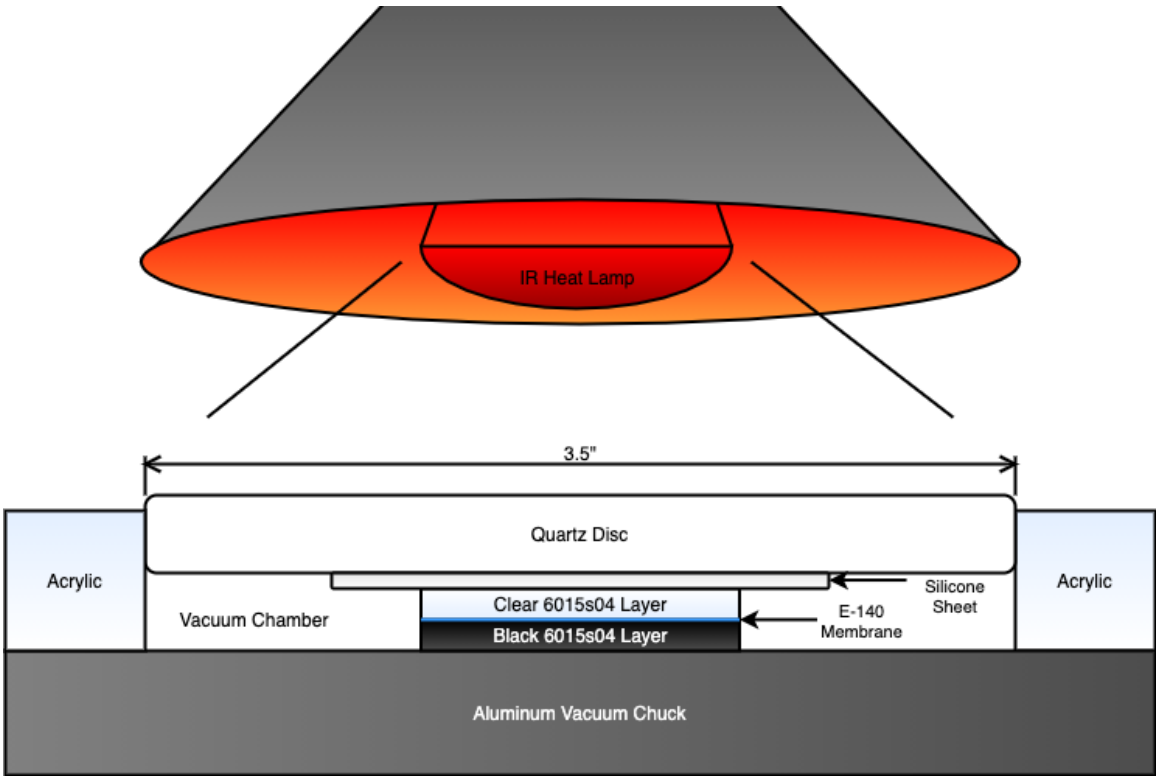

Figure 4-21: Setup for bonding chips using an IR heat lamp. A quartz disc is pulled down using vacuum to preload the bonding process.

results.

Many commercial IR systems exist for bonding devices using IR lasers, but a machine that uses a scan laser (Ex. Leister Laser Systems) is a preferred choice. This allows for light to be spread out more evenly across a chip and and for one region of the chip to be welded at a time. This is important because regions with pumps and valves may need less exposure time than regions with larger bonding surfaces. The prototypes produced using this method had the strongest bonds and least amount of bubbles. They are of extremely high quality and show the most promise for manufacturing parts at scale. The infrared welding process can be automated so that partially assembled chips are welded together quickly in a clean and controlled environment.

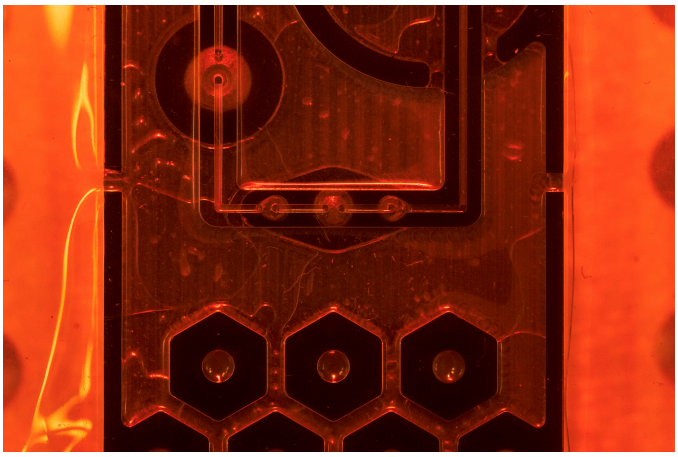

(a) A chip in vacuum press under IR illumination.

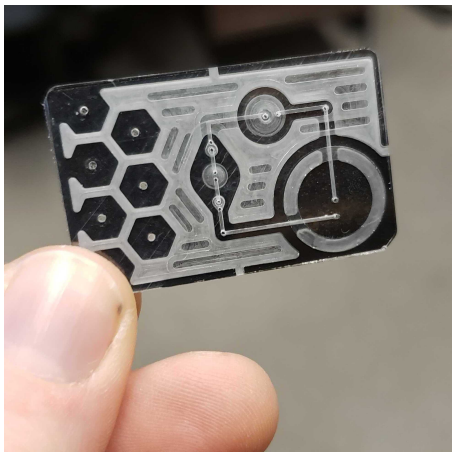

(b) A chip bonded using IR.

Figure 4-22: A 3 layer prototype of a chip with an integrated pump bonded using IR illumination.

4.4 UV Curable Adhesive

For most of the chips in this thesis a fluid reservoir is required for media storage. These reservoirs will eventually be injection molded directly on the chip, but for present prototypes can be joined using a UV curable adhesive for prototypes. Dymax 1072-M was selected as a good adhesive for joining external parts to COC due to its low autofluorescence, low water absorption, as well as solvent resistance. A 400 μL reservoir bonded to a microscope slide is shown in **Figure 4-23**. This technique could be used to join a variety of components and materials to the chips, but ultimately adhesive bonding should be avoided. Adhesive bonding is best suited for attaching additional components, such as sensors, to a chip for a prototype or measurement. Dymax 1072-M, for example, has unknown biological interactions and sometimes dissolves when exposed to ethanol and other organic solvents for extended periods of time. Application of the adhesive can also be hard to control and the bond strength between different materials is not fully defined. This adhesive is elastomeric in nature and might also contribute to the absorption and adsorption of small molecules in the chips.

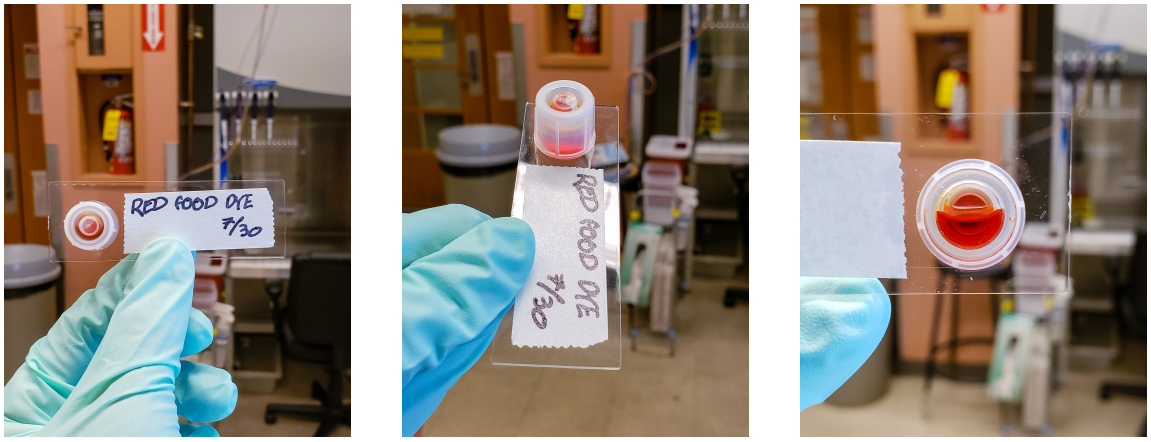

(a) Top View (b) Side View (c) Bottom View

Figure 4-23: UV curable adhesive (Dymax 1072-M) can be used to reliably bond liquid tight features to a microfluidic chip.

Chapter 5

Fluidic Control Elements

The integration of membrane-based fluid control elements into microfluidic chips opens up a wide range of fluid control possibilities. The most important building block features for a comprehensive microfluidic control system include: pumps to displace fluid, valves to gate fluid flow, pressure regulators to control system pressure, and accumulators to add fluid capacitance. By combining these elements in series and parallel, a circuit may be designed to meet a wide range of fluidic conditions.

In this chapter, a process for designing and optimizing thin elastomer membrane elements is presented and used to design a pump chamber, a valve, and a pressure regulator. In addition, a novel fluidic accumulator is introduced that uses trapped gas bubbles as an energy storage element for a microfluidic channel. These components are integrated into a functional pump design which is then combined with a pressure control system to provide a more stable flowrate.

5.1 Design of Elastomeric Membrane Elements

A 2D FEA model was built to study the motion and performance of E-140 diaphragm elements. The model was used to optimize the geometry of a valve seat and to design a reliable pump chamber with a displacement volume of approximately 1 μL. These designs were then implemented in hardware prototypes and tested using pressure and flow sensors. A finalized pump configuration was selected using the optimal pump

chamber and valve design.

5.1.1 Membrane Simulations

To accurately predict the motion of elastomeric diaphragms an appropriate material model must be selected. The E-140 membrane is a semi-crystalline thermoplastic elastomer and behaves similarly to a rubber or urethane material. For this reason a Yeoh model [111] was selected to describe the shape of the E-140 stress-strain response. The material manufacturer did not agree to share the raw test data for the E-140 grade, so an approximation of the stress strain response was generated by linearly scaling a Yeoh model for polyurethane provided in ANSYS to match the spec sheet modulus of E-140. To do this, the raw data provided in ANSYS for polyurethane was normalized at the listed tensile stress at break and then multiplied by the modulus of E-140; spec sheet values predict a stress of approximately 46 MPa at 500% strain with an initial tensile modulus of 68.9 MPa based on the ISO 527-2/1A/1 test standard [101]. This data was implemented accordingly for the uniaxial test data and the resulting approximate stress-strain curve is provided in **Figure 5-1**. The tensile modulus defines the initial slope of the curve and the data past the modulus predicts the plastic deformation of the material. Ideally, the stress-strain curves should be generated using ASTM standards for elastomeric materials, but this would have required more time and expense than the project allowed. Further, these studies took place during the 2020 COVID-19 lockdown when generating actual test data was not possible. Future testing should be conducted at 37°C to better characterize the material for use in an incubator.

The ANSYS model was set up as a 2D axisymmetric structural simulation. The membrane was modeled as a 50 μm thick material with a minimum of 3 finite elements along the thickness of the membrane; without 3 or more elements the bending modes and stiffness of the membrane cannot be properly simulated. The bodies of the chip are assigned as a rigid material, because deformations in the bulk material will be very small compared to deformations in the membrane. Joints between the membrane and chip are set as bonded elements. The amount of mesh elements was maximized

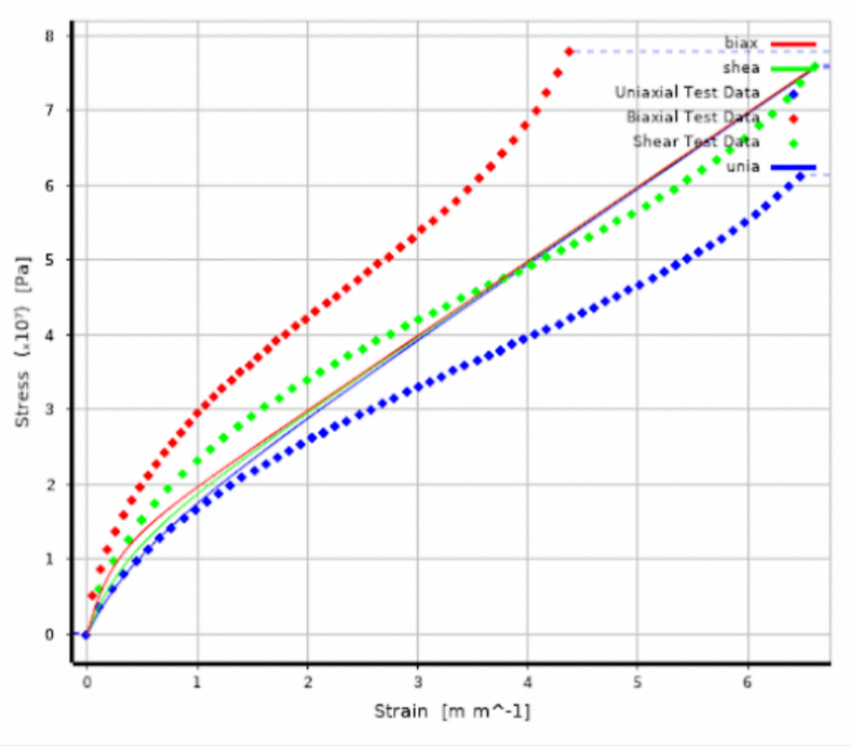

Figure 5-1: A Yeoh material model used for simulating the stress-strain response of TOPAS E-140. This model provides a relationship between the stresses (in Pascals) experienced by the material to an applied strain (meters/meter). The only known parameters for TOPAS E-140 are the uniaxial stress of 46 MPa at approximately 500% strain (5 m/m in this graph) and the tensile modulus of 68.9 MPa, which defines the initial slope of the uniaxial stress curve. The biaxial and shear data are proportional to the data for polyurethane and are automatically scaled in ANSYS. The resulting Yeoh model (solid lines) is used to predict the actual deformations of the E-140 material to an applied load.

to provide the best results.

The goal of these studies was to design a new pump chamber and an improved valve geometry. The pump chamber should evenly distribute stresses across the diaphragm as it deflects, and also make sure that no fluid volume is trapped in the chamber when fully deflected, so as to create an accurate volumetric flowrate. In previous pump designs there was a stress concentration at the edge of the diaphragm that caused fatigue of the membrane and a small amount of fluid would get trapped in the edges of the pump chamber.

A variety of pump chamber geometries of equal displacement volume were compared. Specifically, a 2 mm diameter bore with no supporting structure, a spherical

cap with a 1mm radius and 0.31 mm thickness, and two chambers with continuously varying geometry were compared. The designs were all normalized to have roughly the same displacement volume, and a simulation was performed to see how the membrane would respond to an applied pressure of 5 psi. The displacement volume of each fluidic chamber is 0.5 μL in the simulation but in operation would be twice that volume in an actual pumps due to symmetry of the pneumatic and fluidic layers. That is, the net displacement of the chamber is 1 μL.

The spherical cap geometry provides a good baseline because it is easy to determine the displacement volume mathematically and to design the geometry in CAD. Unfortunately, the simulation validates the concern that fluid gets trapped in the edges of the chamber. A 2 mm diameter chamber with a depth of 0.31 mm depth is shown in **Figure 5-2**.

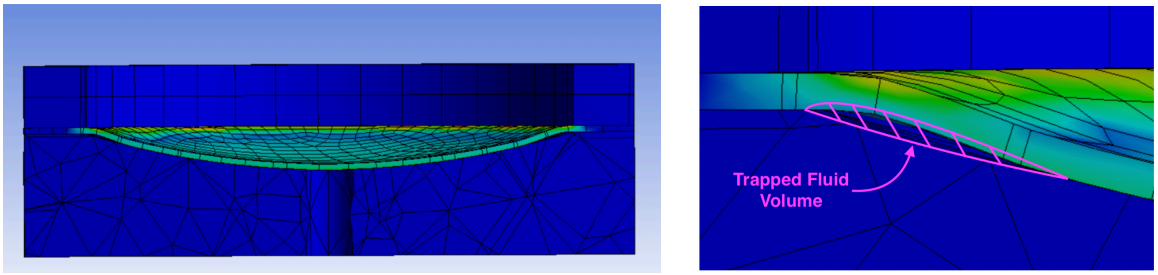

Figure 5-2: A spherical cap geometry does not provide relief for the membrane and results in trapped volume at the edges of the diaphragm, as highlighed in pink.

The proposed alternative pump chamber design consists of two continuous arcs that are tangent to the membrane surface. These arcs perform 2 key functions: first, they provide support to the edges of the diaphragm; as the pressure is applied the membrane it will first contact the edges of the pump chamber and then move to the center of the chamber. This pushes fluid volume from the outside of the chamber to the center so that no volume gets trapped in the chamber. Second, the shape provides support to the membrane so that the stress concentration at the edges is distributed across the membrane. In an optimized geometry this implies that the membrane is under uniform tension and is not resisting bending loads. A simulation of a tangent-arc pump chamber is shown in **Figure 5-3**. The geometry can also be

scaled so that larger or smaller pump chambers can be designed into future chips.

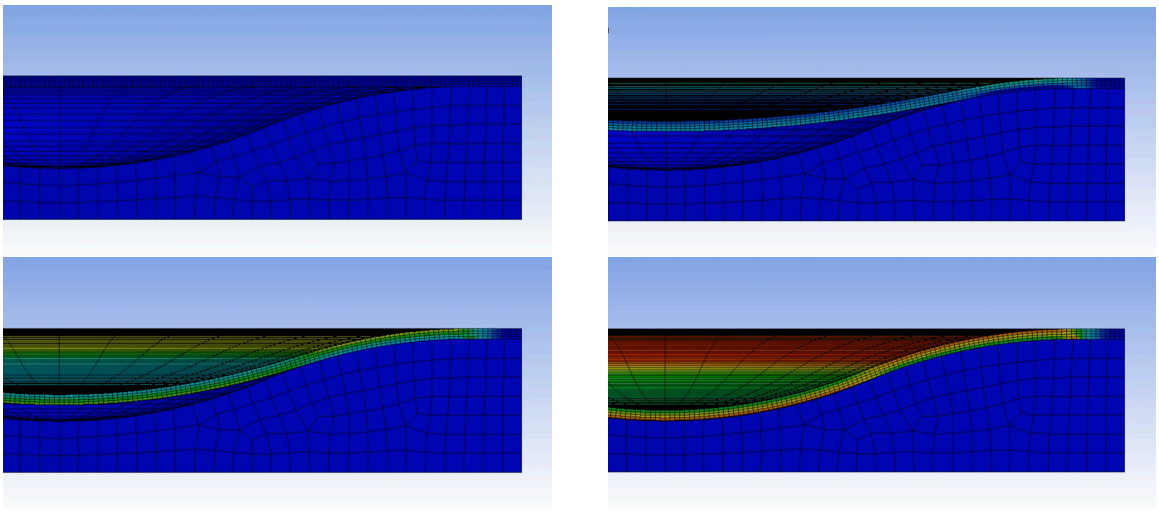

Figure 5-3: Simulation of the new pump chamber demonstrates fluid displacement from the outside of the chamber to the center. The geometry also helps to distribute stress concentrations in the membrane.

The tangent arc pump chamber is a low-stress design featuring a maximum strain of only 4% across the membrane surface. This should help to reduce fatigue on the membrane and lead to a more reliable pump design. Long term reliability studies are of lower priority since the chips are intended to be disposable, but this may be worth studying in future systems.

The model was then used to optimize the valve design. In a doormat valve [67] the sealing pressure does not exceed the applied pressure to the membrane. This is undesirable because this requires relatively high pressures to be used for actuating the valves. Higher pressures can be harmful to cells and imply slower switching times when vacuum is applied. It is also unclear where a doormat valve is sealing, and thus they can have unpredictable performance.

To improve the valve design, a defined sealing feature was evaluated. The selected geometry was a 0.2 mm radius ring-shaped feature that is as small as possible under our machining process. The valve volume is a parasitic pumping mechanism that we would like to minimize. The ring creates a stress concentration in the membrane at the valve outlet and makes sure that fluid cannot pass under the ring due to the high contact pressure at the ring. Additionally, the tension in the surrounding membrane

acts as a mechanical amplifier to provide more stress on the ring. The valve geometry was made as small as possible in the model; the overall diameter is only 3.0 mm and the chamber is only 150 μm in depth. In future simulations the overall diameter was reduced to 1.5 mm. This was originally predicted as the smallest possible valve, but actual prototypes were able to be machined at a smaller diameter of only 1 mm. In **Figure 5-4** the valve seat is shown with a stress concentration on the sealing interface. The model predicts that the stress at the sealing interface will be amplified by a factor of 32 with an applied pressure of 10 kPa and a factor of 54 with an applied pressure of 50 kPa. Note that this is not the predicted sealing pressure, but does suggest better sealing characteristics.

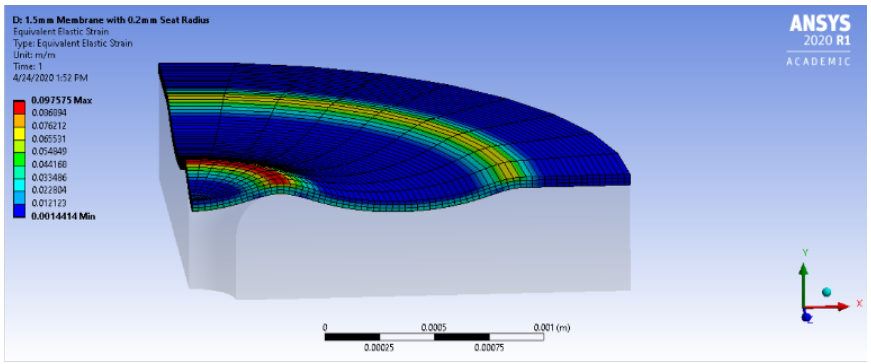

Figure 5-4: Simulating the valve sealing characteristics using a 2D model in ANSYS. The tension in the membrane acts as a mechanical amplifier to create a stress concentration on the valve seat.

5.1.2 An Integrated COC Micropump

The pump chamber and valve designs were then integrated into a pump prototype. The pump chip consists of 5 pump bodies connected to PTFE tubing using NOA81 UV adhesive. The chip was bonded using the clamp described in Chapter 4 in an oven at 84°C. The bonded chip is shown in **Figure 5-5**. The chip is made out of machined COC layers and uses a laser-cut membrane. The pneumatic connections are push-to-connect fittings that are screwed into the top of the chip and connected to 1/16" OD tubing.

A photo of the internal geometry of the chip is provided in **Figure 5-6**. This

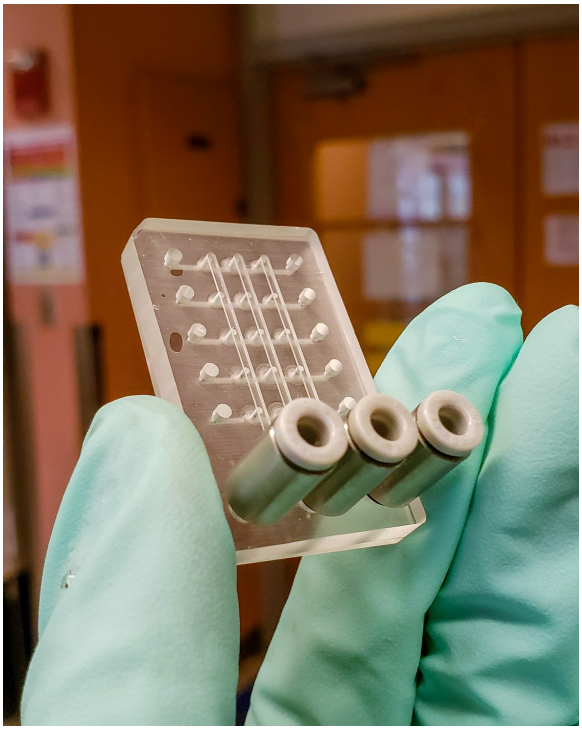

Figure 5-5: A microfluidic chip with 5 integrated micropumps made entirely out of COC.

image helps to show the size of the valves relative to the pump chamber and the intended flow direction. There are a few burrs in the machined part but these burrs were removed using a tiny drill bit prior to bonding.

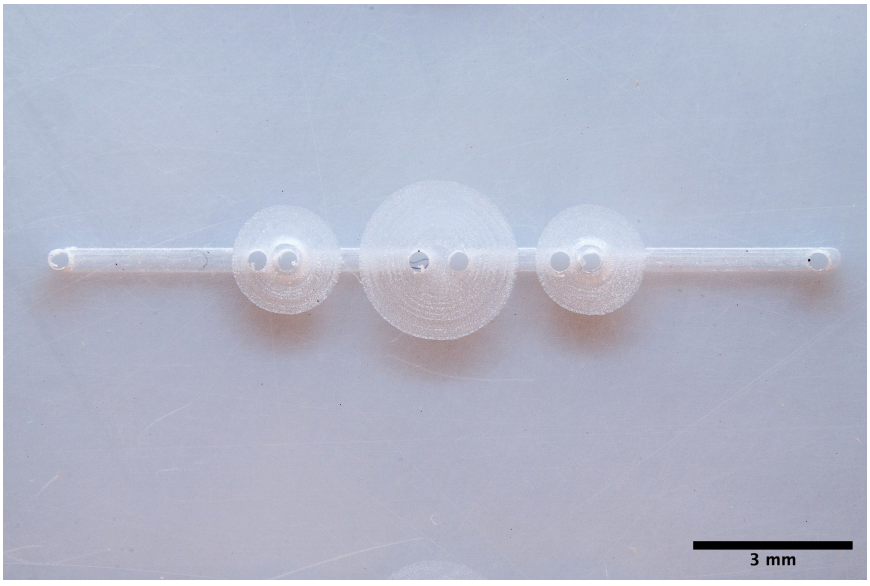

Figure 5-6: Internal geometry of the original COC micropump.

After assembly, the pump was connected to a Sensirion LPG10-1000 flow meter [112]. This flow meter is a thermal flow meter designed specifically for microfluidic applications. The sensor is fast enough to capture some of the higher frequency components of the flow from the pump, and the nature of the sensor makes it good at calculating the average flowrate by means of a moving average. The raw data from the sensor, provided in **Figure 5-7**, shows that the pump is able to provide an average flow-rate of 60 μL/min. The pump is pulsatile in nature and does not provide a consistent flowrate. With each stroke of the pump chamber an instantaneous flowrate of approximately 400 μL/min peak is observed. Further, the valves create instantaneous flowrates of around 200 μL/min peak and displace a significant volume of fluid. This valve displacement does not contribute to the average flowrate because each displacement of volume from the valve is associated with an aspiration of fluid back into the valve. The exact behavior of the valves is hard to visualize due to the low sampling rate of the sensor. With a higher sampling rate the shape of these curves would be easier to capture. Much faster sampling times are possible with the LPG10-1000, but this comes with a tradeoff for resolution. This feature of the sensor was not discovered until after most of the fluidic testing was finished.

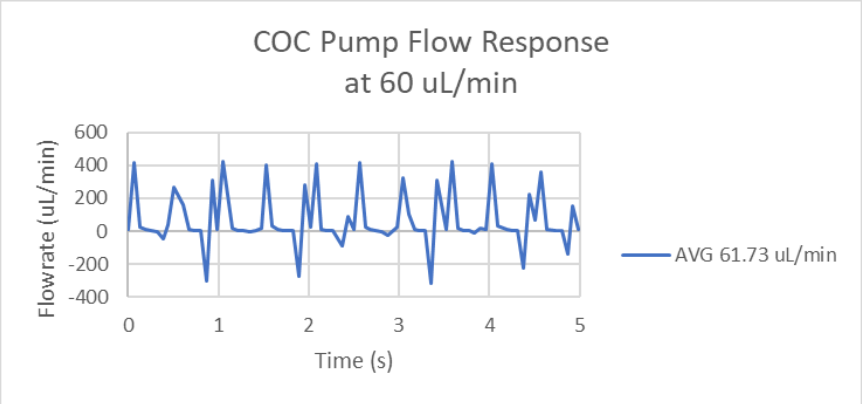

Figure 5-7: Flow characteristics of the original COC micropump. The valves produce a significant amount of fluid displacement but the average flowrate is not affected.

Although the pump was able to provide the desired average flowrate of 60 μL/min it is desirable to have a pump that provides more constant flow and and which also has reduced valve volumes. A smoother flow will provide a more gentle velocity, so

as not to stress cells in culture. The pump chamber appeared to work very well, and was used for the remainder of the project. The control of the pump could also be improved by using an electronic pressure regulator to control the pressure on the diaphragms to transition more gradually. The pump works with an applied pressure of only ±4 psi, but a higher pressure of ±7 psi ensures that the pump can push against a greater head pressure. Based on the FEA simulations the pump only requires ±1 psi to actuate, but such a low actuation pressure remains untested.

5.1.3 Valve Geometry Optimization

One of the ways to improve the pump design is to use a different valve. A lower volume valve would lead to more stable flow. Although the 2D ANSYS simulations help to get an idea of what types of valve geometries make a good seal, they do not accurately predict the leak characteristics of a valve. Further, the 2D simulation does not allow for designs with more complicated 3D geometries. A valve's performance needs to be measured experimentally by applying a pressure and recording the leak flowrate.

A variety of valves were designed as a design performance study. The original doormat valve [63] was used as a baseline and compared to: (1) the 1.5mm diameter ring valve, (2) a teardrop shaped valve with the same ring-shaped feature as the 1.5mm ring valve, (3) a figure 8 shaped valve with two sealing rings, and (4) a weir valve that features a small flat surface between the inlet and outlet.

These valve designs were CNC machined and assembled into a chip with a single pneumatic port which actuates the valves. The fluidic side of each valve was connected to PTFE tubing using NOA81 UV adhesive. The tubes were also connected to an acrylic bracket to help with sealing and to provide a strain relief. The assembly of this chip highlighted in **Figure 5-8**. Water with food coloring is used to show that the valves permit fluid flow and are not bonded shut.

The chip was then connected to an upside-down Falcon tube filled with DI water. The Falcon tube is converted into a pressurize fluid source by adding a tube through the bottom of the cap and connecting it to an external pressure source. The fluid

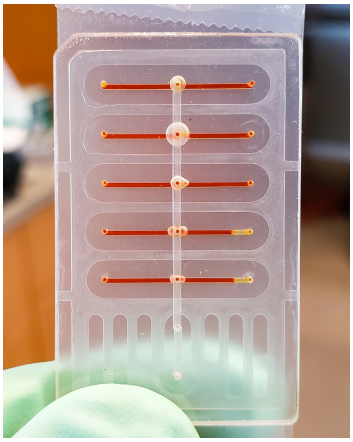

(a) Valve profiles.

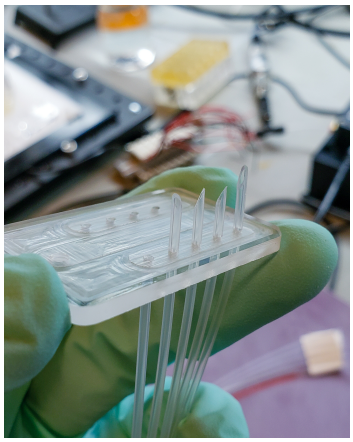

(b) Tubing connections.

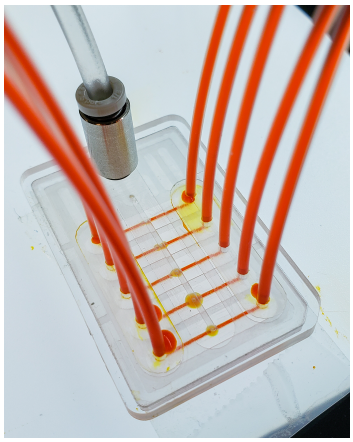

(c) Final test setup.

Figure 5-8: Test chip featuring 5 valve designs and sealed using scotch tape and connected to 1/32" OD PTFE tubing.

pressure was monitored using a 0-10 psi pressure sensor. The pneumatic port was connected to an external 0-10 psi pressure regulator; this acts as the applied sealing pressure to all 5 valves at once. The outlet of the valve chip is connected to a Sensirion LPG10-1000 flowmeter and then connected to another upside down Falcon tube with a vent. Both tubes are elevated by about 12" above the chip so that the hydrostatic pressure is balanced. Note that the flow sensor is placed at the outlet of the chip so that any leak at the chip-tube interface do not corrupt the outcome of the test. This works because the fluid pressure on the valve is the same regardless of whether there is a leak upstream or not. If the flow sensor were upstream, it would be recording the leak flowrate of the valve as well as the leak flowrate of the tube interface. Leaks downstream are less likely because this part of the chip is at a lower pressure. A diagram of this setup is provided in **Figure 5-7**.

First, the setup was used to test the sealing characteristics of the original doormat valve as compared with the new ring valve over a range of applied pressures. This was done connecting the PTFE tubing to an old pump design and to the pump in **Figure 5-5**. The pump chamber and one valve were held open using vacuum so as to isolate one valve for the test. This helps to get an idea for the best applied pressures to use for further testing. In both cases only a few actuation pressures are used to get a sense of the required actuation pressure. The sealing characteristics of the doormat

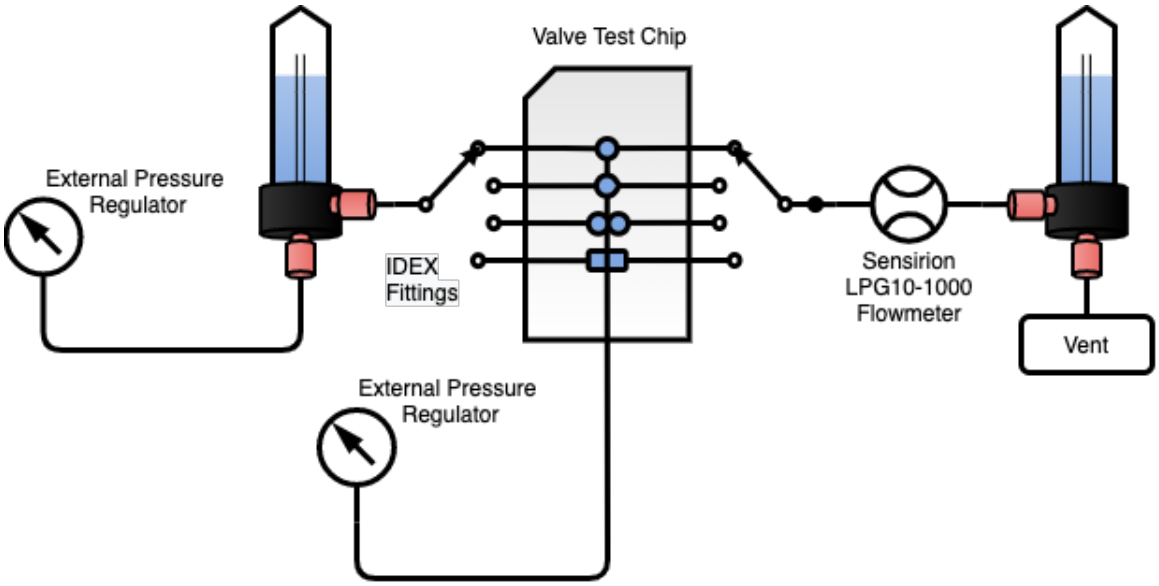

Figure 5-9: Test setup for comparing the proposed valve designs.

valve are presented in **Figure 5-10a** and the sealing characteristics of the ring valve are presented in **Figure 5-10b**. The key results from this test are that the ring valve appears to seal better than the doormat valve and even seals at pressures higher than the actuation pressure. The doormat valve only seals up to the applied pressure, but appears to leak at all applied pressures.

The test was difficult to run at higher head pressures and lower valve actuation pressures for a number of reasons. First, the pressure regulator used to actuate the valve does not open until approximately 0.25 psi which limits the lower range of possible test conditions. Second, the flow meter tends to have a bias of 1-2 μL/min so an actuation pressure of 0 psi might read anywhere from 0-2 μL/min even if no flow is present. With low actuation pressures, the valves are also sensitive to the hydrostatic pressure generated by the difference in liquid height between the two reservoirs. This is exemplified in **Figure 5-10b** where 0 psi of applied head pressure results in approximately 300 μL/min of flow. At higher head pressures, the valves do not seal very well and significant amount of fluid leak through the valve. In many cases, this resulted in enough fluid transferred between the reservoirs that the test needed to be reset. Additionally, the higher head pressures caused a few leaks in both pumping platforms. For these reasons, 5 psi was selected as the actuation pressure

for further testing to compare different valve designs.

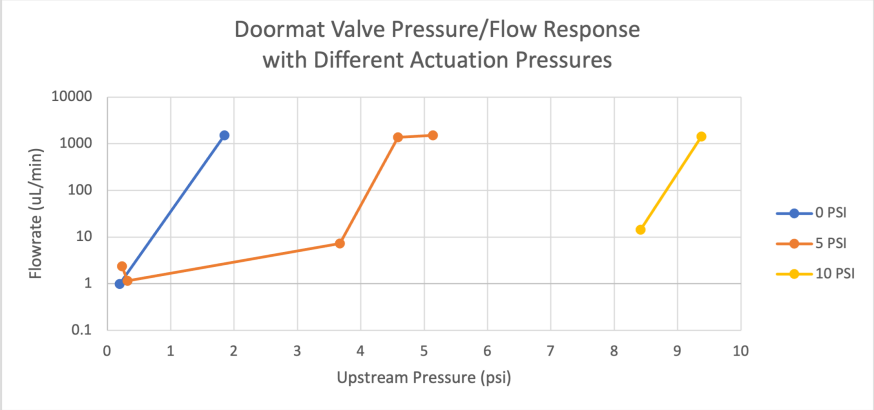

(a) Sealing characteristics of the original doormat valve.

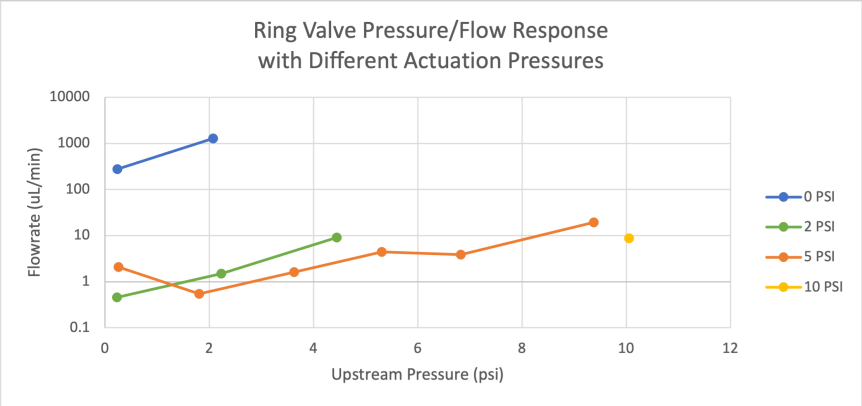

(b) Sealing characteristics of the ring valve.

Figure 5-10: Sealing characteristics of the original valve design and the new ring valve design. Data was generated by isolating a valve in a pump platform and applying a head pressure. The leak flowrate of the valve is recorded using a flowmeter. The doormat valve leaks more at lower head pressures as compared to the ring valve and opens when the head pressure equals the actuation pressure. The ring valve is able to generate a strong seal up to the actuation pressure and continues to seal beyond the actuation pressure.

Next, the 5 valve designs were compared using an actuation pressure of 5 psi and a range of upstream pressures in increments of 0.5 psi starting at 0.5 psi and ending when the flow sensor saturated at approximately 1000 μL/min. This data is presented in **Figure 5-11**. The figure 8 and weir valves leaked immediately and may have been too small for the bonding procedure. It is probable that the membrane bonded to the pneumatic side of the chip and thus the valves were essentially open for this test. The doormat valve and ring valve exhibit a similar response as before. The ring

valve does a better job at sealing for lower pressures and the doormat valve tends to leak well below the actuation pressure. The teardrop valve was shown to seal very well at lower upstream pressures and only begins to leak when the upstream pressure exceeds the actuation pressure. This result may be different from the previous study for two reasons. First, the doormat valve is made of a different material in this test. The original evaluation used polyurethane and the valve test chip was made of COC, a thicker and stiffer membrane material. Second, the ring valve was pressurized in the opposite direction. All of these valves seal in both directions but the ring and teardrop valves perform best when the head pressure is applied in the center of the valve. It is also worth noting that this ring valve is a slightly different geometry, 2 mm in diameter instead of 1 mm in the COC pump.

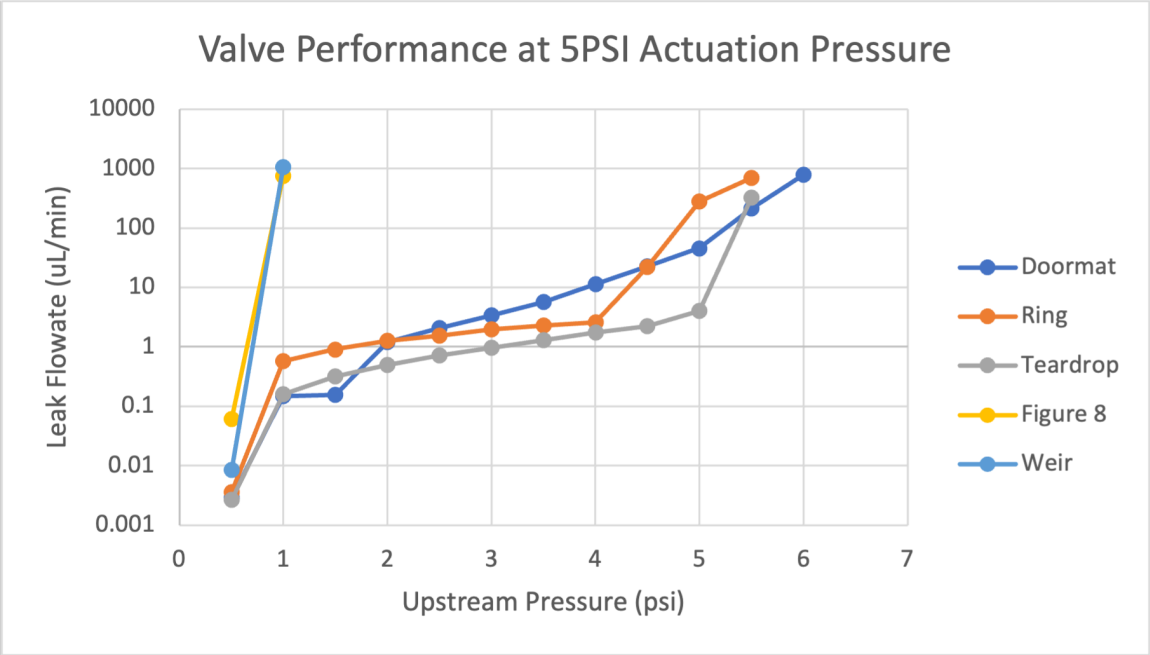

Figure 5-11: Leak flowrates of the 5 valve designs with an actuation pressure of 5 psi. Log-scale vertical axis.

The teardrop valve meets all of the requirements for a good valve design. It reliably seals up to the actuation pressure, generates a good seal at 5 psi, and is easy to machine. When compared to the doormat valve and ring valve, the teardrop valve also has significantly lower volume. The volumes of the three candidate valves can be compared in **Table 5.1**. For these reasons, the teardrop valve was selected

as the base valve geometry for all future platforms. It is worth noting that despite it's asymmetric design, the valve is actively controlled and it can be used for bi-directional flow. When configured with a pump chamber, the narrow edge of the valve is preferably oriented away from the pump chamber. This makes sure that the membrane can properly stretch over the valve seat and create a seal; when placed in the other direction the membrane cannot flex around the valve seat because it is pushing against an incompressible fluid in the pump chamber. A diagram of a complete pneumatic micropump is presented in **Figure 5-12**.

Valve	Chamber Volume (μL)
Doormat	0.320
Ring	0.503
Teardrop	0.188

Table 5.1: The chamber volume of three candidate valve designs.

The fluid can flow in either direction but is limited by the pneumatic control unit to 0-3 μL/s. Slow flowrates are possible, but are not recommended because the instantaneous flowrate of each pump stroke will greatly exceed the average flowrate. Lower flowrates may be acceptable when the instantaneous flowrate is less important than the average flowrate. These flowrates should be validated before being used experimentally. The flowrate of the pump at 30, 60, and 120 μL/min is shown in **Figure 5-13**. The measured average of these flowrates are 28.81, 58.07, and 110.21 μL/min. The slightly lower flowrates might be explained by the sensor saturation at 1,500 μL/min. Doubling the pump flowrate is accomplished by doubling the pump stroke frequency. An individual pump stroke is shown in **Figure 5-14** to highlight the flow induced by the pump chamber and valves.

The pump design was implemented as a CAD geometry template that can be dragged and dropped into any chip design. This makes designing new chips easy and fast. The final pump design has be observed to work at actuation pressures as low as $\pm$4 psi and with a variety of fluids such as DI Water, IPA, 200 proof ethanol, and even Pepto Bismol. The pump is self-wetting and clog resistant. Different pump

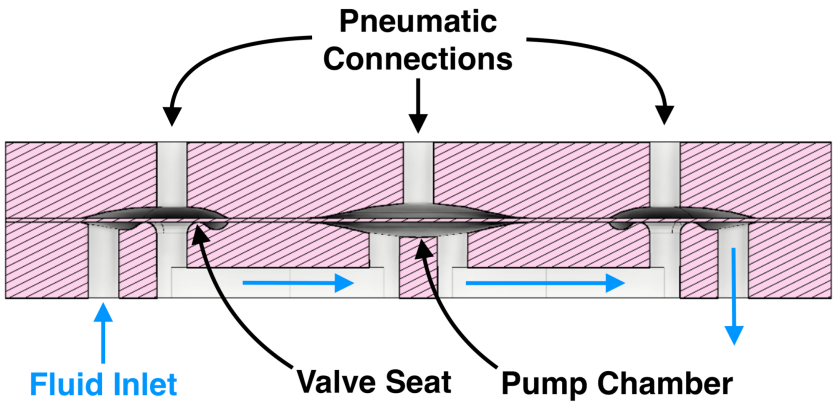

(a) Pump Cross Section

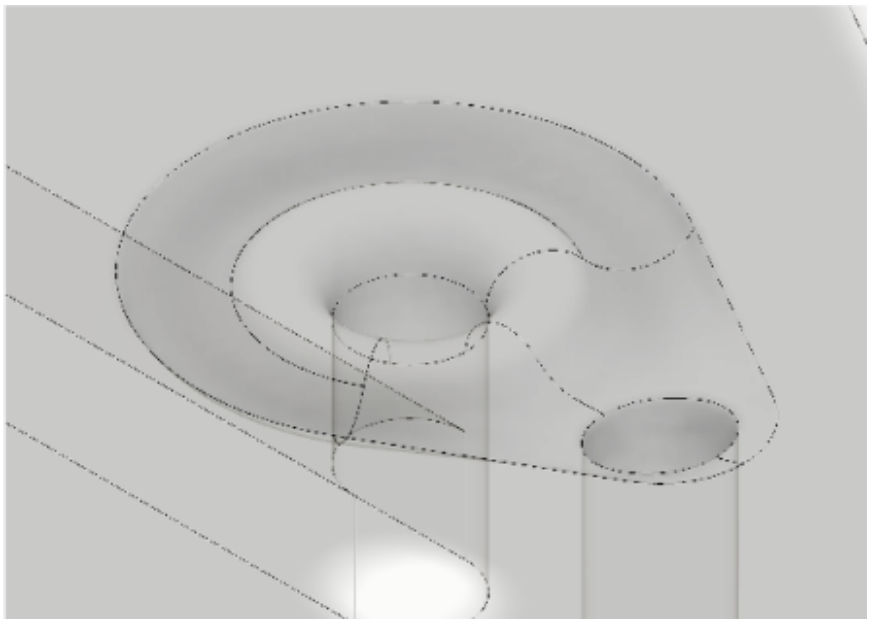

(b) Teardrop Valve Profile

Figure 5-12: A cross section of the redesigned COC micropump with a tangent arc pump chamber and two teardrop valves.

flowrates may be achieved by using larger or smaller diameter pump chambers and by implementing changes to the control scheme.

5.2 Fluidic Accumulators

The biggest issue with the existing pneumatic pump design is that it creates a pulsatile flow profile. This type of flow profile is undesirable, because some biological

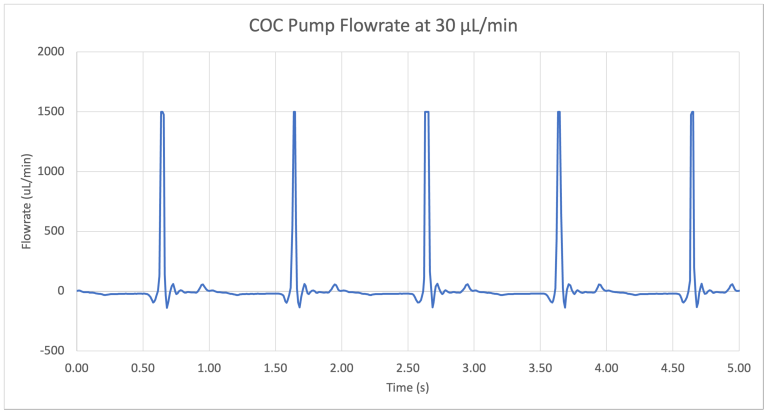

(a) COC pump flowrate at 30 μL/min.

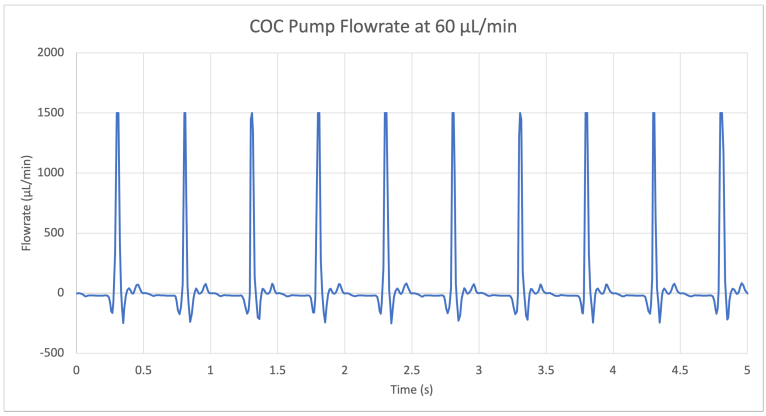

(b) COC pump flowrate at 60 μL/min.

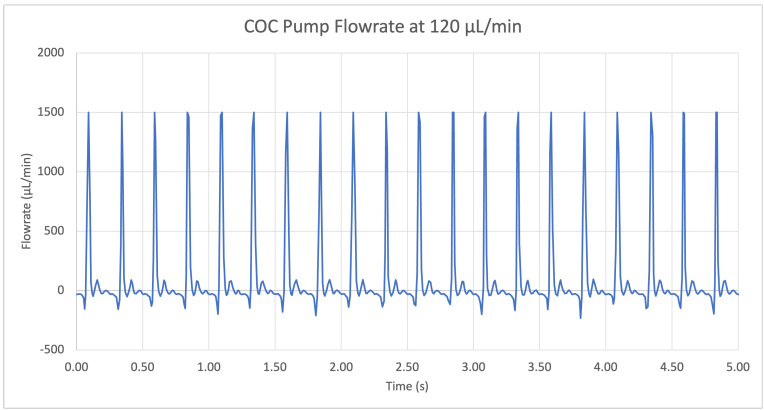

(c) COC pump flowrate at 120 μL/min.

Figure 5-13: The flowrate of the final COC micropump is measured using a Sensirion LPG10-1000 flowmeter connected to a chip via PTFE tubing. The measured average flowrates are 28.81, 58.07, and 110.21 μL/min when set to 30, 60, and 120 μL/min.

applications are sensitive to shear stress and thus to the stability of the fluid flow. To smooth out the fluid flow, an energy storage element is frequently used. In large-scale hydraulic circuits, this is accomplished by using a fluidic accumulator to store fluid

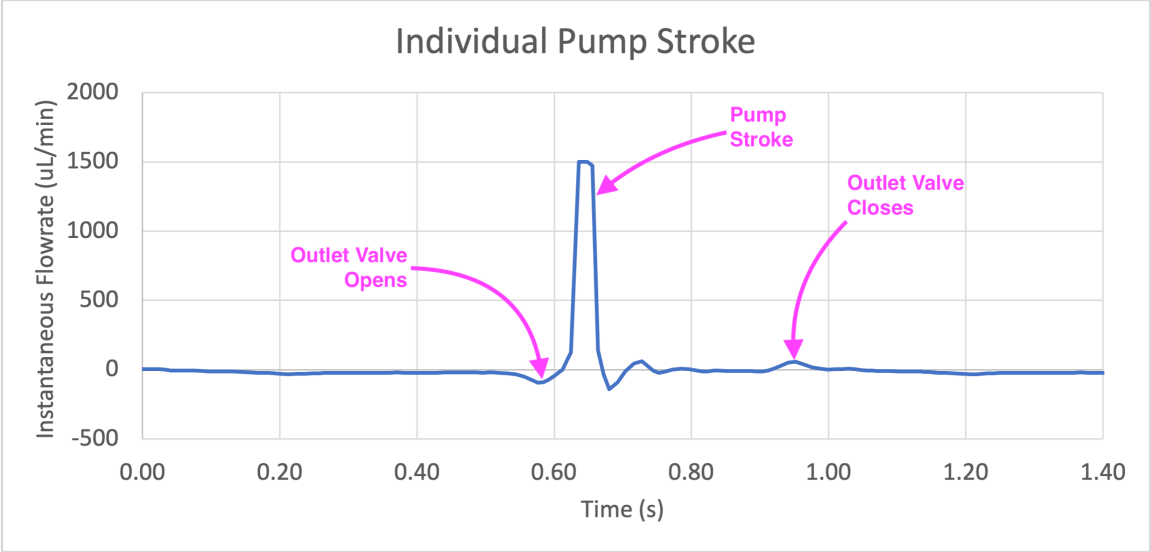

Figure 5-14: An individual stroke of the COC micropump. The valve openings and pump chamber displacement are highlighted in pink. The sensor saturates at 1,500 μL/min. Some oscillations in the flowrate at the end of the pump stroke may be caused by compliance in the system due to bubbles, tubes, and fittings.

under pressure. These components are usually a compressed piston or rubberized diaphragm that hold excess fluid volume at elevated pressure. In microfluidic applications, these elements are often called fluidic capacitors because their main purpose is to add compliance and damp out fluid pulsations. The term "capacitor" is appropriate for describing the energy storage potential of these devices and may be used interchangeably with the term "accumulator".

Very little work has gone into developing accumulators for microfluidic applications but they should be a standard element in many fluidic circuits. They are able to stabilize system flowrates, store fluid volume, protect the chip from overpressure events, and even potentially sense system pressures. Most microfluidic accumulators that have been studied use an elastomeric diaphragm that uses strain energy to hold fluid under pressure [63, 113, 89]. As the membrane is pressurized by the fluid it deforms and increases the system volume. A larger diameter increases the chamber volume and reduces the stiffness. If a large volume and high stiffness accumulator is required a higher modulus material or thicker membrane could be used. The main downside to this type of accumulator is that it requires an elastomer membrane,

which is not a feature of all microfluidic chips. Another proposed design uses capillary forces as a means for storing energy [90]. As fluid moves into a constricting channel the capillary force increases to store energy in the gas/liquid interface. This design is best suited for very small systems because the effect of capillary action only works at small scales.

An improved microfluidic accumulator should be able to store relatively large amounts of fluid under pressure and not require an elastomeric material to do so. This would allow the design to translate to all kinds of microfluidic devices, including 2-layer chips that are controlled using external pumps.

5.2.1 Trapped Gas Accumulator

One concept for a scalable and low-profile microfluidic accumulator is one that compresses trapped gas bubbles to store energy. The gas bubbles essentially act like springs in the device. One benefit to this concept is that the process of energy storage is linear and depends on the adiabatic expansion of the trapped gas. At constant temperature, the product of pressure and volume will remain constant between two states. This relation is expressed below:

$$P_1 V_1 = P_2 V_2 = C$$

The shape of the bubble determines the sensitivity of the accumulator; larger bubbles make the component more compliant and more bubbles add to the overall fluidic capacitance. One geometry for incorporating trapped bubbles into a chip is to have a series of dead-end channels that are configured into a tightly packed array. These finger-like channels are then connected to a fluidic channel so that there is a gas-liquid interface. As the pressure of the fluid increases, the gas will compress and some fluid will enter the fingers. The total volume of fluid that enters the fingers will be linearly proportional to the pressure of the fluid.

There are two main downsides to this design. First, some amount of pressure is required to get fluid into the accumulator in the first place. The fluid resists entering

the fingers because of surface tension forces. Once the surface tension is overcome, the accumulator becomes linear. The second issue is that any trapped gas in the accumulator may dissolve into the liquid. This would happen over several days, but may make this accumulator unsuitable for longer term studies. A photo of the first trapped gas accumulator prototype is shown in **Figure 5-15**. This accumulator has 12 mm long channels that are 300 μm wide and 150 μm in depth.

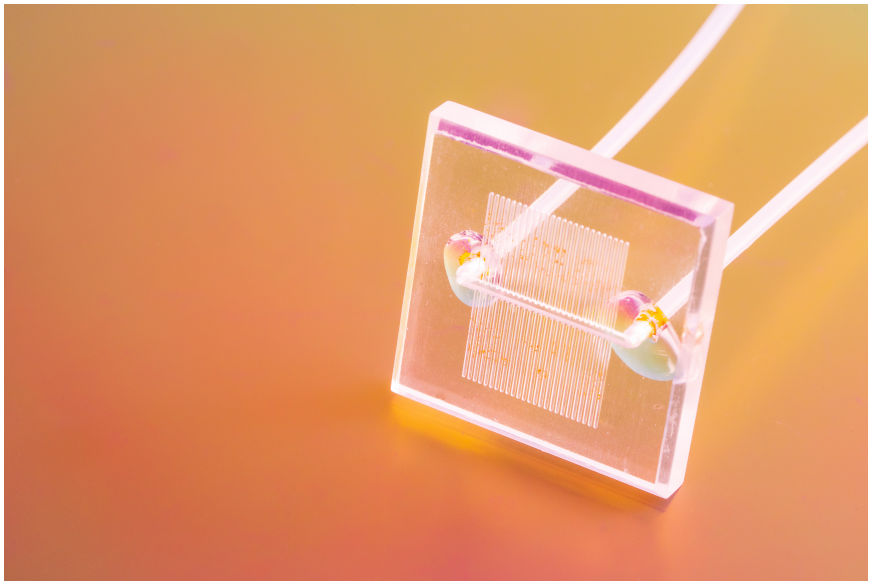

Figure 5-15: Prototype of a trapped gas accumulator.

The trapped gas accumulator was tested by connecting the device with PTFE tubing and wetting the channel with DI water and food coloring. The outlet was plugged and the inlet was connected to a syringe. The syringe was then used to compress the bubbles and a video recording of the accumulator was captured. Two frames from this video are presented in **Figure 5-16** to show the accumulator at low and high pressure states. The exact fluid pressure was not measured, but should equate to approximately 2 psi and 6 psi based on the length of the bubbles shown. The device could also be used as a pressure sensor because the length of the bubble is inversely proportional to the channel pressure.

Further testing of the trapped gas accumulator is suggested to better understand the effects of surface tension, size and shape of the fingers, and whether the trapped gas dissolves into the liquid over time. Further, the adiabatic model should be vali-

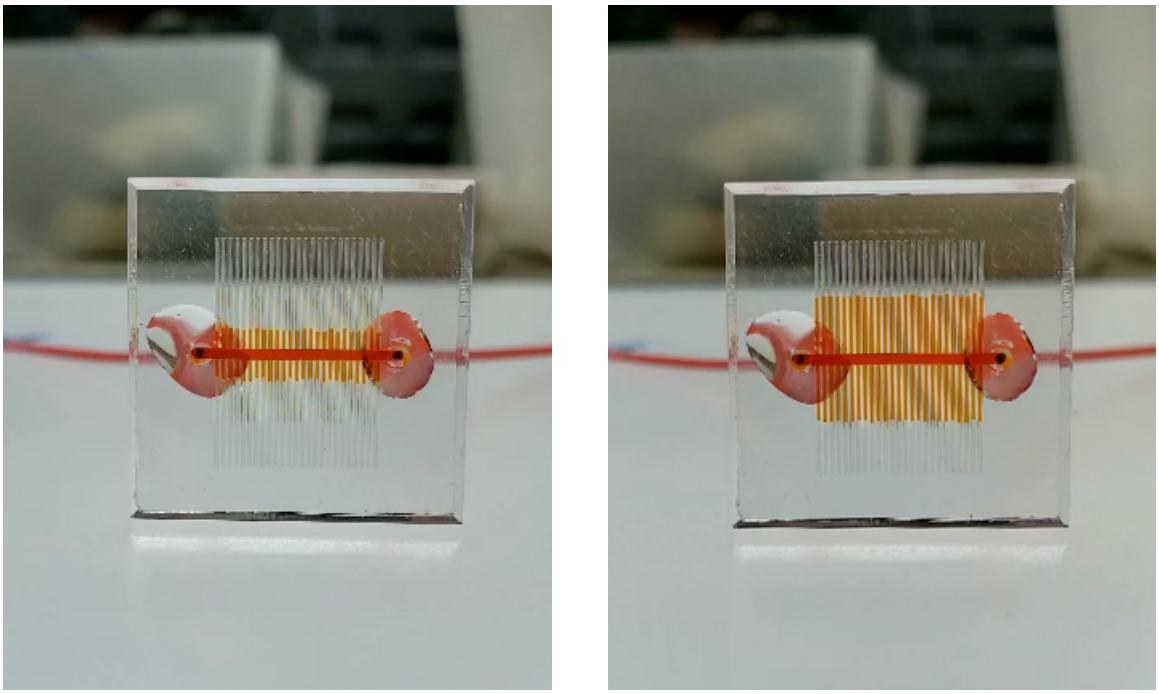

(a) Low Pressure (b) High Pressure

Figure 5-16: A trapped gas accumulator under high and low pressure conditions. The exact pressure was not measured but should be approximately 2 psi and 6 psi.

dated against the actual response of the accumulator.

5.3 Back-Pressure Regulator

The pneumatic pump is good at providing a consistent average flowrate, but does not set a defined pressure in the channel. Typically, the channel pressure is determined by the downstream fluid circuit when using a flow-determined pump. Similarly, systems that use a pressure-based pump design usually need to measure or model the flowrate generated by a given pressure. In most applications it would be desirable to control both the flowrate and pressure inside a given channel. Unfortunately, there has been little to no research on controlling the channel pressure in a microfluidic device when using a flow-determined pump.

One way to control the channel pressure in a system with a flow-determined pump is to use a pressure regulator. Three different types of pressure regulators for large scale hydraulic and pneumatic systems exist: a downstream-pressure regulator, a

back-pressure regulator, and a differential pressure regulator. A down-pressure regulator controls the pressure downstream of the regulating element, a back-pressure regulator controls the pressure upstream of the regulating element, and a differential pressure regulator controls the difference in pressure between two nodes of a fluidic circuit. Each have benefits and tradeoffs, but all kinds of regulators could be useful when implemented in a microfluidic chip.

The simplest type of pressure regulator for us to build is a back-pressure regulator. Typically, a back-pressure regulator consists of a diaphragm or valve-like element that can be biased to a set pressure. The fluid pressure pushes up against this element and begins to flow when the upstream pressure exceeds the setpoint of the back-pressure regulator. This configuration is useful for a microfluidic circuit because it enables a designer to control the pressure in a channel. Further, the lifting and closing of the regulating element can help to stabilize fluid flow. This is because the regulator is both a resistive and compliant element. The diaphragm flexes when the channel pressure increases above the applied pressure and the shearing of fluid through the regulator provides a resistance to flow. This behaves like an RC fluid circuit and helps to stabilize pulsatile flow. This is mechanism is explored further by combining the regulator with an accumulator in the sections below.

A back-pressure regulator was developed for microfluidic systems by using a 5 mm diaphragm and a similar internal geometry to the valves designed previously; a cross-section is provided in **Figure 5-17**. A 5 mm diaphragm was selected because it is has relatively low stiffness. Also, tension in the membrane has little influence on the sealing pressure because the geometry only allows a maximum of 4% strain in the membrane. A smaller diaphragm experiences more strain and would act as a mechanical amplifier; the sealing pressure would be significantly greater than the externally applied pressure. This is similar to the findings of the valve simulations presented in Section 5.1.1. With a 5 mm diaphragm, a pressure balance between the fluid pressure and applied external pressure dominates the mechanics and movement of the membrane. If the upstream fluid pressure exceeds the externally applied pressure, liquid will begin to flow. If the channel pressure is less than the external

regulator pressure, the on-chip regulator operates like a closed valve.

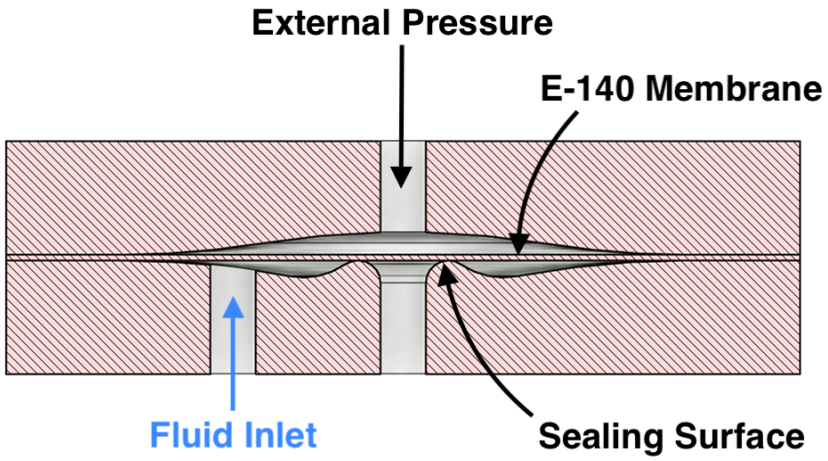

Figure 5-17: Cross-section of the back-pressure regulator.

Although there is some associated compliance with the back-pressure regulator, an accumulator helps to store energy and stabilize the system. A prototype of a back-pressure regulator and accumulator connected in series is presented in **Figure 5-18**. Fluid first flows into the accumulator and then pushes up against the back-pressure regulator. A later version of the chip was modified to have an additional port for monitoring the channel pressure between the on-chip regulator and trapped gas accumulator. This additional port can be seen in **Figure 5-18b**. The size of the accumulator was also increased from the size of the original chip.

The back-pressure regulator and accumulator were then configured in a test setup to see how well the pressure regulator would work when driven by a pneumatic pump. A vented reservoir was connected via PTFE tubing to an external pneumatic pump between two Sensirion LPG10-1000 flow sensors. This configuration allows for monitoring the flowrate on the suction side of the pump as well as the pressure regulated discharge side. Next, the tubing is connected to the accumulator and back-pressure regulator. The outlet of the pressure regulator is connected to another vented reservoir. The back-pressure regulator is controlled using a conventional 0-10 psi pneumatic pressure regulator, and the on-chip liquid pressure is monitored using a 0-10 psi

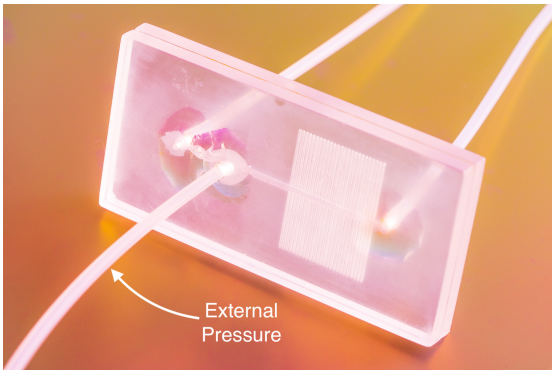

(a) Original prototype of an on-chip pressure regulator.

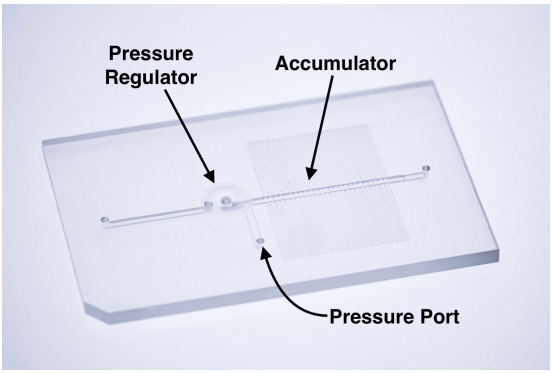

(b) Additional port added for measuring fluid pressure.

Figure 5-18: Prototype of a microfluidic back pressure regulator with an integrated trapped gas accumulator.

Elveflow pressure sensor. The external pneumatic pressure was also measured using a 0-10 psi Elveflow pressure sensor. This pressure sensor was wetted with fluid and then capped on the outlet; this makes sure that there is no added compliance due to bubbles in the pressure sensor or tubing. A diagram of this test setup is provided in **Figure 5-19**.

The pump was set to flow at 120 μL/min and the pressure on the pneumatic regulator was varied from 0-4 psi. The measured input pressure and corresponding channel pressure are presented in **Figure 5-20**. The pressure regulator behaves linearly, and the channel pressure is almost identical to the applied pressure. The test had to start at 0.25 psi because the 0-10 psi pressure regulator does not open until this pressure. Another test with a different external pressure regulator would be required to validate the back-pressure regulator performance at lower pressures. The error is also reported in **Figure 5-20b** as the difference in applied pressure and channel pressure. The channel pressure will always be greater that the externally applied pressure regulator due to viscous forces in the chip, tension in the membrane, and sealing characteristics of the back-pressure regulator. In general, the pressure regulator will only need to be operated between 0-2 psi and and is assumed to be accurate within approximately 0.05 psi in that range.

At higher pressures, the regulator begins to reduce the pump flowrate and behaves

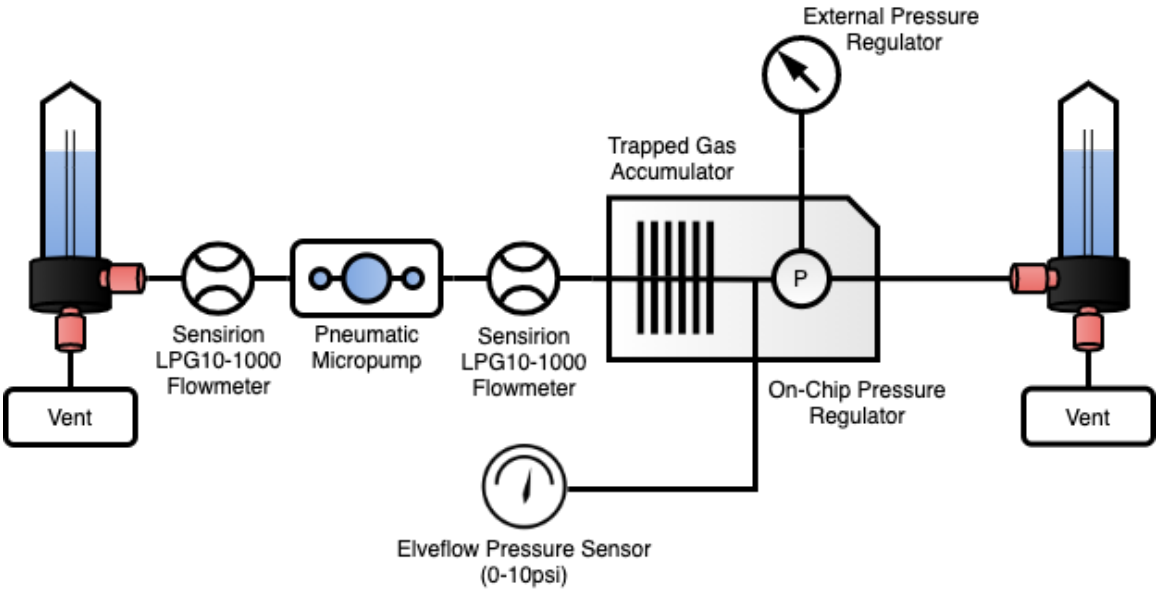

Figure 5-19: Test setup for evaluating the on-chip pressure regulator and trapped gas accumulator. The setup features a flow sensor at the inlet and outlet of the pump, pressure sensors for monitoring the externally applied pressure and channel pressure, and two vented reservoirs.

less predictably. The added pressure resistance from the regulator decreases the pump flowrate as shown in **Figure 5-21**. Note that this data was generated using the original micropump design and that the new pump design can overcome significantly greater head pressures. It is possible that the improved pump provides more stable flow and may be able to drive the back pressure regulator at higher pressures but this has not been tested.

At higher pressures the external regulator and on-chip pressure regulator become less stable. The pulsations of the pump start to appear in the pressure profile and the on-chip pressure is no longer uniform. The on-chip pressure and externally applied pressures can be compared in **Figure 5-22a** and the error between on-chip pressure and external pressure is presented in **Figure 5-22b**. There are a variety of factors that could contribute to this pressure variation. First, the on-chip regulator is not really designed to work at higher pressures; at these pressures the diaphragm closes entirely and behaves more like a valve than a regulator. Second, it appears that the external regulator is not providing a constant pressure. Ideally, the external regulator should remain at a fixed pressure and not get influenced by the micropump or on-chip

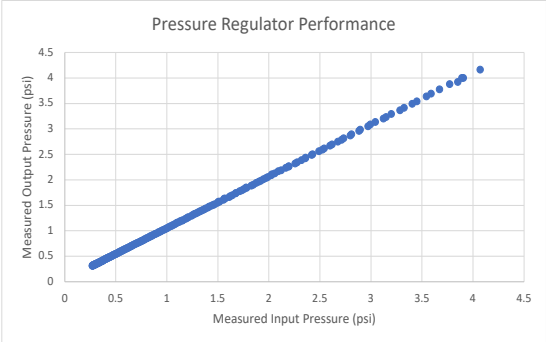

(a) The regulated channel pressure is almost identical to the externally applied pressure, especially at low pressures.

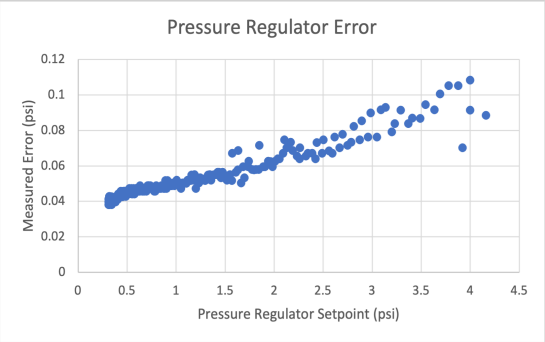

(b) The absolute error is the measured difference in applied pressure and channel pressure.

Figure 5-20: The the pressure regulator behaves linearly despite irregularities in the system flowrate. The error of the regulator depends on the applied pressure and the system is more stable at lower pressures.

pressure regulator. It is possible that this pressure variation is due to the external pressure regulator being coupled to the same air line as the pneumatic pump. More testing with a better external pressure regulator connected to an independent line is recommended.

To get a better sense of the pressure regulator stability, the external regulator was set to 6psi and manually adjusted to relieve the pressure for 6psi down to 0 psi. The pump was set to drive a flowrate of 120 μL/min. As the pressure was decreased the regulator first behaves erratically and then stabilizes as observed in **Figure 5-23**. At about 4 psi the regulator becomes stable and is much easier to control. The system works best between 0-2 psi and should not be used outside this range until the pressure variation is studied further. It is likely that the pneumatic pressure regulator's feedback system is not stable at the high frequency switching of the pump platform. This is not uncommon for gas pressure regulators [87].

Another benefit to the pressure regulator and accumulator combination is that they help to damp out fluid pulsations. The flowrates on the suction side of the pump and pressure regulated discharge side of the pump are shown in **Figure 5-24**. The regulator and accumulator act like an RC circuit and smooth out the flow profile from the pump. This effect was measured right at the discharge of the pump

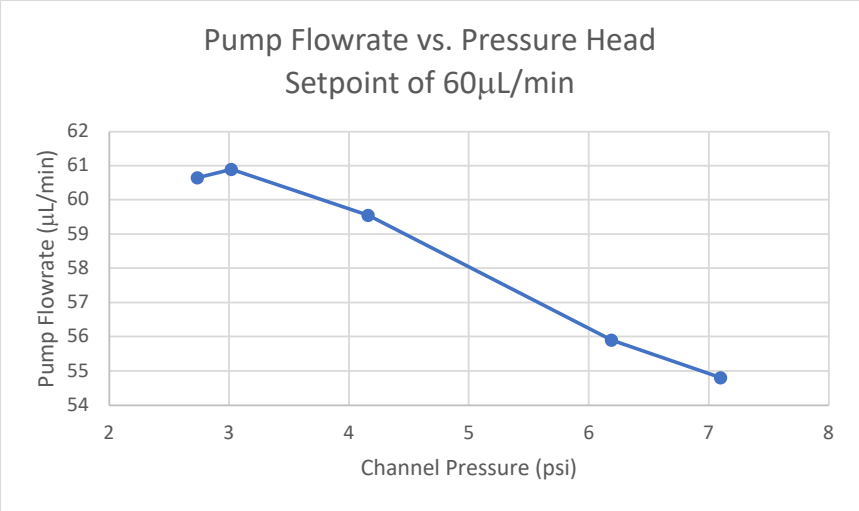

Figure 5-21: At pressures above 3psi flowrate starts to decrease. The pump is unable to overcome the added resistance of the regulator and the flow begins to slow down.

but would be more stable if measured between the capacitor and accumulator. This pressure regulating system sets a precedent for being able to provide stable fluid flow using a displacement-based pump and still be able to control the channel pressure. The back-pressure regulator alone helps to improve flow stability, but the addition of an accumulator provides the best results.

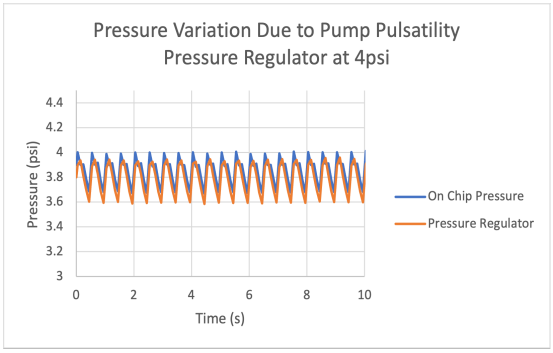

(a) The external regulator and on-chip regulator begin to fluctuate with the pulsations from the pump at higher pressures.

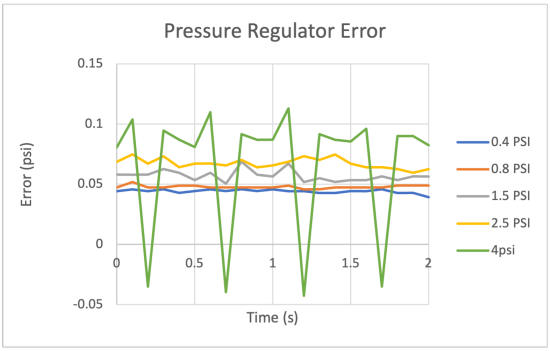

(b) The pressure regulator is more stable and predictable up to pressures of approximately 2 psi.

Figure 5-22: The pressure regulator does not provide a uniform pressure when set at a higher pressure. This may be attributed to the faster opening and closing of the on-chip diaphragm as well as coupling of the pressure system used to to drive the pump and external pressure regulator.

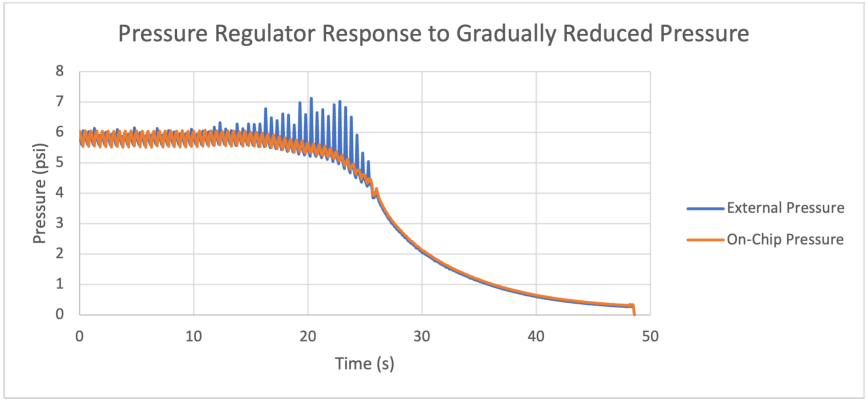

Figure 5-23: The external regulator was gradually adjusted to see the pressure regulator response over a wide pressure range. At 4 psi the regulator stabilizes and becomes much easier to control. At about 0.25 psi the external regulator shuts off.

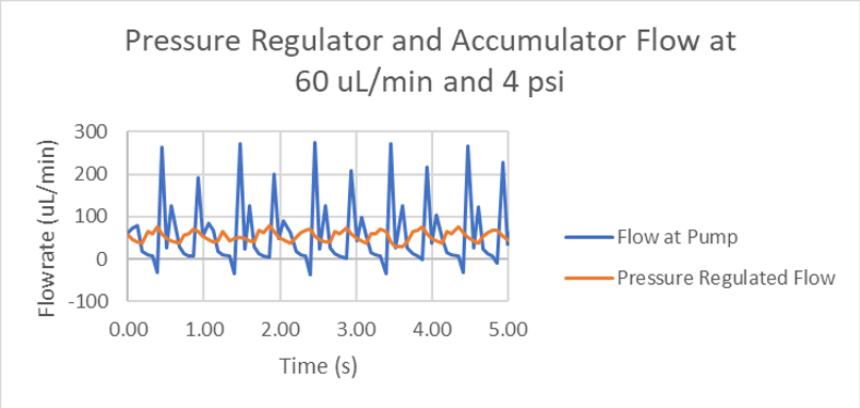

Figure 5-24: Improved micropump flow stability with the use of a microfluidic back-pressure regulator and an integrated trapped gas accumulator.

Chapter 6

Tissue Integration

Integrating tissues into a microfluidic device is one of the biggest challenges in 3D cell culture experiments. For a tissue to properly integrate into a microfluidic device it needs to have some sort of Extracellular Matrix (ECM). An ECM *in vivo* may consist of a scaffold composed of collagen, elastin, bone, other connective tissues, or even liquids such as blood plasma. The ECM provides a space for cells to migrate, divide, and proliferate. It can influence cell-adhesion characteristics and even change cell phenotypes. Variations in the stiffness and composition of the matrix can have a large influence on cell behavior and viability. Every organ has an ECM with defining characteristics that help to structure the tissue [114]. Within an ECM there are numerous growth factors, integrins, enzymes, proteins, and other biomolecules that help the tissue to function.

These same principles hold true for *in vitro* systems. Cells in 2D or 3D cultures require a matrix to grow and proliferate. This can be as simple as a petri dish with agar, a plastic scaffold or membrane, or as complicated as Matrigel, a gelatinous emulsion of proteins and growth factors secreted from malignant mouse tumors. These materials may be combined with other matrix materials such as collagen, or can be used stand alone. Similar to the ECM's found *in vivo*, a matrix for a cell culture experiment should be tailored to a specific tissue.

One of the most common methods to mimic the ECM found *in vivo* is to synthesize a hydrogel biomaterial that replicates the mechanical structure and chemical

profile of the matrix found in the model organ. A hydrogel is a biocompatible (and usually biodegradable) material with relatively high water content and mechanical properties that closely match living tissues. Such gels can be composed of a material such as fibrin, PEG, or a variety of other polymeric materials. The stiffness of the material can be tuned using varying amounts of crosslinking agents, and the cell-adhesion characteristics can be controlled by incorporating different receptors and growth factors. For example, a hydrogel scaffold has been developed to closely match the shape, structure, and biochemical profile of the human intestinal epithelium [115].

Most hydrogels are installed into an open-well device such as a 96-well plate or injected into a microfluidic chip. Hydrogels are usually installed as a liquid and then polymerize once incorporated into the device [116] . The most common method for integrating a hydrogel into a tissue chip is via a surface-tension based technology called a phase guide. A phase guide is a geometric feature in a chip that pins the meniscus of a hydrogel material during installation and helps to shape the hydrogel into a constrained geometry [117]. Phase guides have become the most common means for integrating hydrogels into a chip because they are simple and easy to use. Other types of capillary pinning techniques have been explored and may be used depending on the specific application's requirements. For example, a platform may require arrays of hydrogels rather than a single channel [118]. A wide range of hydrogels and installation methods are now available for researchers to design and fabricate a system to suit their experimental needs [119].

Despite the widespread adoption of hydrogels in the cell culture field, there are a number of challenges associated with using phase guides in a microfluidic chip. Phase guides are sensitive to the wetting properties of the material, the height of the channel, the shape of the phase guide feature, the bulk polymer material, and the properties of the hydrogel, as well as any surface treatments applied to the chip. If these factors are not properly accounted for, hydrogels can spill over or burst into neighboring channels during installation. Further, the shape of a phase guide may cause the hydrogel to bulge into an undesirable shape when it swells. Lastly, the phase guide structure is only useful when the hydrogel is installed into the device.

Once the hydrogel has polymerized, the phase guide is a vestigial structure that blocks convective and diffusive transport through the hydrogel and essentially results in wasted biomaterial. This part of the chip is sometimes called a "dead zone" to describe the lack of cell proliferation and viability found in these areas.

Some research has gone into designing pressure regulators for controlling the installation process, but this technique wastes a significant amount of material and demands a specific shape of hydrogel compartment [120]. Others have tried to create sacrificial templates that dissolve to create internal geometries in the hydrogel that act as fluidic channels or the foundation of a vascular bed [121, 122]. Channels with cell-laded gels can even be 3D printed into precise geometries [123].

6.1 Concept Selection for Hydrogel Installation

In this thesis we explored alternative methods for installing hydrogels into a device, so that a wider range of geometries can be designed into a chip. These approaches are alternatives to phase guides, which limit the amount of material that can be used and are not reliable enough for larger scale experiments. An ideal hydrogel installation method should have the following features:

1. **Accommodates All Hydrogels**

   The device should allow for any kind of hydrogel material to be installed. It should avoid any dependance on the density, viscosity, or wetability of the hydrogel. The design should also be able to be scaled to different volumes and aspect ratios and reconfigured for a specific tissue. This would allow for chips to be designed with no built-in constraint on tissue size.

2. **Easy to Use**

   The installation method should be easy to use and reliable. A user should not have to worry about the hydrogel bursting into another channel or have to control the pressure of the gel during installation. The hydrogel should also be able to be installed via pipette so as to use a familiar tool for the operator. This

process should be fast and intuitive so that the gel does not polymerize before it is installed into the chip.

3. **Allows for Direct Tissue Access**

   The compartment should allow for sampling of the tissue and enable a biologist to directly probe, add cells, or otherwise interact with the tissue. Media should be able to be sampled directly at the tissue and the tissue should be able to be removed from the chip after an experiment.

4. **Imaging Friendly Design**

   The compartment must be imaging friendly for use with a microscope and thus allow for cells to be imaged without other structures or materials getting in the way of the image.

5. **No "Dead Zone"**

   The geometry should be free of any "dead zones" or areas where the hydrogel goes to waste. All parts of the hydrogel should be able to receive nutrients by both diffusive and convective transport.

The tissue compartment might be in a variety of different sizes and shapes depending on the experimental requirements and type of tissue. Cross sections of different hydrogel geometries and tissue compartment features are presented in **Figure 6-1**. Variations in the tissue compartment will influence factors such as how media is perfused into the tissue, where cells are loaded into the device, how media can be sampled in the device, how the gel is allowed to swell, and what is able to be imaged.

For this project, a perfusable hydrogel tissue compartment with two fluidic channels on opposing faces at different pressures is the ideal configuration. This will allow for media to be perfused through the gel and for cells to connect to the lumen-like structure of the media channels. This type of geometry could be produced in a variety of different ways as discussed in the sections below.

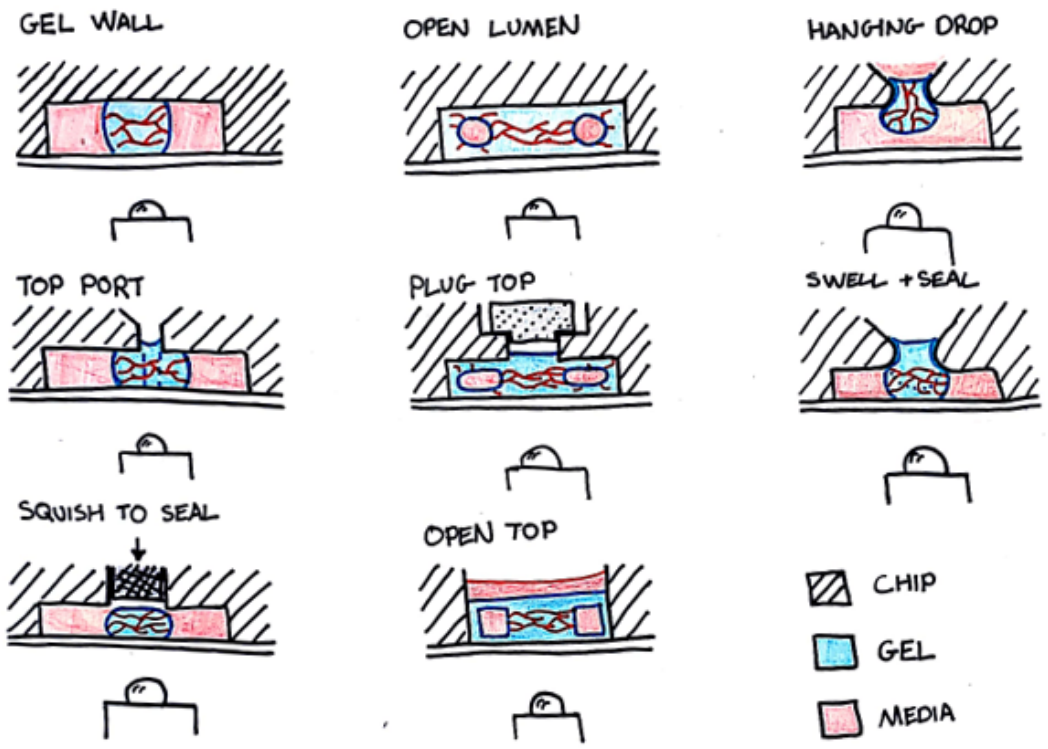

Figure 6-1: Different configurations for a vascularized hydrogel tissue compartment. All of these configurations feature two or more media channels that can be used to perfuse a central hydrogel channel. Here the gel is shown in blue, and the media is shown in red.

6.1.1 Laser Cut Micro-Porous Membranes

The hydrogel could be installed on top of a micro-porous membrane. If the membrane is made of a hydrophobic material, the liquid gel will remain on top of the membrane due to surface tension. This could work with tightly spaced pores as big as 1mm in diameter. The E-140 membrane could even be used as a material since it is image friendly, able to be laser cut, and hydrophobic. A CAD model of this type of scaffold is shown in **Figure 6-2** and a laser cut membrane prototype is shown in **Figure 6-3**.

6.1.2 Dissolvable Materials

An open channel in the device could also be made using dissolvable materials. One method would be to use dissolvable structures that are pre-installed or 3D printed into to device. The hydrogel would be cast over the dissolvable structures and the resulting

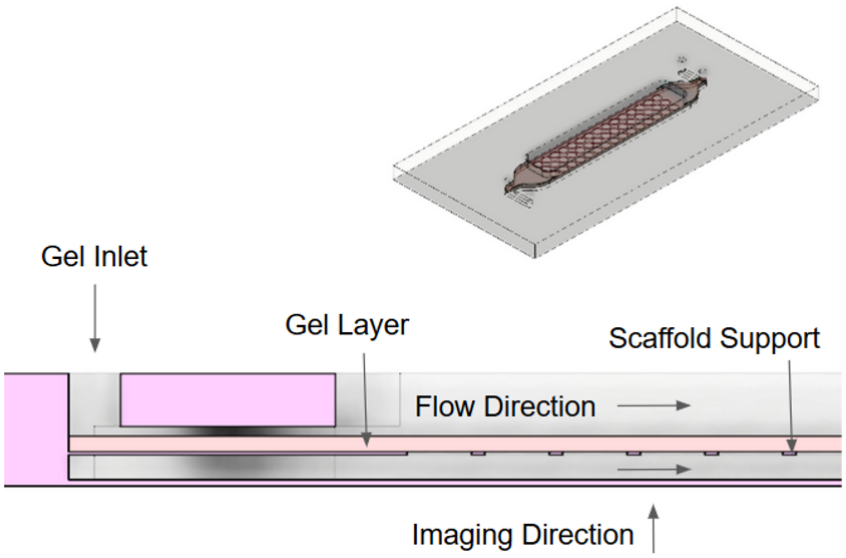

Figure 6-2: Concept for a hydrogel scaffold made using a laser cut membrane bonded in the middle of a chip.

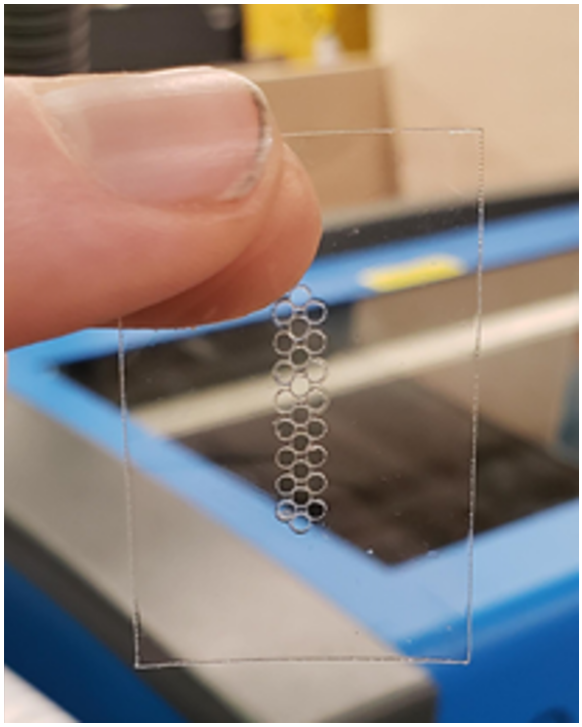

Figure 6-3: Prototype of a laser cut cell scaffold with 1 mm diameter holes. This scaffold was shown to support several microliters of DI water.

cavity would be used as an open lumen for media to pass through. Alternatively, the gel could be installed into a dissolvable packet similar to the dissolvable pods used

to load dishwashing detergent. The gel would be injected into the dissolvable packet, polymerized, and then loaded into the chip. The media channels would then be used to dissolve the packet. Alternatively, the gel could be installed into a chip with a dissolvable scaffold or membrane. This would create a smooth interface between the gel and media channels and potentially limit the amount of dissolved material. Finally, micropillars or phase guides could be made of a dissolvable material. This would allow them to shape the hydrogel during installation and then get removed after their intended use.

Many dissolvable materials could be used to design these structures. For example, the structures might be made of salts or other crystalline materials. The features could be made of glucose so that they can be dissolved into the media and later digested by the cells. Other polysaccharides might be considered, including pullulan, which can be extruded as a thin film (Ex. Listerine breath strips). Proteins may also be used since many can be broken down enzymatically. The right material will depend on the biological sensitivity and solubility of the material.

6.1.3 Hanging Hydrogel Drops

Another surface pinning technology comes in the form of a hanging drop. Hanging drops have been used to develop a wide variety of plate-based assays, and could serve a similar function in hydrogel-based experiments. Typically, a hanging drop device uses a liquid media in a drop form to aggregate cells and components in the media into the bottom of the drop. This technique has frequently been used to grow spheroids, a type of spherical organoid.

For implementation in this type of microfluidic device, the hydrogel drop would need to form under a slot-shaped feature in the chip to create an elongated drop. This feature would enable more gel volume to be used than possible in a semi-spherical drop. The benefit to this feature is that the hanging drop would allow for the gel to swell after polymerization and grow into a near rectangular geometry. The swelling of the gel could then be used to create a seal between two media channels. A sketch of this concept is found in **Figure 6-4**.

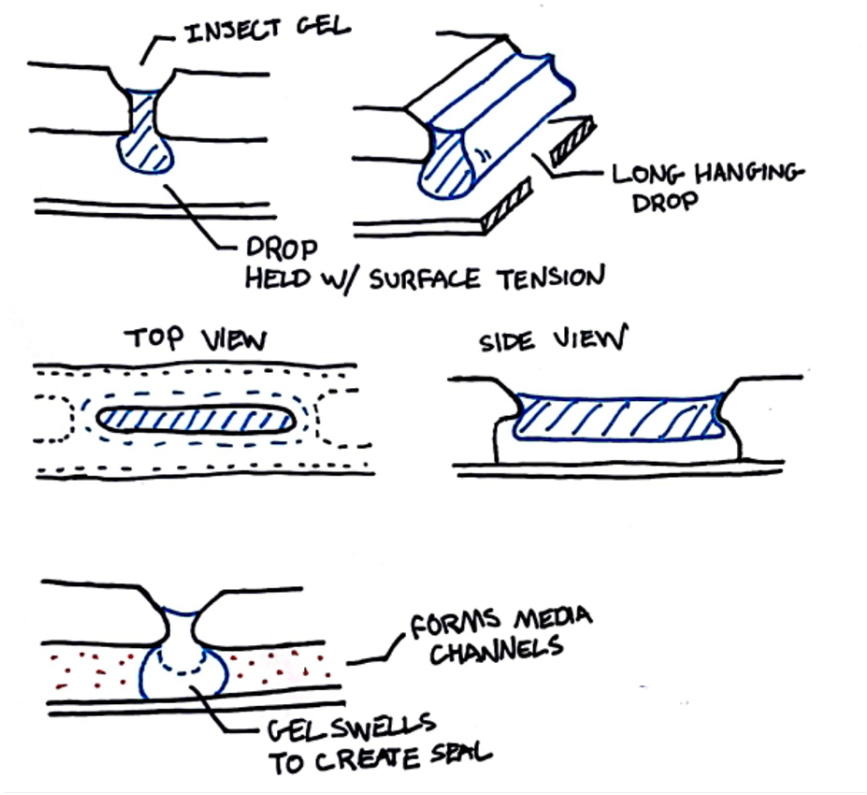

Figure 6-4: Concept for a hydrogel tissue compartment with a slot-shaped hydrogel drop constrained by surface tension.

6.1.4 On-Chip Transwell Insert

Similar to a membrane-based tissue compartment, a gel might be loaded directly onto a transwell insert on a chip. This insert could occupy the same space as the media reservoir. Media could be drawn from the top of the reservoir and the fluid outlet could be placed under the scaffold. This geometry would require new inserts to be made of an image friendly material and joined to the chip. Significant effort would be required to make sure that the reservoir and scaffold can be imaged properly.

6.1.5 Removable Components

The hydrogel geometry could also be made using removable structures. These structures cannot be allowed to bind to the gel, so it would be recommended that PTFE, PFA, or some other non-adherent polymer would be used. A few concepts that leverage this technique are presented in **Figure 6-5**, **Figure 6-6**, and **Figure 6-7**. This

concept was further refined into the final tissue compartment presented in Section 6.2

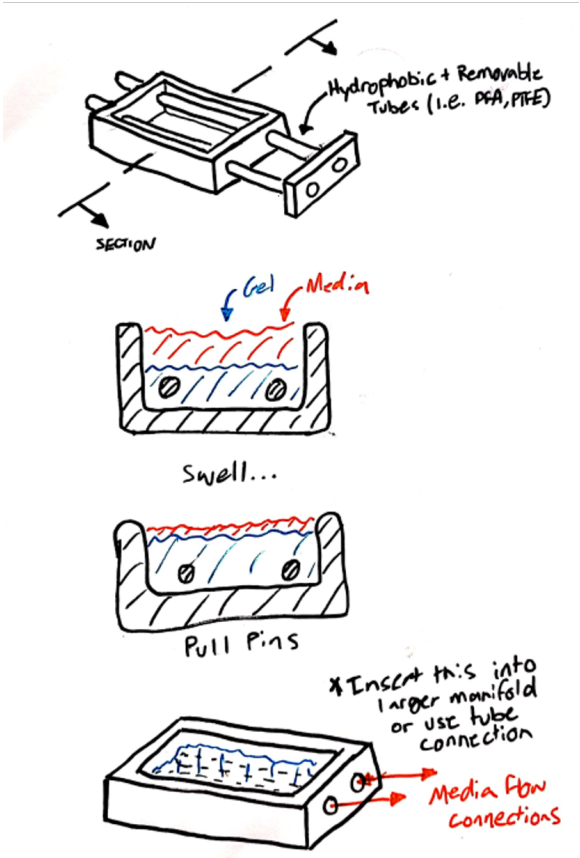

Figure 6-5: Concept for a hydrogel compartment with open-lumen structures formed with removable PFTE pins.

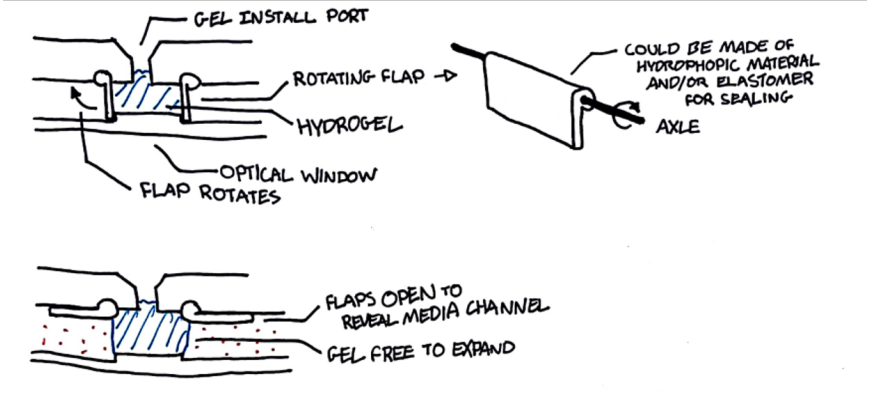

Figure 6-6: Concept for a hydrogel compartment with a gel wall that is created using a rotating flap made of a non-adherent material.

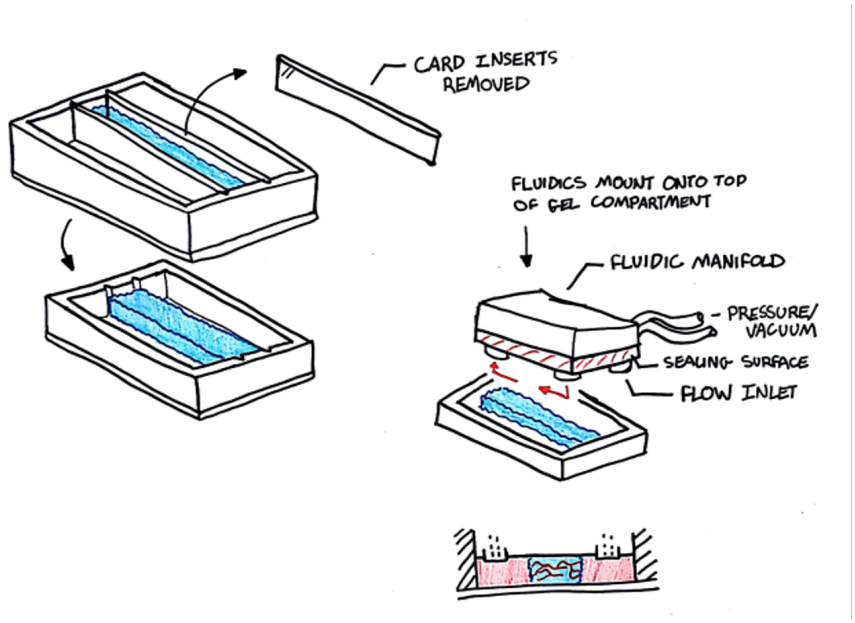

Figure 6-7: Gel geometry defined with removable PTFE walls.

6.2 PTFE Gel Guide Tissue Compartment

The concept for using removable structures was selected as the best method for containing a hydrogel in our microfluidic device. This method is preferable because it can be designed to generate a flat gel-media interface. This is desirable because the gel media interface is a key factor in creating vascular structures that are fully perfusable.

An early experiment was conducted to see what materials would stick to a PEG-based hydrogel. PEG drops were placed onto sheets of HDPE, PMMA, Ultem, COC, and PTFE. All of the drops adhered except for those on the PFTE substrate. This was the expected result, and PTFE was confirmed as the material choice for the removable structures.

Next, a prototype was made to show that fluids including gels could be constrained by PTFE walls that would then slide away into the chip or be removed from the top of the chip. In **Figure 6-8** a 12 mm long and 1 mm wide channel is blocked by PTFE walls on either side and filled with DI water. The PTFE walls do not allow the water to spill into the neighboring channels because the liquid is pinned at the corners using surface tension. This demonstrates that a liquid can be formed into a rectangular prism using PTFE walls.

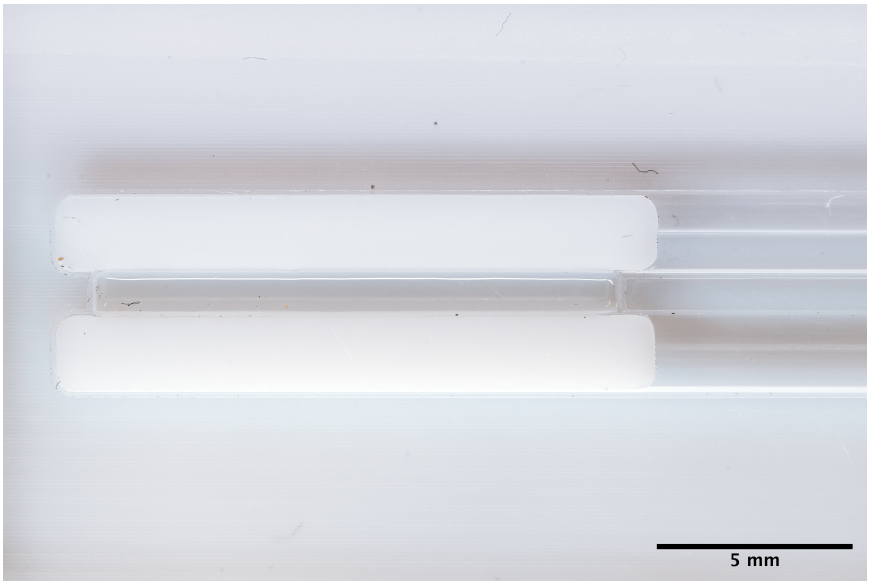

Figure 6-8: Gel geometry defined with removable PTFE walls.

The prototype was further refined to use PTFE plugs that protrude from the top of the chip. The plugs are slot-shaped components that define a rectangular compartment inside of the chip. Gel is installed into the compartment via a 0.8 mm diameter hole in the top of the chip. The gel is allowed to polymerize before the PTFE plugs, hereafter called gel guides, are removed; this polymerization process requires about 20 minutes at 37°C in the incubator. The gel guides are disposable and removed using a pair of specialty tweezers as shown in **Figure 6-9**. Loading of a PEG-based hydrogel into a chip with an integrated tissue compartment is also shown in **Figure 6-10**

(a) Specialty tweezers. (b) Grab PTFE gel guide. (c) Pull to remove.

Figure 6-9: Removal of PTFE gel guides after hydrogel polymerization.

Once the gel guides are removed, the compartment is sealed by inserting a small cap made of an elastomeric material. The original prototype caps are made using

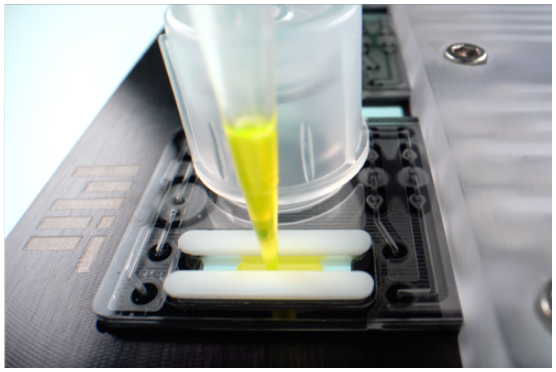

(a) PEG-based gel installed using a pipette. The liquid gel fills the compartment from the center to the edges.

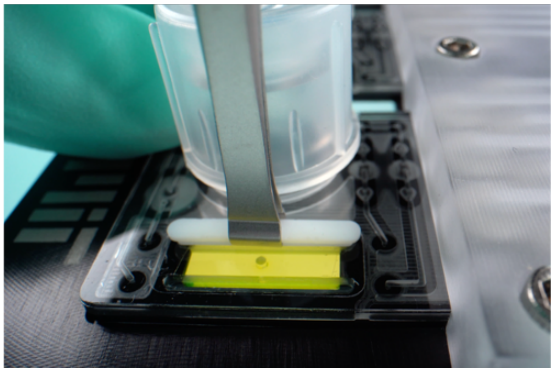

(b) Gel guides are removed once the gel has polymerized. The gel guides are disposed of and treated as biohazardous waste.

Figure 6-10: A fluorescent dyed PEG-based gel getting installed into the tissue compartment using a $200\mu L$ pipette tip.

PDMS, but a final part should be made using TOPAS E-140 to give better inertness properties. A photo of the cap installed into a prototype chip is shown in **Figure 6-11**, and a close-up photo of the cap's sealing feature is shown in **Figure 6-12**. The cap seals the tissue compartment by means of a small bump that presses against the walls of the slot-shaped hole in the chip. This cap geometry works well when placed properly, but can leak if the cap is misaligned to the slots. One problem is that PDMS is too soft for the cap to properly orient with the slots when it gets pressed in place. PDMS was used for prototyping purposes because the required mold could be readliy machined using an undercut ball endmill and because we can cast PDMS in our lab at room temperature.

The cap has an added benefit in that it can be removed to sample media next to the tissue or to add other components to the gel. Future designs should further take sterility into consideration and improve upon the sealing characteristics of the bump. Additionally, ports in the top of the tissue compartment might allow for other cells to be added into the compartment or for media to be added directly to the gel.

The gel guides create a molded hydrogel structure that is in the shape of a 1x3x12mm rectangular prism. The gel walls are flat and smooth to create the best surface for vascular networks to open up to the media channels. More surface area also implies that no region will be cut off from nutrient supply.

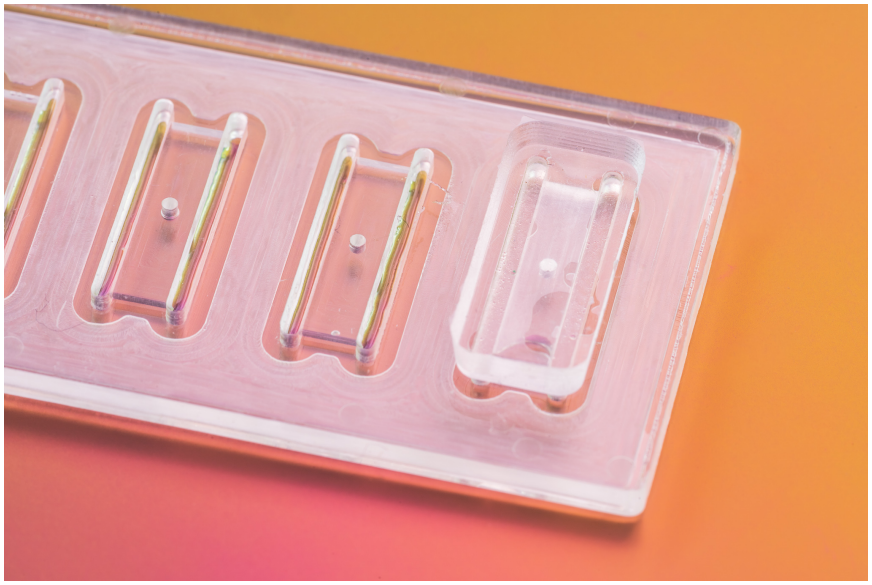

Figure 6-11: The compartment is sealed using an elastomeric cap. A cap prototype was made using PDMS but the part is designed to be made of TOPAS E-140.

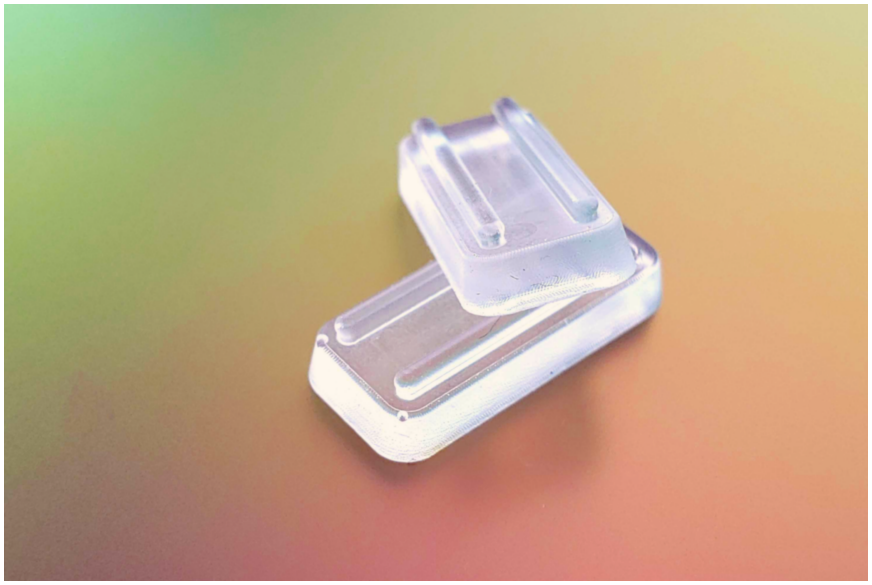

Figure 6-12: The caps have two slot-shaped plugs with a small bump on the lower outer periphery that helps to create a defined seal.

The gel compartment has an added benefit in that it does not allow gels to swell inside the chip. PEG based gels were installed into a chip with this tissue compartment and left to swell in PBS media. As seen in **Figure 6-13**, the gel did not expand significantly into the media channels after several hours of exposure to the PBS. Later devices loaded with PEG gels exhibited similar good behavior. Although

it is beneficial that the gels do not swell and block the media channels, it may prevent them from reaching their intended final volume. Future iterations of this tissue compartment design could consider using an elastomeric diaphragm behind the gel so that the hydrogel has a degree of freedom to expand into. The current geometry constrains the top and bottom of the gel and prevents the material from expanding isotropically.

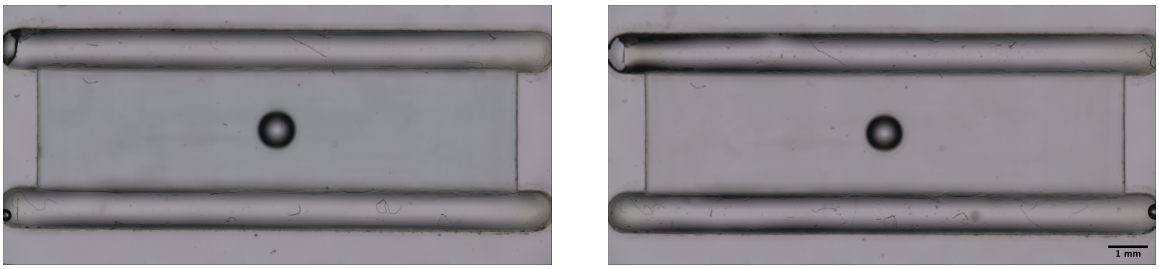

(a) PEG-based gel after installation. (b) Gel allowed to swell in PBS for 1 hour.

Figure 6-13: The PEG-based gel does not swell in this tissue compartment design.

This hydrogel tissue compartment is very easy to use and allows for a wide range of hydrogel materials to be used. As long as a gel can be installed as a liquid via pipette, it should work with this device. The compartment allows for imaging of the tissue and access to the media channels. The size of the compartment can be easily adjusted by using different PTFE gel guides and longer slot-shaped media channels. This system is further evaluated in a biological study presented in Chapter 7.

Chapter 7

Biological Validation

The proposed Organ-on-a-Chip platform was evaluated using two chip designs that help to validate the biological performance of the new platform. First, the adsorption and absorption of progesterone is compared to a PDMS device. Second, a chip is used to vascularize a co-culture of Human Umbilical Vein Endothelial Cells (HUVEC) and Normal Human Lung Fibroblast (NHLF) cells in fibrin and PEG-based hydrogels. The design of the two chips is described in the sections below and the results of the experiments are presented in detail.

7.1 Media Recirculation Chip

The first chip design includes a 400 μL reservoir, a pneumatic micropump, and a back pressure regulator. A top-down view of this chip with blue dyed fluid showing the channels and other components is provided in **Figure 7-1**. The single-inlet, single-outlet design enables a user to recirculate media at a flowrate between 0-3 μL/s at elevated pressure of up to 2 psi. This fluid loop can be used to evaluate the absorption characteristics of the COC materials to specific molecules and may later serve as a platform for comparing different surface treatments for improved chemical inertness. The chip may also be used to evaluate the viability of monocytes and T-cells that are passed through the pumps, for the purposes of studying immune cell recruitment and extravasation in various physiological and pathological conditions.

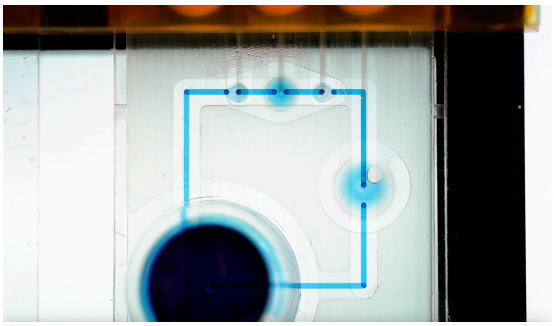

(a) A top-down view of the Media Recirculation Chip.

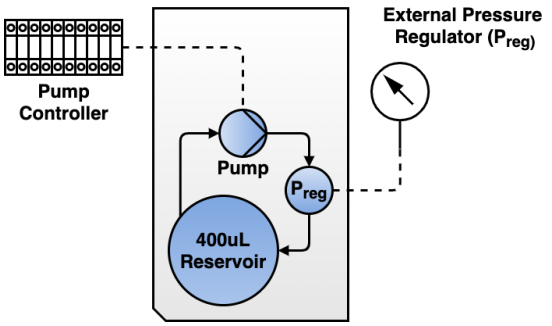

(b) The chip features a 400μL reservoir, a pump, and a back pressure regulator.

Figure 7-1: Photo and schematic for the Media Recirculation Chip design. (a) Photo of an initial prototype of the chip. The pressure regulator diaphragm is partially bonded to the fluidic side of the chamber, a defect that was avoided in later assemblies. (b) Diagram of the fluid circuit with a reservoir, pump, and pressure regulator.

The recirculating media chip can also be used to evaluate the valve sealing characteristics and pump performance. The chip has been used to pump a wide variety of fluids such as Pepto Bismol, milk, and a rheoscopic fluid comprised of glitter and food coloring. Pepto Bismol is not a typical fluid but was used to show pumping of a relatively high viscosity liquid. These fluids were used to demonstrate that media formulations of high density and viscosity can be used, as well as the ability to pump particles. The successful movement of glitter particles through the device offers an indication that monocytes and other small cells could be passed though the pumps without getting stuck to the membrane surface or clogging the pump. Future studies will involve passing cells through the pumps and looking at the viability of different cells.

7.1.1 Analysis of Hormone Absorption

The media recirculation chip was used to evaluate protein adsorption and absorption to the COC materials. This was done in the incubator as shown in **Figure 7-2**. The chip was set to flow at 60 μL/min, and no external pressure was applied to the pressure regulator. A media formulation containing 500 nM (0.157 μg/mL) of progesterone (P4) was created using Endometrial Epithelial Organoid (EEO) based media. 350

μL of the media was then added to two chips and another formulation of Phosphate Buffered Saline (PBS) based media was created. The PBS media has a significantly lower concentration of progesterone due to losses to plates, tubes, and other transfer materials. 350 μL of the PBS based media was then added to the remaining 2 COC pump chips. Both media formulations were also added to PDMS devices of similar volume in static conditions. The devices were kept in the incubator for 3 days and media was sampled each day. The media was analyzed using a progesterone ELISA test to measure the concentration of progesterone on each day.

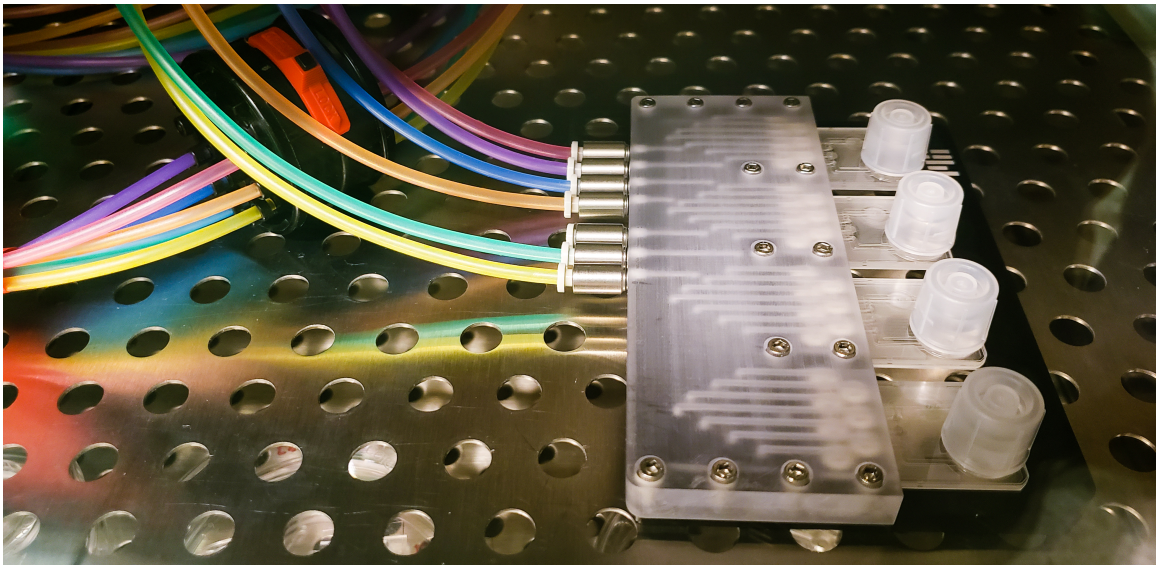

Figure 7-2: 4 pump chips recirculating progesterone containing media in the incubator.

As shown in **Figure 7-3**, the COC chips undergo an initial loss of P4 concentration to the surfaces of the channels but then do not experience a significant loss in concentration beyond the initial adsorption. The PDMS devices experience a significant loss of progesterone due to both absorption and adsorption, so the measured progesterone levels are undetectable on Day 1. This highlights the importance of avoiding PDMS as a material for hormone-sensitive studies. Further, it shows that the adsorption of small molecules to the COC devices is consistent and predictable.

It is hypothesized that the loss of progesterone in the COC devices can be predicted and controlled by using media changes. Once the surfaces in the chip are

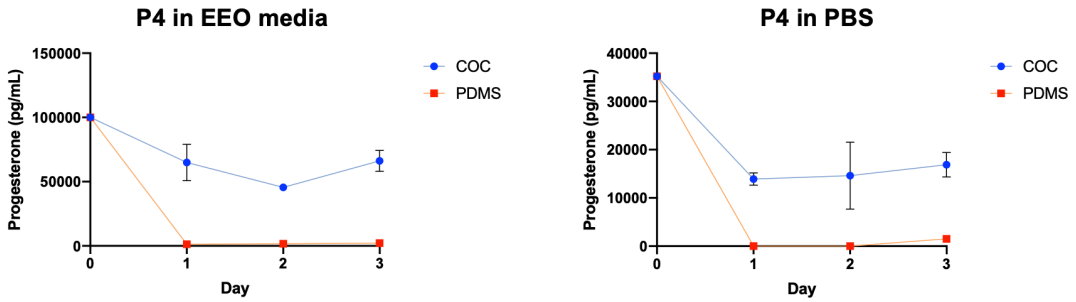

Figure 7-3: Initial results for progesterone (P4) absorption was evaluated in COC and PDMS chips of similar volume. The COC pump chips were recirculated at 60 μL/min and compared to a PDMS chip in static conditions. Progesterone containing media at 500 nM was formulated using EEO and PBS media; N=2 chips for each condition. The COC chips lose a fixed concentration of progesterone due to surface adsorption and the PDMS chips appear to absorb all of the progesterone on Day 1.

saturated with a hormone, drug, or other sticky molecule, they are unlikely to adsorb any more of the saturated compounds. Further testing should be conducted to understand whether progesterone can be adsorbed to the surfaces of the COC devices initially, and then a media change can be performed to replenish the progesterone concentration. We hypothesize that if the surfaces are fully saturated, there will be no further reduction in the progesterone concentration after a media change. Performing future media changes would then allow for complex hormone cycles to be mimicked on the chip. The devices should also be primed with serum or albumin containing media to minimize the initial adsorption. Additionally, the potential for adsorbed molecules to dissolve back into the media should be explored.

7.2 Vascularized Hydrogel Perfusion Chip

A second chip was developed to evaluate whether a chip with integrated micropumps and a controlled pressure drop would help to promote vasculogenesis in a chip. Vasculogenesis is the process of vascular network formation in an embryo or developing tissue and should be distinguished from angiogenesis, the development of new vessels from a pre-existing vascular network. A vascular network can be used to model a

wide variety of metabolic tissues including the blood-brain barrier, skin, lung, and gut. For a project in our lab, a model of the endometrium is of particular interest. This will allow us to study the causes and potential therapies for Endometriosis, a condition defined by ectopic growth of lesions outside of the uterus. In this project, a vascular bed will be used to support fibrotic clusters of cells that mimic the fibrotic lesions found outside of the endometrium. A vascular bed will be created as part of a 3D endometriotic lesion model, to investigate the role of microvasculature in disease establishment and progression.

Creating the conditions for vasculogenesis on a microfluidic device has been previously studied, and the optimal conditions for vascularization of hydrogel materials is similar to those found *in vivo*. The optimal conditions depend on the appropriate levels of Vascular Endothelial Growth Factor (VEGF), as well as physiologically relevant fluidic conditions [124]. Previous studies have shown that fibrin-based gels are most likely to develop a fully perfusable vascular network when there is an average flow velocity of approximately 10 μm/s through the gel [125, 126, 127]. Based on the permeability of fibrin gels, this equates to approximately 2-10 mmH_2O of hydrostatic pressure across the 3mm wide hydrogel channel in the EndoChip [128].

After a healthy vascular network has formed in the hydrogel compartment, the flow through the gel should be increased by adjusting the pressure drop across the hydrogel mmH_2O [129]. This higher flowrate provides the necessary shear stress and nutrient supply to promote angiogenesis from the existing vessels. Eventually, this flow regime could also be used to traffic immune cells through the vessels to simulate an immune response. As the tissue continues to grow, the convective transport of recirculating media should help to replenish the glucose and oxygen metabolized by the tissue. More experimentation will be required to determine the appropriate pressures and flowrates.

To create an interstitial pressure drop across the hydrogel, a chip must be configured with some sort of pressure control system. The first proposed chip design featured a chip with 3 integrated pumps and two elevated reservoirs as shown in **Figure 7-4**. The height of tubing exits in the reservoirs sets the pressure in the two

channels and thus the pressure drop across the hydrogel. Media is recirculated by two pumps connected separately to each channel. A third pump is added to compensate for the media that is passed through the gel; instead of accumulating in the other reservoir it would be returned to the original reservoir. Other methods might be used to redirect the fluid passed through the gel such as a dedicated spillway or Pythagorean siphon [130, 131, 132].

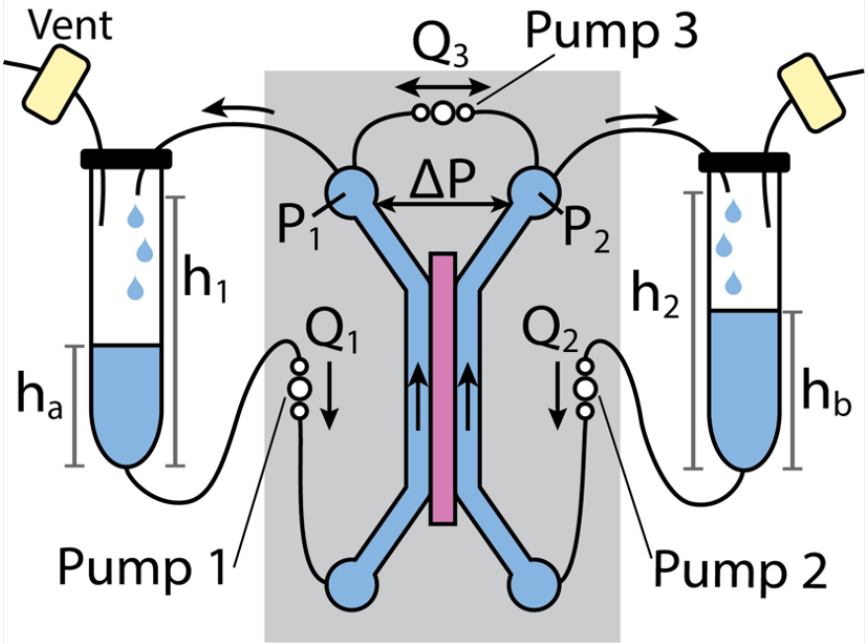

Figure 7-4: The original concept for a perfusable microfluidic device with recirculating media. The chip features a pump for each channel and another pump to maintain a fixed hydrostatic pressure difference between each channel.

This design could meet the fluidic requirements, but a few major challenges led to an alternate design. First, this design would require 3 pumps to provide flow for only two media channels. Second, the height of the fluid in the reservoirs may need to be sensed to provide feedback to control the compensating pump. Third, the pulsatility of the pumps creates a dynamic pressure profile that makes setting a constant hydrostatic pressure profile nearly impossible without an additional pressure regulating element. Finally, the use of two reservoirs would make media sampling more difficult.

As an intermediate step, an initial platform was developed using external pumps

and reservoirs connected to a COC chip with phase guides, but the platform was determined to be too difficult to use for actual testing. This early chip design and pumping platform are shown in **Figure 7-5**.

(a) An early EndoChip prototype with external tubes and pumps.

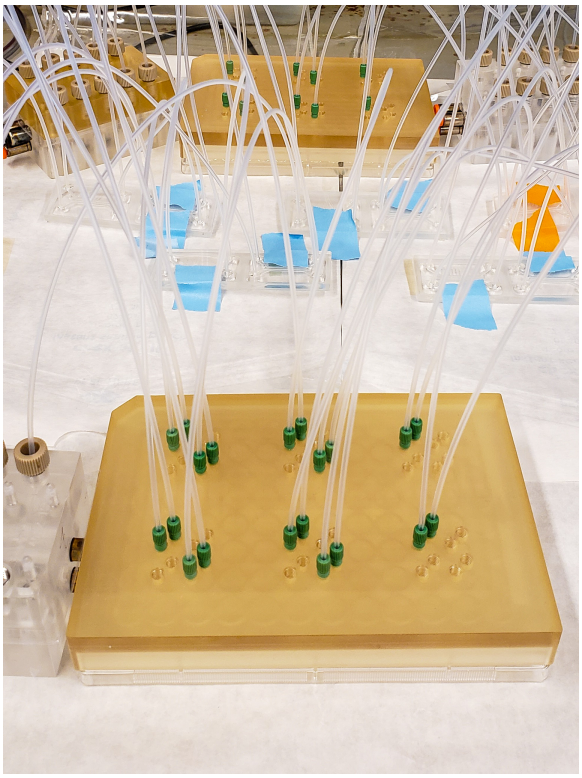

(b) Cumbersome tube connections to the original EndoChip platform.

Figure 7-5: An early prototype of the EndoChip (a) is connected to an external 96-well plate using PTFE tubing (b). The platform is very cumbersome and difficult to use.

These shortcomings led to a final chip design that has a similar behavior to the originally proposed chip design, but with reduced complexity and more control configurations. The proposed chip, which we call the EndoChip, features two synchronized pumps that are each connected to a tissue compartment like the one presented in Section 6. Each channel in the tissue compartment is connected to a back-pressure regulator to set the channel pressure. No accumulator was added to the circuit because the pressure drops in this device are very small and there is significant compliance added by the PDMS cap. At lower pressures the trapped gas accumulator does not provide much fluidic capacitance, so the system's compliance would have still been dominated by the regulator diaphragms. In addition, the trapped gas accumulator has not been validated for longer-term studies and could have caused unforeseen issues in the initial chip validation. Future chips may include a trapped gas accumulator or other capacitive element once these components have been studied further. A diagram of the EndoChip is presented in **Figure 7-6a** and a top-down photo is shown in **Figure 7-6b**.

The chip includes two pumps that are connected to the same pneumatic control signal and thus pump in synchrony. It is important that the two pumps are connected in parallel because this means that any pressure variation due to flow pulsatility will be synchronized as well. Based on previous testing, the pressure should be nearly constant in the channel; synchronizing the pumps just provides an added level of confidence in the pressure control system. Video footage was captured to demonstrate that the motion of the two pumps and pressure regulator diaphragms is synchronous. The reservoir is connected to the fluidic circuit using a single inlet and single outlet.

The chip can be driven in two configurations. In a first configuration, the pumps are driven at a constant flowrate that meets or exceeds the metabolic demand of the tissues by diffusion alone. A pressure difference across the hydrogel can be applied to perfuse media through the gel. The flow through the gel will generally be small compared to the flow through the media channels. This configuration requires the permeability of the gel to be known so that the flowrate through the gel can be accurately predicted. The pressure drop should be increased once the hydrogel is

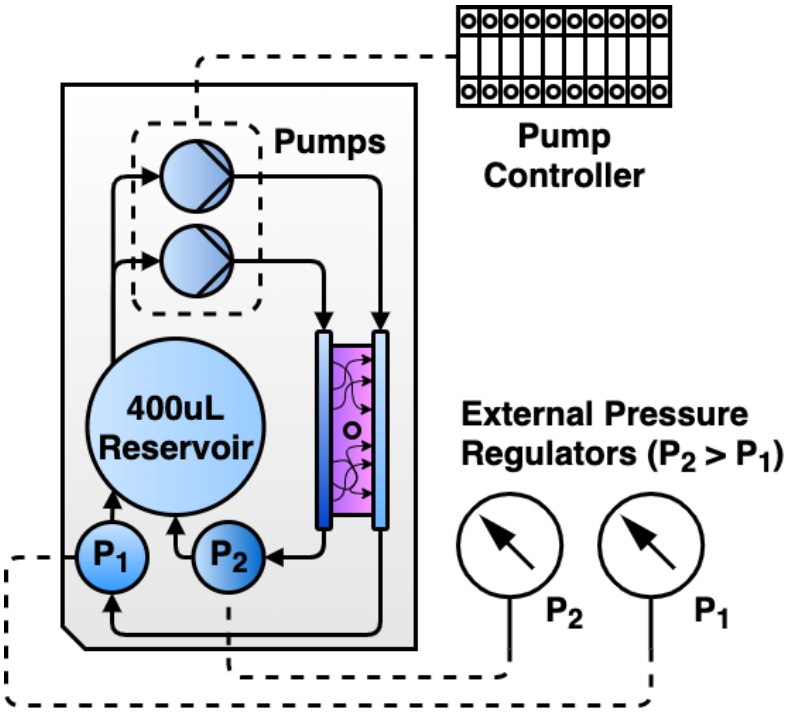

(a) Diagram of the EndoChip fluidic circuit.

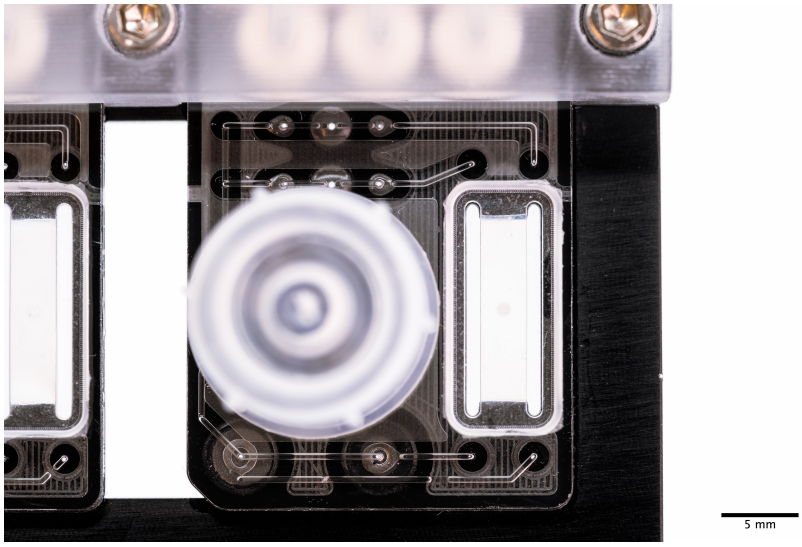

(b) A top-down view of the EndoChip.

Figure 7-6: Two pumps are used to drive a pressure difference across a hydrogel tissue compartment. The pumps are driven at the same flowrate and the pressure regulators are adjustable from 0-2 psi. The 400 μL reservoir is connected to the circuit via a single inlet and single outlet.

vascularized and perfusable.

The second configuration uses a control scheme driving the pumps at a lower

flowrate and blocking one of the pressure regulators. With a pressure drop of around 2 psi across the hydrogel, most of the media from one channel will be directed through the gel. This is particularly true when the gel is fully vascularized and perfusable. This configuration should only be used when convective transport in the gel dominates the intended flow regime (Pe $>$ 10) [133, 134].

7.2.1 Vascularized Co-Culture of HUVEC and NHLF Cells

Vascularization of endothelial cells was explored using previously built models for phase-guide based devices and translated to the new tissue compartment presented in Chapter 6. A total of 4 chips were used in the pilot study. Fibrin gel was used for 3 of the tissue compartments and one chip was loaded with a PEG-based gel. It was hypothesized that too high of a pressure drop might lead to collapsed microvessels in the fibrin gel, despite providing a better chance for vascularization in the PEG-based gel. For this reason, the selected pressure drops were determined using models built for fibrin gels.

Based on previous lab experiments and a comprehensive literature review, an interstitial pressure drop of 0.014 psi across the 3 mm wide fibrin compartment should provide the best conditions for vascular network formation [125, 124, 126, 128, 127, 135]. The system had not yet been validated such a small pressure drop, so a pressure calibration was performed for the pilot study. To perform this calibration, the gel compartment on a chip was filled with NOA81 UV curable adhesive to isolate each media channel. Two PTFE tubes were glued to the top of the EndoChip using Dymax 1072-M UV adhesive and an acrylic alignment bracket. These tubes are joined to the tissue compartment media channels and act like a water column for precise pressure measurement. This system does not capture instantaneous spikes in pressure from the pumps, but does a good job at showing the steady-state pressure bias of the system. The pumps were set to flow at 60 μL/min and the pressure regulator was adjusted from 0-1 psi gas pressure. The change in hydrostatic pressure in the media channel was measured using a ruler. This pressure calibration is presented in **Figure 7-7**. A cross-channel pressure drop of 0.09 psi was set using the external pressure regulators;

0.40 psi for the low pressure channel and 0.49 psi for the high pressure channel. This externally applied pressure difference equates to approximately 10 mmH_2O across the hydrogel. In the future, further pressure calibration is recommended to enable more accurately controlled pressure differences.

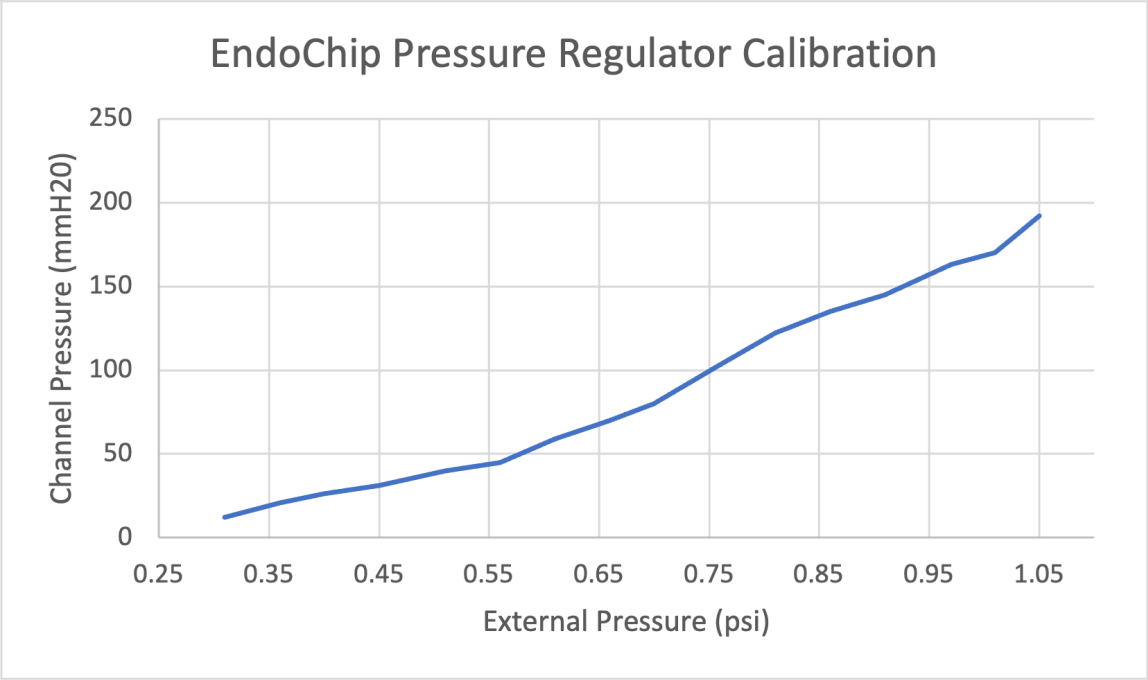

Figure 7-7: Pressure calibration for the EndoChip design. Plot shows channel liquid pressure versus externally applied pneumatic pressure.

HUVEC cells were seeded at a density of 10 M/mL and NHLF cells were at 1 M/mL to meet a 10:1 ratio of endothelial and fibroblast cell concentrations. The fibrin gel formulation was 50% fibrinogen and 50% thrombin. The PEG gel formulation was 3 wt% PEGVS, 35% XL, 1.5 mM SYNKRGD, 1.5 mM GFOGER, 0.5 mM BM Binder, and 0.5 mM FN Binder. Vasculife culture media with added supplements was used. Media changes were performed daily to maintain high glucose levels in the device. The same protocol was used to seed cells in an AIM Biotech chip [11, 13] for comparison.

Loading of hydrogels into the new platform was done by pipetting 36 μL of gel into each tissue compartment; 38 μL is initially aspirated into the pipette to provide some room for error. After loading, the gels were left to polymerize at 37°C in the incubator for 20 minutes. Once the gels were polymerized, the device was removed from the

incubator and the PTFE gel guides were removed with tweezers. An image of cells loaded into EndoChip on Day 0 is provided in **Figure 7-8**. The PDMS caps were installed into the device and 350 μL of media was added to the reservoirs. The pumps were turned on using our controller and a portable pressure/vacuum supply. When performing this step two major issues were encountered. First, the back pressure regulator diaphragms were sealed shut from the bonding process and resisted the flow from the pumps. This resulted in an overpressure event that caused a leak from the PDMS caps in all 4 chips. The diaphragms were eventually opened by applying vacuum for a few minutes. The second issue was that the PDMS caps were soft and sticky after being sterilized using ethylene oxide (EtO). These softer caps were difficult to seal properly and leaked on all but one chip. A cap redesign with a tighter fit was implemented for future studies, and EtO was not used for sterilization of the caps going forward. The caps were instead sterilized with 70% ethanol.

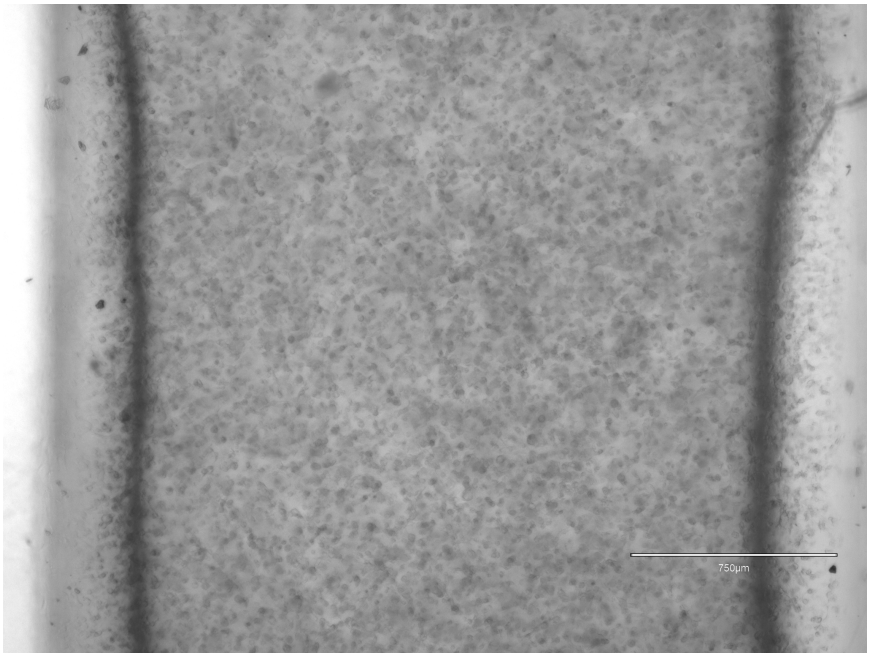

Figure 7-8: Day 0: A fibrin gel with a 10:1 ratio of HUVEC and NHLF cells loaded into the EndoChip. The media channels are observable on the left and right of the gel channel. The channel is cloudy due to the cell loading.

By the end of Day 1, all 3 of the leaking devices were dried up and all of the media was lost. These chips were retired from the test, leaving only one fibrin chip for further

analysis. Despite the initial sealing issues, the one remaining chip was fully functional with operable pumps and pressure regulators. The cap was left undisturbed and the gel channel was imaged daily. By the end of Day 1, cell migration was observed and small clusters of endothelial cells began to form. The fibroblasts began to elongate and connect the endothelial clusters. These formations are an early sign of vasculogenesis and are observable in **Figure 7-9**. By Day 2, the networks were more pronounced in both the EndoChips and AIM chips, and can be seen in **Figure 7-10**. Unfortunately, the network density was too low to support further growth and the network formation stagnated on Day 4. At this point, some dead endothelial cells began to appear as small black dots in the vessels as shown in **Figure A-2**.

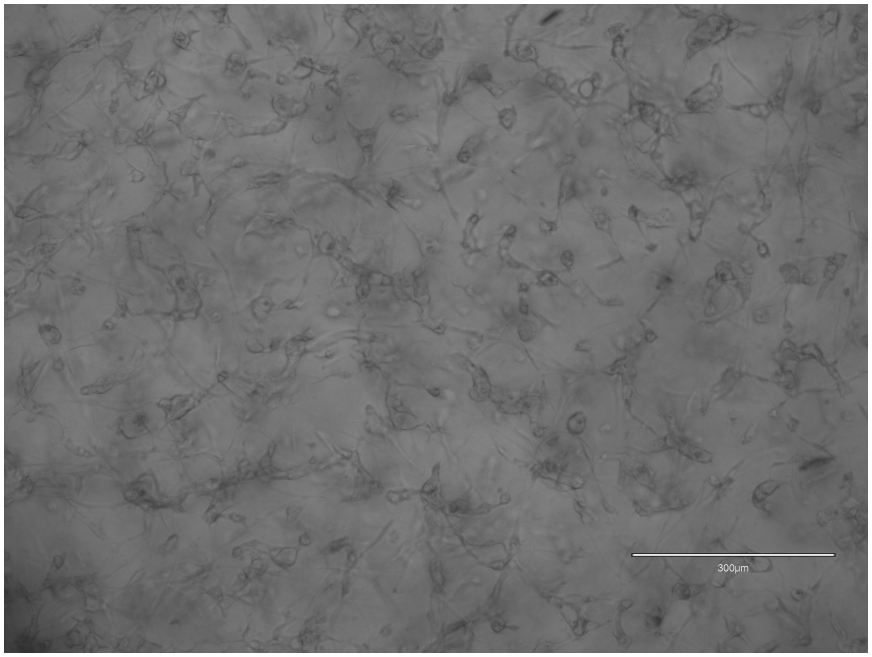

Figure 7-9: Endothelial cells begin forming small clusters and fibroblasts begin to restructure on Day 1. This behavior indicates that the cells survived the installation process and are undergoing the beginning stages of vasculogenesis.

Once networks were mostly formed, a 1 M/mL concentration of HUVEC cells were seeded onto the sides of the gel as described below. These additional cells help to open up the vascular networks to the media channel. This procedure was performed in the AIM chips by emptying the existing media in one channel and replacing it with the cell-laden media. The device was then tilted sideways for 10 minutes and

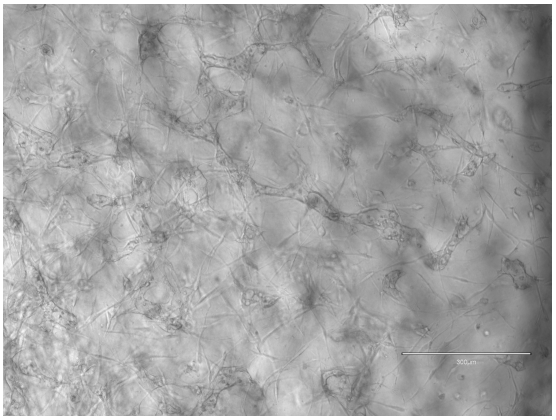

(a) Network formation in the EndoChip on Day 2.

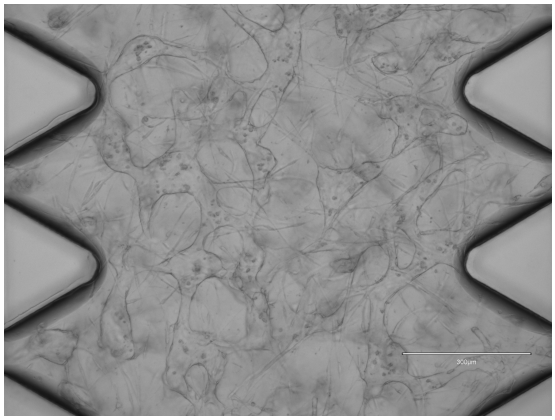

(b) Network formation in the AIM chip on Day 2.

Figure 7-10: Similar vascular network formations are observed in both EndoChip and AIM devices by the end of Day 2.

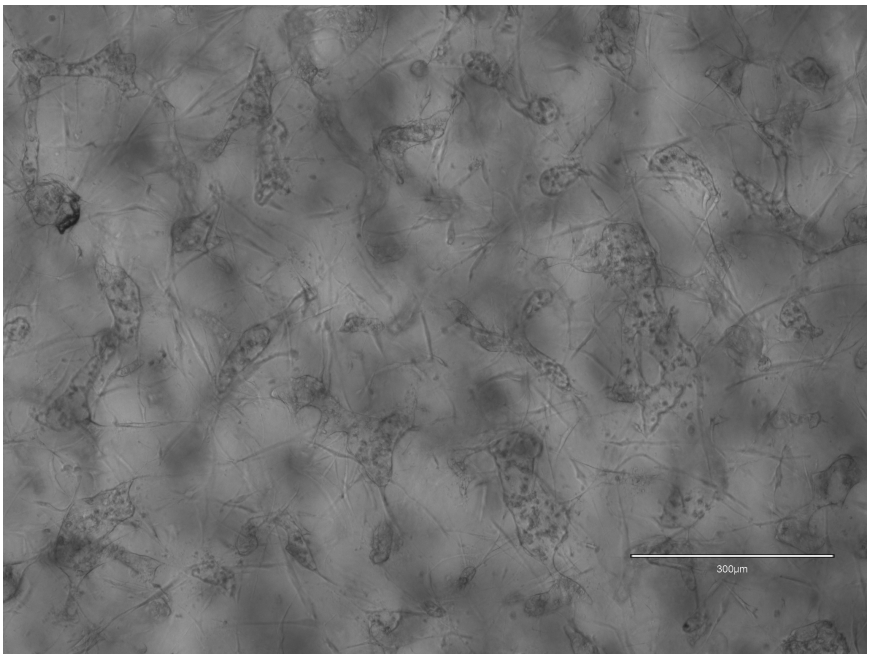

Figure 7-11: No additional network formation in the EndoChip by Day 4. Some dead cells appear as darker spots in the network.

the process was repeated for the other side. An image of cells loaded in the AIM chip is presented in **Figure A-3**. Cells were loaded in the EndoChip by removing all existing media and then loading the reservoir with 150 μL of the cell-laden media. The pressure regulators were disengaged by applying pneumatic vacuum to lift the regulator diaphragms, and the pumps were driven at 30 μL/min. The cells were

successfully loaded into the media channels using this technique and are pictured in **Figure 7-12**. The platform was tilted sideways by 45° for 10 minutes on each side in the incubator to encourage the cells to settle and adhere to the gel wall. Some of the added cells appear to bind to the gel channel as expected. After the cells had a chance to settle the pumps were turned back on at 60 μL/min.

Figure 7-12: Additional cells were seeded onto the hydrogel walls of the EndoChip on Day 5. Cells were loaded into the channels using the onboard pumps.

No further network formation in the EndoChip was observed for the remainder of the test, but cells remained alive in the device for 10 days. At this point the test was ended and equipment was reconfigured for a second trial. The second trial used the same fluidic conditions with redesigned PDMS caps for improved sealing. This new cap is pictured in **Figure A-4**. The same chips were used in this study, and the pumps were validated prior to hydrogel installation. The remaining gel was removed from the chips by pumping 1% trypsin through the device to break down the hydrogel components. The chips were then cleaned using 7X detergent in an ultrasonic bath for 45 minutes, followed by a rinsing step with DI water, and then washed with 70% ethanol for sterilization. New culture tube caps and PTFE gel guides were installed into the chips, and the entire platform was sprayed down with ethanol and left to

evaporate in an EtO pouch for 2 days.

The second trial went significantly better than the first. The gels were easy to install, and the new PDMS caps were able to seal the devices without any leaks. The new caps also appear to reduce the amount of trapped bubbles in the fluid in the media channels. The cells are observed at 10x magnification from Day 0 to Day 3 for early signs of vascularization, andd all 4 of the chips show consistent and similar results. Images taken daily of each chip are shown in **Figure 7-13**. By Day 3, some of the vascular networks are able to be perfused. Small particles of cellular debris were observed traveling through the networks and recorded on video. The direction of the particle movement is consistent with the direction of the applied pressure difference.

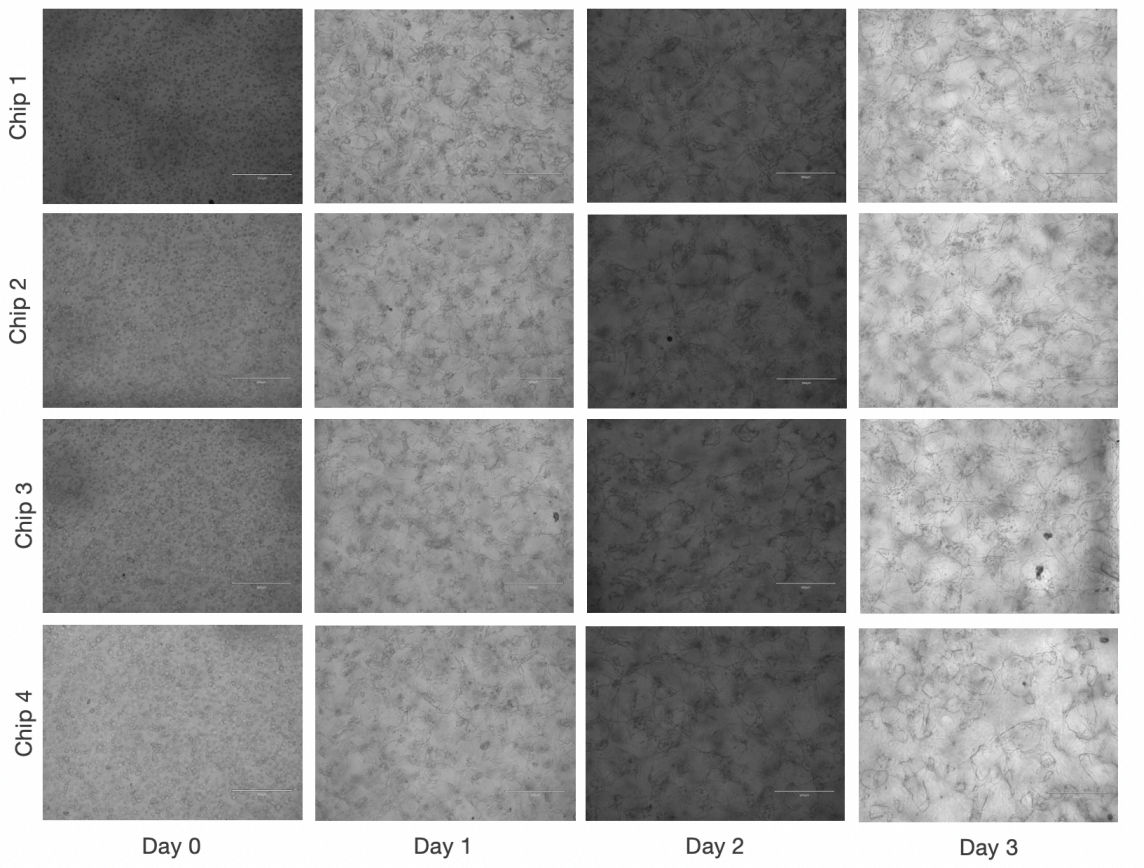

Figure 7-13: 4 EndoChips experience similar levels of vascularization in the devices. By Day 3 some of the networks are fully perfusable and able to traffic small particles.

The only major flaw in the test was that several of the hydrogels had a small cavity at the gel installation port. It is likely that this was caused by the liquid ejection

function of the pipette, which may have injected some air into the gel channel. These cavities had a tendency to grow over time, and created an opening in the center of the hydrogel channel in 2 of the chips. Further damage to the hydrogel from this original defect can be observed in **Figure 7-14**. It is also possible that the contracted shape of the hydrogel is due in part to cellular forces acting on the ECM. This issue will be explored further in future studies, but is not currently a major concern. Use of the pipette liquid ejection function should be avoided in future studies to prevent this extra bubble from forming in the gel channel.

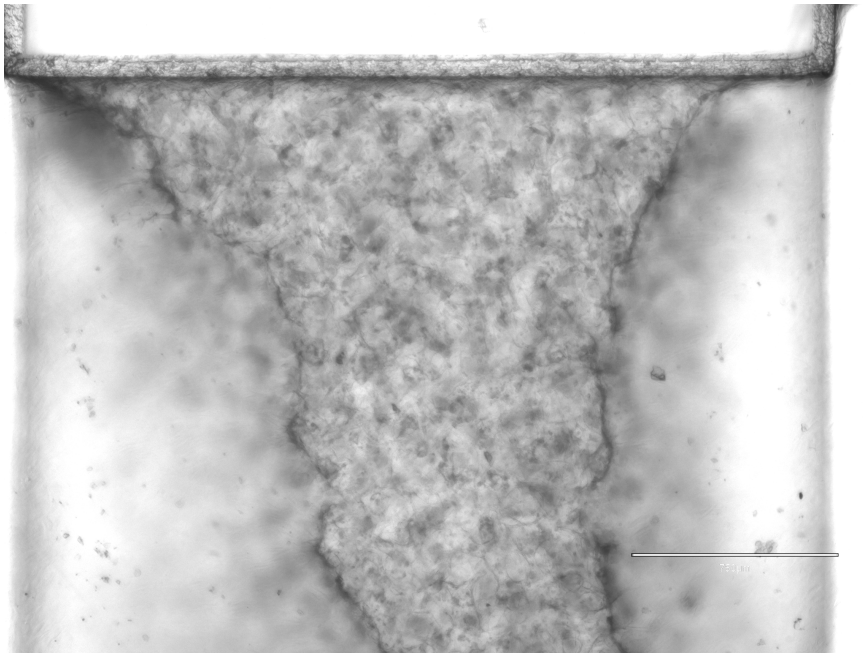

Figure 7-14: A bubble at the gel installation port creates an initial defect in the fibrin hydrogel that grows over time. This is exemplified by the tapered shape of the hydrogel and an opening at the center of the tissue compartment. This shape may be caused by damage to the hydrogel due to flow as well as contraction of the hydrogel due to cellular forces acting on the ECM.

Most of the tissue compartments were perfusable by Day 5. To demonstrate the perfusability of the vascular network, 40kDa fluorescent Dextran is added into the reservoir of the chip and its distribution throughout the device is observed under a fluorescent microscope. The pumps were driven at 30 μL/min during imaging. An image of a vascular network perfused with Dextran media is presented in **Figure 7**. The vascular structures are 3D in nature and are fully perfusable in the hydrogel

channel. The process is relatively fast, but can be observed live on the microscope.

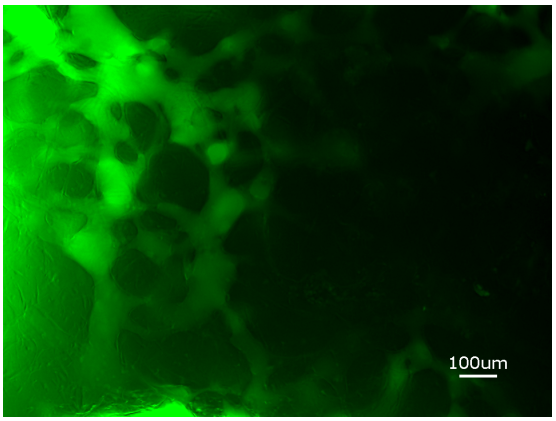

(a) Dextran is gradually perfused into the vascular network using the onboard pumps.

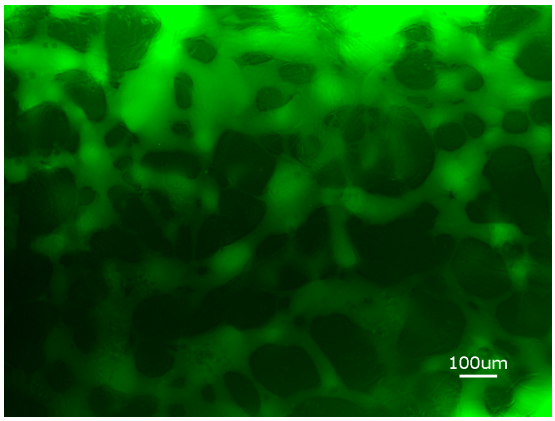

(b) A fully perfusable region in the hydrogel compartment.

Figure 7-15: An EndoChip was perfused with 40 kDa Dextran added to the media and imaged using GFP. The fluorescent media reveals the internal structures in the channel and confirms the perfusability of the device.

The cells were then fixed with 4% paraformaldehyde (PFA) for 30 minutes prior to staining. The cells were stained with actin, DAPI, and Ulex europaeus agglutinin 1 (UEA-I) peroxidase and left pumping overnight on a rocker plate so that the stains would have more time to bind onto the cells. Actin is used to mark the cytoskeleton of both the endothelial and fibroblast cells, DAPI targets the cell nuclei, and UEA-I selectively stains the endothelial cells. The next morning the staining media was replaced with PBS to eliminate background noise during subsequent imaging procedures.

The EndoChips were imaged using the GFP, DAPI, and TX Red channels on an EVOS M5000 microscope as well as a Keyence BZ-X700. Multiple wavelength channels can be imaged at once and stacked on top of each other to get a clear view of the vascular structures. One example of this overlay process is presented in **Figure 7-16**. An additional view of the endothelial cell networks is provided in **Figure 7-17**.

Overall, the EndoChip shows consistent and reliable formation of vascular networks. Different cell concentrations, flowrates, and interstitial pressure differences should be explored for a variety of hydrogel biomaterials to fully characterize the parameter space for forming physiological microvasculature.

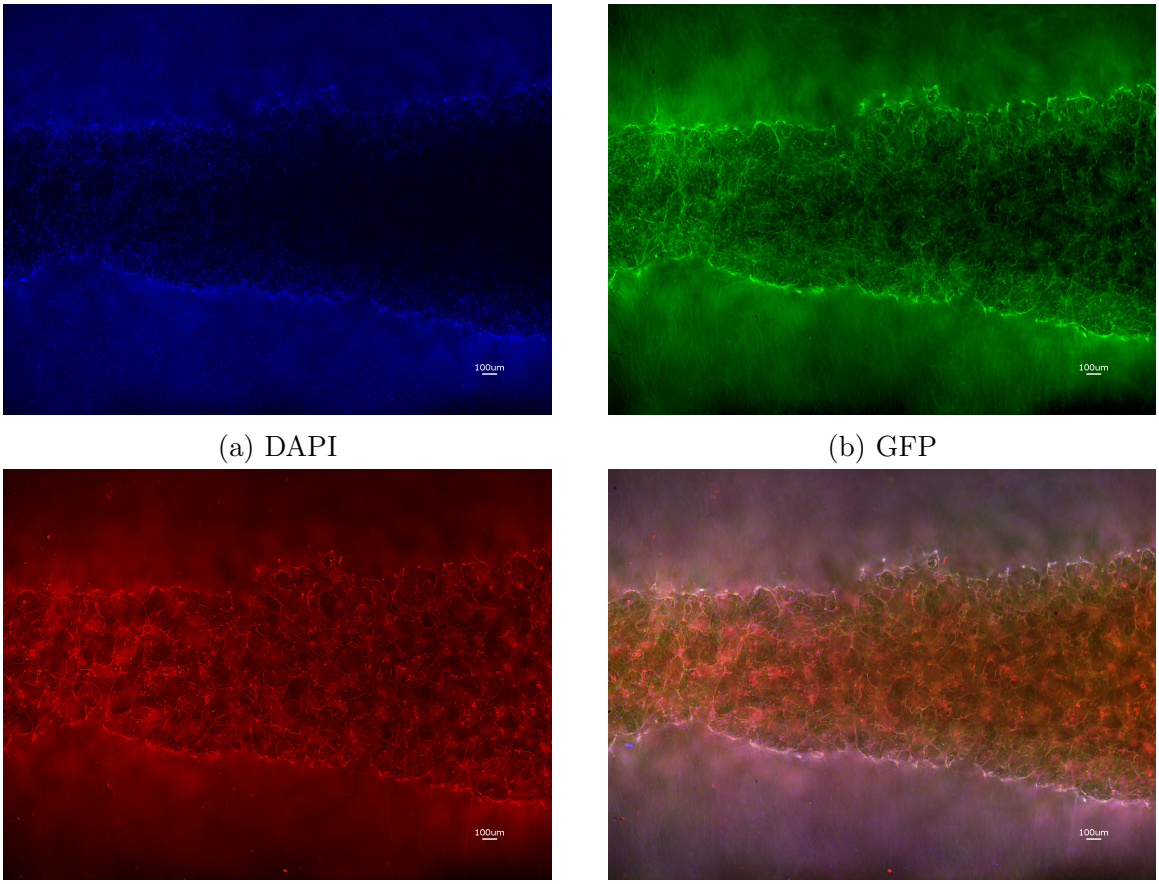

(a) DAPI

(b) GFP

(c) TX Red

(d) Overlay of all 3 images

Figure 7-16: The vascular structures are fixed with PFA and stained using DAPI for the cell nuclei, actin for the cytoskeleton, and UEA-I for the endothelial cells. The images were taken near the center of the EndoChip at 4x magnification with the media channels observable on the top and bottom of each image. (a) The cell nuclei appear as blue dots on the DAPI channel. (b) The cell cytoskeleton, and particularly the elongated fibroblasts, appear in green on the GFP channel. Many of the fibroblasts bind to the bottom of the media channels where a thin layer of fibrin gel is present on the E-140 interface. (c) The endothelial cell networks appear red on the TX Red channel. These structures are 3D in nature and are perfusable across the channel. (d) The fluorescent channels can be stacked on top of each other to see all of the structures at once.

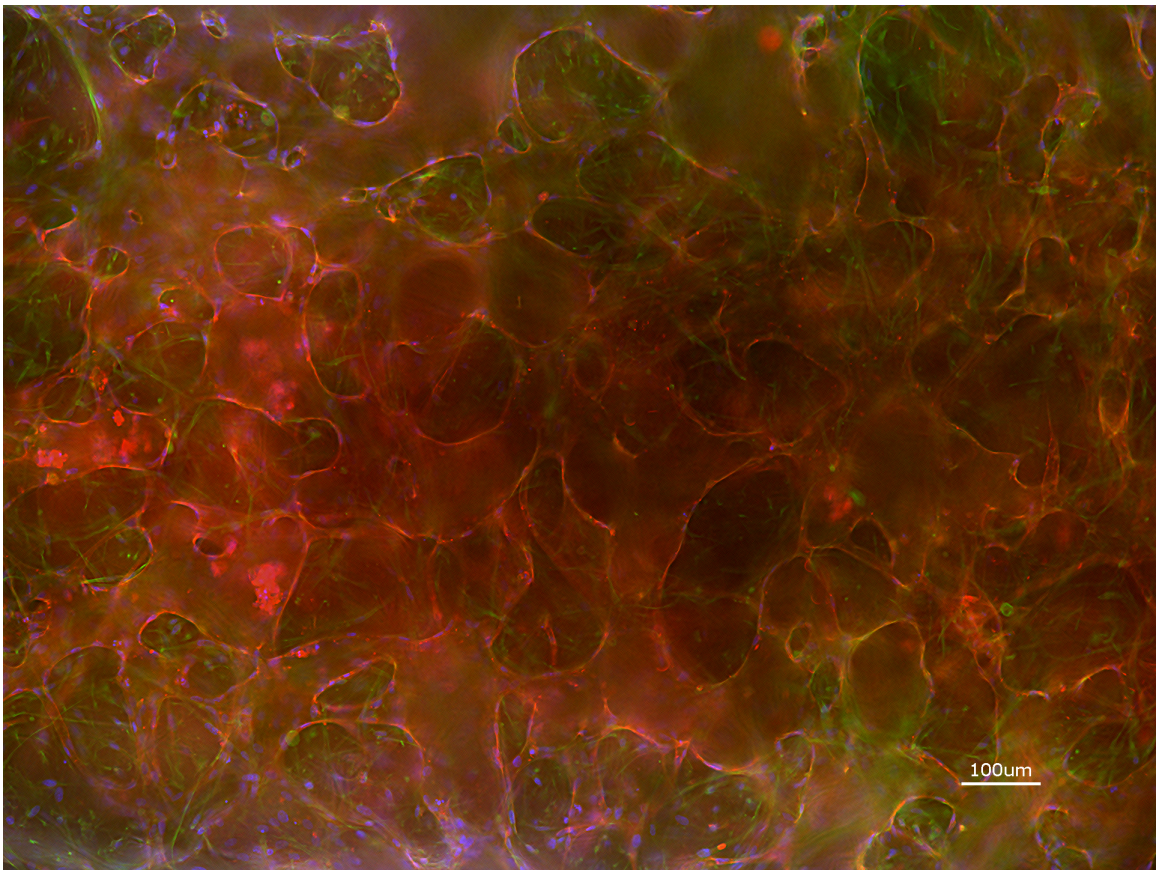

Figure 7-17: Well-defined fluorescent images of vascular networks can be captured on the EndoChip. These types of images help to provide qualitative insights into the physiological relevance of tissue models developed in the chip.

Chapter 8

Conclusions and Suggestions for Future Work

8.1 Summary

We have designed, fabricated, and validated a high-throughput Organ-on-a-Chip platform for control of physiological processes. The platform enables precise control of channel pressures and flowrates using disposable multi-layer thermoplastic microfluidic chips with integrated elastomeric membranes. The device uses a 3D printed manifold that connects 4 microfluidic chips to 7 pneumatic signals via a standardized pneumatic interconnect. These signals are used to control the onboard pumps, valves, and pressure regulators. The 5-layer chips are made of Cyclic Olefin Copolymers and assembled using primarily thermal bonding techniques. A custom COC elastomer membrane and co-extruded COC optical film were developed to facilitate fast and reliable bonding of the chips. Techniques for manufacturing the chips at scale are explored.

A pneumatic valve, a micropump chamber, a fluidic accumulator, and an on-chip pressure regulator were developed to provide precise control of channel flowrates and pressures. The membrane-based elements were designed using a hyperelastic FEA model and their performance was evaluated using pressure and flow sensors connected to a test chip. The valve and pump chamber were integrated into a pneumatic mi-

cropump design and used in several chip designs. The pumps can be driven from 0-3 μL/s using solenoid valves. The on-chip pressure regulator is able to regulate channel pressures from 0-2 psi using an externally applied pressure source. A microfluidic accumulator is used to store liquid under pressure and was shown to smooth out fluid flow.

The platform was validated in two biological studies. First, a chip with a single pump and pressure regulator was used to recirculate a media formulation containing progesterone. Some progesterone was lost due to adsorption to the surfaces of the chips, but far less than the absorption observed in PDMS-based devices. The effect of surface adsorption can possibly be avoided in future studies by using proper surface treatments and priming procedures, or accounted for by using routine media changes. A second chip was developed to vascularize a co-culture of endothelial and stromal cells. A novel tissue compartment was developed to constrain 36 μL of hydrogel in a rectangular geometry. The tissue compartment includes PTFE components that are used to constrain the gel while polymerizing and are removed after gel polymerization. The device is then sealed using an elastomeric cap. The compartment was integrated into the final chip design, named the EndoChip, and used to contain a 10:1 ratio of HUVEC and NHLF cells in a fibrin gel. Channel flowrates of 60 μL/min and an applied interstitial pressure difference of 10 mmH_2O and were used to promote vasculogenesis.

The platform sets a foundation for building advanced tissue models and running high-throughput experiments with recirculating media. Future studies will be conducted to explore the optimal device parameters for long-term culture with a variety of hydrogel biomaterials. Future iterations of the EndoChip design will be used to build physiologically relevant fibrotic lesion models for studies of Endometriosis.

8.2 Suggestions for Future Work

The 4 main directions for future work on this platform include: determining the feasibility of manufacturing multi-layer COC chips at scale, improving the sterility

and ease-of-use of the platform, improving the pumping system to provide smooth fluid flow, and designing chips to accommodate new tissues.

8.2.1 Infrared Bonding

Feasibility of scale manufacturing of multi-layer COC chips with integrated elastomer membranes will be determined by the ability to join the elastomer membrane in the middle of the chip. During this process, the membrane is mechanically unsupported and is prone to warping or bonding undesirably to other regions in the chip. One proposed method for avoiding this is to bond the chips using infrared laser welding techniques. Ideally, a scan laser system would be used to reduce the heat load on the part and allow for more selective welding. An alternative method is to use an array of fiberoptic laser beams projected at the seam lines. The exact light intensity, exposure time, and bonding pressure should be fully explored. The preservation of the diaphragms should be validated by measuring pump chamber displacement volumes, sealing pressure of the valves, and by delaminating and inspecting the chips. A bond strength nearing the tensile strength of TOPAS E-140 should be possible using this method. This project may require the use of photomasks for protecting the membrane material and should be done in vacuum if possible. The process should also be made fast and sterile.

8.2.2 Sterility and Media Exchange

The platform currently suffers from a few sterility concerns. First, the reservoir caps are not tight sealing and should have a better seal in future chip designs. This could be accomplished using a screw-on cap or simply by changing the dimensions of the reservoir. The elastomeric tissue compartment caps should also be improved to have better sealing characteristics and to be more sterile. Currently, the bottom of the cap is exposed and does not trap incoming contaminants. The addition of an overhanging perimeter, similar to the that on a Petri dish, could be used to prevent contaminants from entering the tissue compartment.

8.2.3 Manifold Connections

The existing pneumatic manifold is simply bolted to the aluminum base plate because it was easier to develop and was sufficiently easy to use for early testing. A better mechanism would use a quick clamp that compresses the O-rings and locks the manifold in place. This mechanism will make loading chips into the device easier and reduce the chance of user error during assembly.

Additionally, the manifold should be designed to include a quick connect to the pneumatic control unit. The use of push-to-connect fittings and tubing that is connected to a 10-port connector is cumbersome and results in too much clutter in the incubator. A better solution is to get rid of the tubing and have the platforms connect directly to the pneumatic control unit. This connection should be valved on the control unit so that one platform can be removed while the other platforms are running. Eventually, the control unit should exist outside of the incubator and provide the proper temperature and humidity for tissue culture.

8.2.4 Pump Characterization

Although the pump has been evaluated extensively in this thesis, more work is required to better characterize and improve the final pump design. The pump should be evaluated over a range of head pressures and configured with valves that operate at a higher actuation pressure than the pump chamber. This will help to ensure that the valves seal properly and allow for lower pressures to be used on the pump chamber. Further, the displacement volume of the pumps and valves should be verified using an analytical scale and a beaker. This type of flow totalizer will allow for more precise measurement of the average flowrate than is possible with the Sensirion flowmeters used in this project. The teardrop valve performance should also be evaluated in both directions and over a wider range of actuation and head pressures. Existing data only describes the sealing characteristics of the valve in one direction with an actuation pressure of 5 psi.

8.2.5 Pump Control

The pumps can also be improved using a new control scheme. In a preferred configuration, two pumps chambers will be driven out of phase with each other and dispense fluid into the same channel. This will allow for one pump to be dispensing fluid while the other pump is aspirating fluid. Further, the actuation of the pump chamber should be controlled using an electronically controlled pneumatic pressure regulator so that pressures can be applied more gradually. This will help to smooth out the flow pulsations from the pump chamber. This pump configuration should be tested against a range of head pressures and it is possible that the pump could be controlled using feedback from a pressure or flow sensor.

8.2.6 Tissue Integration

New methods for tissue integration in these types of COC devices should be explored. Several examples of these tissue integration methods are presented in Chapter 6, but other tissue scaffolds and installation methods should be explored. The chips should be optimized for liver, skin, kidney, brain, and gut tissue. Other organs are also possible, but these are the most critical organs for drug and disease modeling.

8.2.7 On-Chip Oxygenator

The integration of new tissues may require the design, testing, and implementation of an on-chip oxygenator. Most thermoplastics have significantly lower gas permeability than PDMS, which may result in reduced oxygenen levels in microfluidic devices for cell culture [136]. Some tissues, including hepatocytes found in the liver, have a relatively high metabolic rate, and demand more oxygen than the cells used in this thesis [137]. In other tissues, such as the gut microbiome, hypoxic conditions may be required [64, 138, 139]. The diffusion characteristics of polymer films have been studied extensively, and many polymers with high gas permeability, such as PTFE, could be used as a membrane material [140, 141]. The oxygenator may be configured with closed loop feedback using on-chip sensors or imaging based monitoring of oxygen

levels on the chip [142, 143].

8.3 Conclusions

The platform described in this thesis is designed to provide correct fluidic conditions for vascularization of endothelial and stomal cells *in vitro*. We conclude that this device is able to provide an interstitial pressure and channel flowrate that promotes vasculogenesis in a fibrin hydrogel. Further experimentation with the device will help to verify the consistency and performance of the EndoChip and inform future chip designs.

The COC chips have strong bonds, are optically clear, and demonstrate sufficiently low levels of hormone adsorption for most experiments that are sensitive to hormone concentrations. The on-chip pumps, valves, and pressure regulators provide consistent flowrates and pressures in the chips. The new tissue compartment is able to contain a relatively large amount of hydrogel without the use of phase guides and is relatively easy to use. The platform enables a wide range of hydrogel biomaterials and is reconfigurable for different testing conditions. This system sets a foundation for long-term culture of metabolically active tissues and is a promising new technology for advanced microphysiological models.

Appendix A

Figures

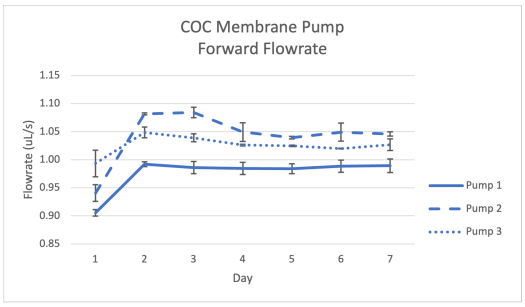

(a) Pump performance in the forward direction.

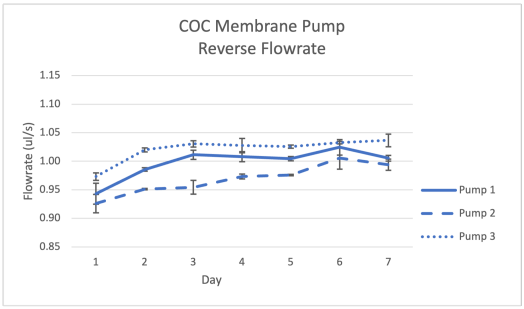

(b) Pump performance in the forward direction.

Figure A-1: An E-140 membrane was used in an old pump design to see if it could be used for future pumping platforms. The membrane material required more actuation pressure, but was able to maintain accurate and consistent flowrates.

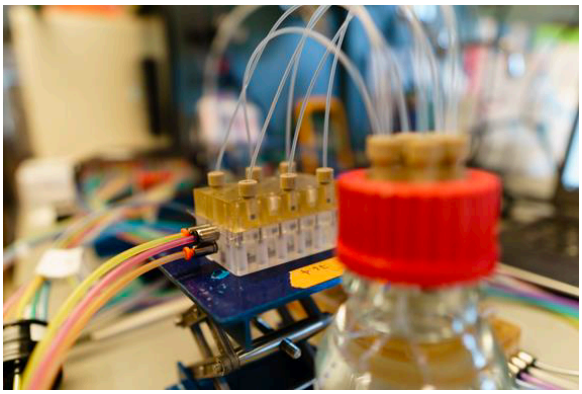

Figure A-2: The E-140 membrane is evaluated for use in a previously developed micropump [78].

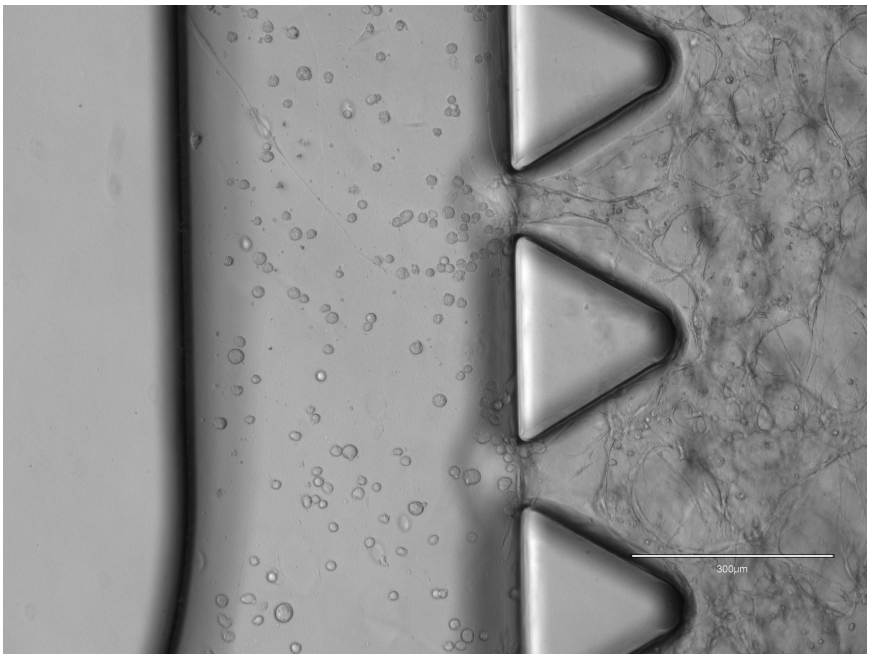

Figure A-3: Additional cells were loaded into the AIM chip on Day 4.

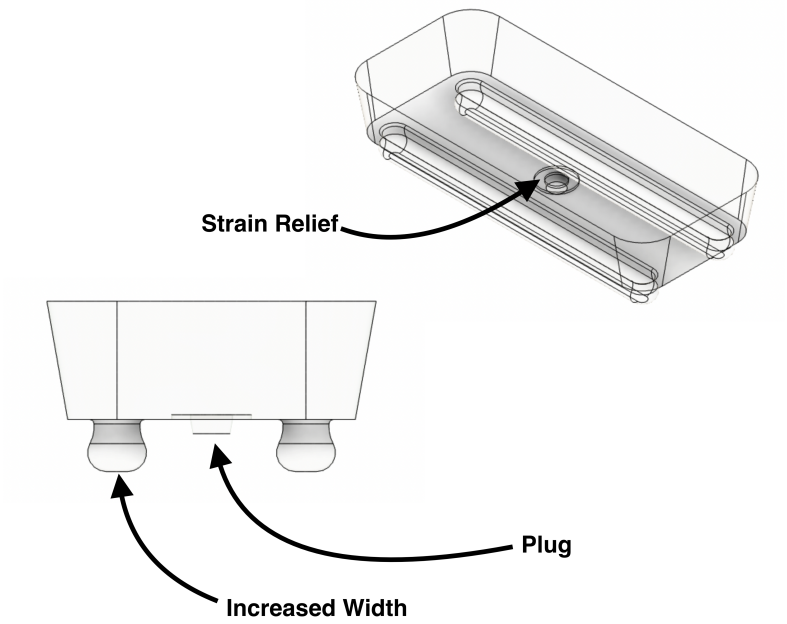

Figure A-4: The redesigned PDMS cap has an additional plug for sealing the gel installation port and a larger bump for a tighter seal. The new cap design has worked on multiple chips without any sealing issues.

Bibliography

[1] M.-H. Wu, S.-B. Huang, and G.-B. Lee, "Microfluidic cell culture systems for drug research," *Lab on a Chip*, vol. 10, no. 8, p. 939, 2010.

[2] M. L. Coluccio, G. Perozziello, N. Malara, E. Parrotta, P. Zhang, F. Gentile, T. Limongi, P. M. Raj, G. Cuda, P. Candeloro, and E. Di Fabrizio, "Microfluidic platforms for cell cultures and investigations," *Microelectronic Engineering*, vol. 208, pp. 14–28, Mar. 2019.

[3] C. D. Edington, M. Cirit, W. L. K. Chen, A. M. Clark, A. Wells, D. L. Trumper, and L. G. Griffith, "Integration of systems biology with organs-on-chips to humanize therapeutic development," B. L. Gray and H. Becker, Eds., San Francisco, California, United States, Feb. 2017, p. 1006113.

[4] W. L. Chen, C. Edington, E. Suter, J. Yu, J. J. Velazquez, J. G. Velazquez, M. Shockley, E. M. Large, R. Venkataramanan, D. J. Hughes, C. L. Stokes, D. L. Trumper, R. L. Carrier, M. Cirit, L. G. Griffith, and D. A. Lauffenburger, "Integrated gut/liver microphysiological systems elucidates inflammatory inter-tissue crosstalk: Integrated Gut/Liver Microphysiological Systems," *Biotechnology and Bioengineering*, vol. 114, no. 11, pp. 2648–2659, Nov. 2017.

[5] C. Maass, M. Dallas, M. E. LaBarge, M. Shockley, J. Valdez, E. Geishecker, C. L. Stokes, L. G. Griffith, and M. Cirit, "Establishing quasi-steady state operations of microphysiological systems (MPS) using tissue-specific metabolic dependencies," *Scientific Reports*, vol. 8, no. 1, p. 8015, Dec. 2018.

[6] C. Maass, C. L. Stokes, L. G. Griffith, and M. Cirit, "Multi-functional scaling methodology for translational pharmacokinetic and pharmacodynamic applications using integrated microphysiological systems (MPS)," *Integrative Biology*, vol. 9, no. 4, pp. 290–302, 2017.

[7] C. Hu, Y. Chen, M. J. A. Tan, K. Ren, and H. Wu, "Microfluidic technologies for vasculature biomimicry," *The Analyst*, vol. 144, no. 15, pp. 4461–4471, 2019.

[8] A. Brown, H. He, E. Trumper, J. Valdez, P. Hammond, and L. G. Griffith, "Engineering PEG-based hydrogels to foster efficient endothelial network formation in free-swelling and confined microenvironments," *Biomaterials*, vol. 243, p. 119921, Jun. 2020.

[9] J. H. Sung, Y. I. Wang, N. Narasimhan Sriram, M. Jackson, C. Long, J. J. Hickman, and M. L. Shuler, "Recent Advances in Body-on-a-Chip Systems," *Analytical Chemistry*, vol. 91, no. 1, pp. 330–351, Jan. 2019.

[10] T. Hasenberg, "Emulating the human vasculature in a Multi-Organ-Chip platform - Rheology and vasculogenesis," p. 169.

[11] S. Chung, R. Sudo, P. J. Mack, C.-R. Wan, V. Vickerman, and R. D. Kamm, "Cell migration into scaffolds under co-culture conditions in a microfluidic platform," *Lab Chip*, vol. 9, no. 2, pp. 269–275, 2009.

[12] V. Vickerman and R. D. Kamm, "Mechanism of a flow-gated angiogenesis switch: early signaling events at cell-matrix and cell-cell junctions," *Integrative Biology*, vol. 4, no. 8, p. 863, 2012.

[13] M. Campisi, Y. Shin, T. Osaki, C. Hajal, V. Chiono, and R. D. Kamm, "3D self-organized microvascular model of the human blood-brain barrier with endothelial cells, pericytes and astrocytes," *Biomaterials*, vol. 180, pp. 117–129, Oct. 2018.

[14] S. J. Trietsch, E. Naumovska, D. Kurek, M. C. Setyawati, M. K. Vormann, K. J. Wilschut, H. L. Lanz, A. Nicolas, C. P. Ng, J. Joore, S. Kustermann, A. Roth, T. Hankemeier, A. Moisan, and P. Vulto, "Membrane-free culture and real-time barrier integrity assessment of perfused intestinal epithelium tubes," *Nature Communications*, vol. 8, no. 1, p. 262, Dec. 2017.

[15] D. Huh, H. J. Kim, J. P. Fraser, D. E. Shea, M. Khan, A. Bahinski, G. A. Hamilton, and D. E. Ingber, "Microfabrication of human organs-on-chips," *Nature Protocols*, vol. 8, no. 11, pp. 2135–2157, Nov. 2013.

[16] S. Peel, A. M. Corrigan, B. Ehrhardt, K.-J. Jang, P. Caetano-Pinto, M. Boeckeler, J. E. Rubins, K. Kodella, D. B. Petropolis, J. Ronxhi, G. Kulkarni, A. J. Foster, D. Williams, G. A. Hamilton, and L. Ewart, "Introducing an automated high content confocal imaging approach for Organs-on-Chips," *Lab on a Chip*, vol. 19, no. 3, pp. 410–421, 2019.

[17] A. Jain, R. Barrile, A. van der Meer, A. Mammoto, T. Mammoto, K. De Ceunynck, O. Aisiku, M. Otieno, C. Louden, G. Hamilton, R. Flaumenhaft, and D. Ingber, "Primary Human Lung Alveolus-on-a-chip Model of Intravascular Thrombosis for Assessment of Therapeutics," *Clinical Pharmacology & Therapeutics*, vol. 103, no. 2, pp. 332–340, Feb. 2018.

[18] J. Kuhnl, T. P. Tao, K. Brandmair, S. Gerlach, T. Rings, U. Muller-Vieira, J. Przibilla, C. Genies, C. Jaques-Jamin, A. Schepky, U. Marx, N. J. Hewitt, and I. Maschmeyer, "Characterization of application scenario-dependent pharmacokinetics and pharmacodynamic properties of permethrin and hyperforin in a dynamic skin and liver multi-organ-chip model," *Toxicology*, vol. 448, p. 152637, Jan. 2021.

[19] L. A. Low and D. A. Tagle, "Organs-on-chips: Progress, challenges, and future directions," *Experimental Biology and Medicine*, vol. 242, no. 16, pp. 1573–1578, Oct. 2017.

[20] J. P. Wikswo, F. E. Block, D. E. Cliffel, C. R. Goodwin, C. C. Marasco, D. A. Markov, D. L. McLean, J. A. McLean, J. R. McKenzie, R. S. Reiserer, P. C. Samson, D. K. Schaffer, K. T. Seale, and S. D. Sherrod, "Engineering Challenges for Instrumenting and Controlling Integrated Organ-on-Chip Systems," *IEEE Transactions on Biomedical Engineering*, vol. 60, no. 3, pp. 682–690, Mar. 2013.

[21] S. M. Park, S. Eom, H. Hong, J. Yoon, S. J. Lee, B. C. Kim, H. W. Kim, and D. S. Kim, "Reconstruction of in vivo-like in vitro model: Enabling technologies of microfluidic systems for dynamic biochemical/mechanical stimuli," *Microelectronic Engineering*, vol. 203-204, pp. 6–24, Jan. 2019.

[22] K. A. Homan, N. Gupta, K. T. Kroll, D. B. Kolesky, M. Skylar-Scott, T. Miyoshi, D. Mau, M. T. Valerius, T. Ferrante, J. V. Bonventre, J. A. Lewis, and R. Morizane, "Flow-enhanced vascularization and maturation of kidney organoids in vitro," *Nature Methods*, vol. 16, no. 3, pp. 255–262, Mar. 2019.

[23] Y. Yang, P. Fathi, G. Holland, D. Pan, N. S. Wang, and M. B. Esch, "Pumpless microfluidic devices for generating healthy and diseased endothelia," *Lab on a Chip*, vol. 19, no. 19, pp. 3212–3219, 2019.

[24] F. Yu, R. Deng, W. Hao Tong, L. Huan, N. Chan Way, A. IslamBadhan, C. Iliescu, and H. Yu, "A perfusion incubator liver chip for 3D cell culture with application on chronic hepatotoxicity testing," *Scientific Reports*, vol. 7, no. 1, p. 14528, Dec. 2017.

[25] C. K. Byun, K. Abi-Samra, Y.-K. Cho, and S. Takayama, "Pumps for microfluidic cell culture: Microfluidics and Miniaturization," *Electrophoresis*, vol. 35, no. 2-3, pp. 245–257, Feb. 2014.

[26] Y. J. Heo, J. Kang, M. J. Kim, and W. K. Chung, "Tuning-free controller to accurately regulate flow rates in a microfluidic network," *Scientific Reports*, vol. 6, no. 1, p. 23273, Sep. 2016.

[27] Y. Temiz, R. D. Lovchik, G. V. Kaigala, and E. Delamarche, "Lab-on-a-chip devices: How to close and plug the lab?" *Microelectronic Engineering*, vol. 132, pp. 156–175, Jan. 2015.

[28] S. Celik-Uzuner and U. Uzuner, "An Extensive Method for Maintenance of Sterility in Mammalian Cell Culture Laboratory Routine," *Challenges*, vol. 8, no. 2, p. 26, Oct. 2017.

[29] W. Lawi, C. Wiita, S. T. Snyder, F. Wei, D. Wong, P. K. Wong, J. C. Liao, D. Haake, and V. Gau, "A Microfluidic Cartridge System for Multiplexed Clinical Analysis," *Journal of the Association for Laboratory Automation*, vol. 14, no. 6, pp. 407–412, Dec. 2009.

[30] S.-B. Huang, M.-H. Wu, S.-S. Wang, and G.-B. Lee, "Microfluidic cell culture chip with multiplexed medium delivery and efficient cell/scaffold loading mechanisms for high-throughput perfusion 3-dimensional cell culture-based assays," *Biomedical Microdevices*, vol. 13, no. 3, pp. 415–430, Jun. 2011.

[31] D. R. Hunt, K. C. Klett, S. Mascharak, H. Y. Wang, D. Gong, J. Lou, X. Li, P. C. Cai, R. A. Suhar, J. Y. Co, B. L. LeSavage, A. A. Foster, Y. Guan, M. R. Amieva, G. Peltz, Y. Xia, C. J. Kuo, and S. C. Heilshorn, "Engineered Matrices Enable the Culture of Human Patient-Derived Intestinal Organoids," *Advanced Science*, p. 2004705, Mar. 2021.

[32] M. W. Toepke and D. J. Beebe, "PDMS absorption of small molecules and consequences in microfluidic applications," *Lab on a Chip*, vol. 6, no. 12, p. 1484, 2006.

[33] P. M. van Midwoud, A. Janse, M. T. Merema, G. M. M. Groothuis, and E. Verpoorte, "Comparison of Biocompatibility and Adsorption Properties of Different Plastics for Advanced Microfluidic Cell and Tissue Culture Models," *Analytical Chemistry*, vol. 84, no. 9, pp. 3938–3944, May 2012.

[34] Y. S. Shin, K. Cho, S. H. Lim, S. Chung, S.-J. Park, C. Chung, D.-C. Han, and J. K. Chang, "PDMS-based micro PCR chip with Parylene coating," *Journal of Micromechanics and Microengineering*, vol. 13, no. 5, pp. 768–774, Sep. 2003.

[35] S. M. Longman and G. C. Buehring, "A method for measuring steroid adsorption to tissue culture plasticware," *Journal of Tissue Culture Methods*, vol. 10, no. 4, pp. 253–255, Dec. 1986.

[36] R. G. Chapman, E. Ostuni, M. N. Liang, G. Meluleni, E. Kim, L. Yan, G. Pier, H. S. Warren, and G. M. Whitesides, "Polymeric Thin Films That Resist the Adsorption of Proteins and the Adhesion of Bacteria," *Langmuir*, vol. 17, no. 4, pp. 1225–1233, Feb. 2001.

[37] K. Domansky, J. D. Sliz, N. Wen, C. Hinojosa, G. Thompson, J. P. Fraser, T. Hamkins-Indik, G. A. Hamilton, D. Levner, and D. E. Ingber, "SEBS elastomers for fabrication of microfluidic devices with reduced drug absorption by injection molding and extrusion," *Microfluidics and Nanofluidics*, vol. 21, no. 6, p. 107, Jun. 2017.

[38] F. Mast, J. A. R. D. Hoschtitzky, C. A. Van Blitterswijk, and H. A. Huysmans, "In vitro biocompatibility of EPM and EPDM rubbers," *Journal of Materials Science: Materials in Medicine*, vol. 8, no. 1, pp. 5–9, 1997.

[39] I. R. G. Ogilvie, V. J. Sieben, B. Cortese, M. C. Mowlem, and H. Morgan, "Chemically resistant microfluidic valves from Viton membranes bonded to COC and PMMA," *Lab on a Chip*, vol. 11, no. 14, p. 2455, 2011.

[40] M. Berenguel-Alonso, M. Sabes-Alsina, R. Morato, O. Ymbern, L. Rodriguez-Vazquez, O. Tallo-Parra, J. Alonso-Chamarro, M. Puyol, and M. Lopez-Bejar, "Rapid Prototyping of a Cyclic Olefin Copolymer Microfluidic Device for Automated Oocyte Culturing," p. 11.

[41] S. Roy, T. Das, and C. Y. Yue, "High Performance of Cyclic Olefin Copolymer-Based Capillary Electrophoretic Chips," *ACS Applied Materials & Interfaces*, vol. 5, no. 12, pp. 5683–5689, Jun. 2013.

[42] G. D. Bittner, C. Z. Yang, and M. A. Stoner, "Estrogenic chemicals often leach from BPA-free plastic products that are replacements for BPA-containing polycarbonate products," *Environmental Health*, vol. 13, no. 1, p. 41, Dec. 2014.

[43] R. Fujita, S. Nagatoishi, S. Adachi, H. Nishioka, H. Ninomiya, T. Kaya, M. Takai, T. Arakawa, and K. Tsumoto, "Control of Protein Adsorption to Cyclo Olefin Polymer by the Hofmeister Effect," *Journal of Pharmaceutical Sciences*, vol. 108, no. 5, pp. 1686–1691, May 2019.

[44] T. B. Stachowiak, D. A. Mair, T. G. Holden, L. J. Lee, F. Svec, and J. M. J. Frechet, "Hydrophilic surface modification of cyclic olefin copolymer microfluidic chips using sequential photografting," *Journal of Separation Science*, vol. 30, no. 7, pp. 1088–1093, May 2007.

[45] K. Perez-Toralla, J. Champ, M. R. Mohamadi, O. Braun, L. Malaquin, J.-L. Viovy, and S. Descroix, "New non-covalent strategies for stable surface treatment of thermoplastic chips," *Lab on a Chip*, vol. 13, no. 22, p. 4409, 2013.

[46] E. Kjaer Unmack Larsen and N. B. Larsen, "One-step polymer surface modification for minimizing drug, protein, and DNA adsorption in microanalytical systems," *Lab Chip*, vol. 13, no. 4, pp. 669–675, 2013.

[47] C.-W. Tsao and D. L. DeVoe, "Bonding of thermoplastic polymer microfluidics," *Microfluidics and Nanofluidics*, vol. 6, no. 1, pp. 1–16, Jan. 2009.

[48] H. Yeh, "Overview of welding methods for medical plastics," in *Joining and Assembly of Medical Materials and Devices*. Elsevier, 2013, pp. 261–298e.

[49] E. Gleichweit, C. Baumgartner, R. Diethardt, A. Murer, W. Sallegger, D. Werkl, and S. KÃűstler, "UV/Ozone Surface Treatment for Bonding of Elastomeric COC-Based Microfluidic Devices," *Proceedings*, vol. 2, no. 13, p. 943, Dec. 2018.

[50] H. S., L. T., S. S., M. S., and Z. R., "Solvent Bonding of a Drug Delivery Device by Using Hansen Solubility Parameters," in *Proceedings of the 8th International Conference on Multi-Material Micro Manufacture*. Research Publishing Services, 2011, pp. 38–41.

[51] N. Keller, T. M. Nargang, M. Runck, F. Kotz, A. Striegel, K. Sachsenheimer, D. Klemm, K. LÃď nge, M. Worgull, C. Richter, D. Helmer, and B. E. Rapp,

"Tacky cyclic olefin copolymer: a biocompatible bonding technique for the fabrication of microfluidic channels in COC," *Lab on a Chip*, vol. 16, no. 9, pp. 1561–1564, 2016.

[52] A. M. D. Wan, A. Sadri, and E. W. K. Young, "Liquid phase solvent bonding of plastic microfluidic devices assisted by retention grooves," *Lab on a Chip*, vol. 15, no. 18, pp. 3785–3792, 2015.

[53] A. B. Azouz, S. Murphy, S. Karazi, M. VÃązquez, and D. Brabazon, "Fast Fabrication Process of Microfluidic Devices Based on Cyclic Olefin Copolymer," *Materials and Manufacturing Processes*, vol. 29, no. 2, pp. 93–99, Feb. 2014.

[54] H. Zhang, X. Liu, T. Li, and X. Han, "Miscible Organic Solvents Soak Bonding Method Use in a PMMA Multilayer Microfluidic Device," *Micromachines*, vol. 5, no. 4, pp. 1416–1428, Dec. 2014.

[55] K. T. L. Trinh, Q. N. Pham, and N. Y. Lee, "Clog-free and reliable solvent bonding of poly(methyl methacrylate) microdevice mediated by eco-friendly acetic acid at room temperature and its application for polymerase chain reaction and human cell culture," *Sensors and Actuators B: Chemical*, vol. 282, pp. 1008–1017, Mar. 2019.

[56] D. A. Mair, M. Rolandi, M. Snauko, R. Noroski, F. Svec, and J. M. J. FrÃľchet, "Room-Temperature Bonding for Plastic High-Pressure Microfluidic Chips," *Analytical Chemistry*, vol. 79, no. 13, pp. 5097–5102, Jul. 2007.

[57] Y. Zhang, K. Gao, and Y. Fan, "Application of a new UV curable adhesive for rapid bonding in thermoplastic-based microfluidics," *Micro & Nano Letters*, vol. 14, no. 2, pp. 211–214, Feb. 2019.

[58] M. Serra, I. Pereiro, A. Yamada, J.-L. Viovy, S. Descroix, and D. Ferraro, "A simple and low-cost chip bonding solution for high pressure, high temperature and biological applications," *Lab on a Chip*, vol. 17, no. 4, pp. 629–634, 2017.

[59] S. Senkbeil, "Design and Fabrication of Polymer-based Lab-on-a-Chip Devices Towards Applications in Food and Environmental Analysis," p. 164.

[60] S. Roy, C. Yue, Z. Wang, and L. Anand, "Thermal bonding of microfluidic devices: Factors that affect interfacial strength of similar and dissimilar cyclic olefin copolymers," *Sensors and Actuators B: Chemical*, vol. 161, no. 1, pp. 1067–1073, Jan. 2012.

[61] T. Park, I.-H. Song, D. S. Park, B. H. You, and M. C. Murphy, "Thermal bonding of polymer microdevices using a pressure-assisted boiling point control system," *16th International Conference on Miniaturized Systems for Chemistry and Life Sciences*, pp. 689–691, 2012.

[62] S. Yu, S. P. Ng, Z. Wang, C. L. Tham, and Y. C. Soh, "Thermal bonding of thermoplastic elastomer film to PMMA for microfluidic applications," *Surface and Coatings Technology*, vol. 320, pp. 437–440, Jun. 2017.

[63] W. Inman, K. Domansky, J. Serdy, B. Owens, D. Trumper, and L. G. Griffith, "Design, modeling and fabrication of a constant flow pneumatic micropump," *Journal of Micromechanics and Microengineering*, vol. 17, no. 5, pp. 891–899, May 2007.

[64] J. Zhang, Y.-J. Huang, J. Y. Yoon, J. Kemmitt, C. Wright, K. Schneider, P. Sphabmixay, V. Hernandez-Gordillo, S. J. Holcomb, B. Bhushan, G. Rohatgi, K. Benton, D. Carpenter, J. C. Kester, G. Eng, D. T. Breault, O. Yilmaz, M. Taketani, C. A. Voigt, R. L. Carrier, D. L. Trumper, and L. G. Griffith, "Primary Human Colonic Mucosal Barrier Crosstalk with Super Oxygen-Sensitive Faecalibacterium prausnitzii in Continuous Culture," *Med*, vol. 2, no. 1, pp. 74–98.e9, Jan. 2021.

[65] F. Abhari, H. Jaafar, and N. A. Yunus, "A Comprehensive Study of Micropumps Technologies," *Int. J. Electrochem. Sci.*, vol. 7, p. 16, 2012.

[66] S. Mohith, P. N. Karanth, and S. Kulkarni, "Recent trends in mechanical micropumps and their applications: A review," *Mechatronics*, vol. 60, pp. 34–55, Jun. 2019.

[67] A. K. Au, H. Lai, B. R. Utela, and A. Folch, "Microvalves and Micropumps for BioMEMS," *Micromachines*, vol. 2, no. 2, pp. 179–220, May 2011.

[68] Y.-N. Wang and L.-M. Fu, "Micropumps and biomedical applications âĂŞ A review," *Microelectronic Engineering*, vol. 195, pp. 121–138, Aug. 2018.

[69] D. W. Dissanayake, S. F. Al-Sarawi, T.-F. Lu, and D. Abbott, "Design and characterisation of micro-diaphragm for low power drug delivery applications," M. Ahmadian, Ed., San Diego, California, Mar. 2008, p. 69282P.

[70] A. Kumar, R. Srivastava, and P. Student, "Modeling and Simulation of a Micropump Chip using Dielectric Elastomer," vol. 2, no. 2, p. 7, 2013.

[71] E. Roy, "Thermoplastic elastomers for microfluidic valving and mixing, toward high- throughput fabrication of multilayer devices," p. 3.

[72] P. Gu, T. Nishida, and Z. H. Fan, "The use of polyurethane as an elastomer in thermoplastic microfluidic devices and the study of its creep properties: Microfluidics and Miniaturization," *Electrophoresis*, vol. 35, no. 2-3, pp. 289–297, Feb. 2014.

[73] J. Kim, M. Kang, E. C. Jensen, and R. A. Mathies, "Lifting Gate Polydimethylsiloxane Microvalves and Pumps for Microfluidic Control," *Analytical Chemistry*, vol. 84, no. 4, pp. 2067–2071, Feb. 2012.

[74] A. Pourmand, S. A. M. Shaegh, H. B. Ghavifekr, E. Najafi Aghdam, M. R. Dokmeci, A. Khademhosseini, and Y. S. Zhang, "Fabrication of whole-thermoplastic normally closed microvalve, micro check valve, and micropump," *Sensors and Actuators B: Chemical*, vol. 262, pp. 625–636, Jun. 2018.

[75] C. MÃűhl, C. Thomas, and U. Hesse, "An Investigation Into The Dynamics Of Self-Acting Compressor Valves," p. 10, 2016.

[76] S. K. Chimakurthi, S. Reuss, M. Tooley, and S. Scampoli, "ANSYS Workbench System Coupling: a state-of-the-art computational framework for analyzing multiphysics problems," *Engineering with Computers*, vol. 34, no. 2, pp. 385–411, Apr. 2018.

[77] A. M. Stockton, M. F. Mora, M. L. Cable, and P. A. Willis, "Design rules and operational optimization for rapid, contamination-free microfluidic transfer using monolithic membrane valves," *Sensors and Actuators B: Chemical*, vol. 177, pp. 668–675, Feb. 2013.

[78] L. R. Soenksen, T. Kassis, M. Noh, L. G. Griffith, and D. L. Trumper, "Closed-loop feedback control for microfluidic systems through automated capacitive fluid height sensing," *Lab on a Chip*, vol. 18, no. 6, pp. 902–914, 2018.

[79] D.-W. Lee and Y.-S. Choi, "A novel pressure sensor with a PDMS diaphragm," *Microelectronic Engineering*, vol. 85, no. 5-6, pp. 1054–1058, May 2008.

[80] M.-C. Liu, H.-C. Shih, J.-G. Wu, T.-W. Weng, C.-Y. Wu, J.-C. Lu, and Y.-C. Tung, "Electrofluidic pressure sensor embedded microfluidic device: a study of endothelial cells under hydrostatic pressure and shear stress combinations," *Lab on a Chip*, vol. 13, no. 9, p. 1743, 2013.

[81] X. Wang, D. T. T. Phan, D. Zhao, S. C. George, C. C. W. Hughes, and A. P. Lee, "An on-chip microfluidic pressure regulator that facilitates reproducible loading of cells and hydrogels into microphysiological system platforms," *Lab on a Chip*, vol. 16, no. 5, pp. 868–876, 2016.

[82] X. Liu and S. Li, "An Electromagnetic Microvalve for Pneumatic Control of Microfluidic Systems," *Journal of Laboratory Automation*, vol. 19, no. 5, pp. 444–453, Oct. 2014.

[83] K. Brower, R. R. Puccinelli, C. J. Markin, T. C. Shimko, S. A. Longwell, B. Cruz, R. Gomez-Sjoberg, and P. M. Fordyce, "An open-source, programmable pneumatic setup for operation and automated control of single- and multi-layer microfluidic devices," *HardwareX*, vol. 3, pp. 117–134, Apr. 2018.

[84] D. C. Leslie, C. J. Easley, E. Seker, J. M. Karlinsey, M. Utz, M. R. Begley, and J. P. Landers, "Frequency-specific flow control in microfluidic circuits with passive elastomeric features," *Nature Physics*, vol. 5, no. 3, pp. 231–235, Mar. 2009.

[85] Zhang and Zhang, "Microfluidic Passive Flow Regulatory Device with an Integrated Check Valve for Enhanced Flow Control," *Micromachines*, vol. 10, no. 10, p. 653, Sep. 2019.

[86] "Extremely simple pressure regulator computation studies," *Chemical Engineering Journal,*, vol. 155, no. 1-2.

[87] N. Zafer and G. R. Luecke, "Stability of gas pressure regulators," *Applied Mathematical Modelling*, vol. 32, no. 1, pp. 61–82, Jan. 2008.

[88] G. S. Offeddu, J. C. Serrano, S. W. Chen, S. E. Shelton, Y. Shin, M. Floryan, and R. D. Kamm, "Microheart: A microfluidic pump for functional vascular culture in microphysiological systems," *Journal of Biomechanics*, vol. 119, p. 110330, Apr. 2021.

[89] B. Yang and Q. Lin, "A Compliance-Based Microflow Stabilizer," *Journal of Microelectromechanical Systems*, vol. 18, no. 3, pp. 539–546, Jun. 2009.

[90] E. Hobbs, "Low-Power Portable Microfluidic Delivery System," PhD Thesis, University of California, Berkeley, 2004.

[91] M. Richter, R. Linnemann, and P. Woias, "Robust design of gas and liquid micropumps," *Sensors and Actuators A: Physical*, vol. 68, no. 1-3, pp. 480–486, Jun. 1998.

[92] "Manifold Assemblies Simplifying Valve Installations," IMI Precision Engineering, Tech. Rep., 03 2018.

[93] T. W. Astle, "Microplate Standardization," *Molecules*, vol. 1, no. 9, pp. 106–113, Jan. 1997.

[94] R. Lamonte and D. Mcnally, "Cyclic olefin copolymers," *Advanced Materials and Processes*, vol. 159, pp. 33–36, 03 2001.

[95] P. S. Nunes, P. D. Ohlsson, O. Ordeig, and J. P. Kutter, "Cyclic olefin polymers: emerging materials for lab-on-a-chip applications," *Microfluidics and Nanofluidics*, vol. 9, no. 2-3, pp. 145–161, Aug. 2010.

[96] G. Khanarian, "Optical properties of cyclic olefin copolymers," *Optical Engineering*, vol. 40, no. 6, p. 1024, Jun. 2001.

[97] *TOPAS^{TM} 6015S-04 Technical Datasheet*, TOPAS Advanced Polymers, 2019.

[98] "Topas coc for pan barex replacement." TOPAS Advanced Polymers, 2015, p. 22.

[99] E. Niedzielska and A. Masek, "Polymer materials with controlled degradation time," *E3S Web of Conferences*, vol. 44, p. 122, 2018.

[100] P. D. Tatarka, T. M. Kneale, and B. Canale-Schmidt, "Transparent, flexible products made with partially crystalline cycloolefin elastomer," Jan 2012.

[101] *TOPAS^{TM} Elastomer E-140 Technical Datasheet*, TOPAS Advanced Polymers, 2019.

[102] J. Steigert, S. Haeberle, T. Brenner, C. Muller, C. P. Steinert, P. Koltay, N. Gottschlich, H. Reinecke, J. Ruhe, R. Zengerle, and J. Ducree, "Rapid prototyping of microfluidic chips in COC," *Journal of Micromechanics and Microengineering*, vol. 17, no. 2, pp. 333–341, Feb. 2007.

[103] H.-T. Nguyen, H. Thach, E. Roy, K. Huynh, and C. Perrault, "Low-Cost, Accessible Fabrication Methods for Microfluidics Research in Low-Resource Settings," *Micromachines*, vol. 9, no. 9, p. 461, Sep. 2018.

[104] M. M. Hossain and T. Rahman, "Low Cost Micro Milling Machine for Prototyping Plastic Microfluidic Devices," *Proceedings*, vol. 2, no. 13, p. 707, Dec. 2018.

[105] A. Lashkaripour, R. Silva, and D. Densmore, "Desktop micromilled microfluidics," *Microfluidics and Nanofluidics*, vol. 22, no. 3, p. 31, Mar. 2018.

[106] D. J. Guckenberger, T. E. de Groot, A. M. D. Wan, D. J. Beebe, and E. W. K. Young, "Micromilling: a method for ultra-rapid prototyping of plastic microfluidic devices," *Lab on a Chip*, vol. 15, no. 11, pp. 2364–2378, 2015.

[107] *Nitto (Permacel) P-02 Product Datasheet*, Nitto, Inc., 2016.

[108] P. K. Yuen and V. N. Goral, "Low-cost rapid prototyping of flexible microfluidic devices using a desktop digital craft cutter," *Lab Chip*, vol. 10, no. 3, pp. 384–387, 2010.

[109] Z. Strike, K. Ghofrani, and C. Backhouse, "CO2 Laser-Based Rapid Prototyping of Micropumps," *Micromachines*, vol. 9, no. 5, p. 215, May 2018.

[110] M. O. Helmy, A. M. Fath El-Bab, and H. El-Hofy, "Elimination of Clogging in PMMA Microchannels Using Water Assisted CO_2 Laser Micromachining," *Applied Mechanics and Materials*, vol. 799-800, pp. 407–412, Oct. 2015.

[111] O. H. Yeoh, "Some Forms of the Strain Energy Function for Rubber," *Rubber Chemistry and Technology*, vol. 66, no. 5, pp. 754–771, Nov. 1993.

[112] *LPG10-1000 Liquid Flow Sensor Product Datasheet*, Sensirion AG, January 2019.

[113] S. W. Inman, "Development of a High Throughput 3D Perfused Liver Tissue Bioreactor," PhD Thesis, Massachusettes Institute of Technology, 2006.

[114] C. Frantz, K. M. Stewart, and V. M. Weaver, "The extracellular matrix at a glance," *Journal of Cell Science*, vol. 123, no. 24, pp. 4195–4200, Dec. 2010.

[115] R. Dosh, A. Essa, N. Jordan-Mahy, C. Sammon, and C. Le Maitre, "Use of hydrogel scaffolds to develop an in vitro 3D culture model of human intestinal epithelium," *Acta Biomaterialia*, vol. 62, pp. 128–143, Oct. 2017.

[116] X. Zhang, L. Li, and C. Luo, "Gel integration for microfluidic applications," *Lab on a Chip*, vol. 16, no. 10, pp. 1757–1776, 2016.

[117] P. Vulto, S. Podszun, P. Meyer, C. Hermann, A. Manz, and G. A. Urban, "Phaseguides: a paradigm shift in microfluidic priming and emptying," *Lab on a Chip*, vol. 11, no. 9, p. 1596, 2011.

[118] B. Gumuscu and J. C. T. Eijkel, "Capillary Pinning Assisted Patterning of Cell-Laden Hydrogel Microarrays in Microchips," in *Cell-Based Microarrays*, P. Ertl and M. Rothbauer, Eds. New York, NY: Springer New York, 2018, vol. 1771, pp. 225–238, series Title: Methods in Molecular Biology.

[119] M. Tenje, F. Cantoni, A. M. Porras Hernandez, S. S. Searle, S. Johansson, L. Barbe, M. Antfolk, and H. Pohlit, "A practical guide to microfabrication and patterning of hydrogels for biomimetic cell culture scaffolds," *Organs-on-a-Chip*, vol. 2, Dec. 2020.

[120] D. T. T. Phan, X. Wang, B. M. Craver, A. Sobrino, D. Zhao, J. C. Chen, L. Y. N. Lee, S. C. George, A. P. Lee, and C. C. W. Hughes, "A vascularized and perfused organ-on-a-chip platform for large-scale drug screening applications," *Lab on a Chip*, vol. 17, no. 3, pp. 511–520, 2017.

[121] J. Patrick, B. Krull, M. Garg, C. Mangun, J. Moore, N. Sottos, and S. White, "Robust sacrificial polymer templates for 3D interconnected microvasculature in fiber-reinforced composites," *Composites Part A: Applied Science and Manufacturing*, vol. 100, pp. 361–370, Sep. 2017.

[122] J. D. McNulty, C. Marti-Figueroa, F. Seipel, J. Z. Plantz, T. Ellingham, L. J. Duddleston, S. Goris, B. L. Cox, T. A. Osswald, L.-S. Turng, and R. S. Ashton, "Micro-injection molded, poly(vinyl alcohol)-calcium salt templates for precise customization of 3D hydrogel internal architecture," *Acta Biomaterialia*, vol. 95, pp. 258–268, Sep. 2019.

[123] S. Ji, E. Almeida, and M. Guvendiren, "3D bioprinting of complex channels within cell-laden hydrogels," *Acta Biomaterialia*, vol. 95, pp. 214–224, Sep. 2019.

[124] C.-L. E. Helm, M. E. Fleury, A. H. Zisch, F. Boschetti, and M. A. Swartz, "Synergy between interstitial flow and VEGF directs capillary morphogenesis in vitro through a gradient amplification mechanism," *Proceedings of the National Academy of Sciences*, vol. 102, no. 44, pp. 15 779–15 784, Nov. 2005.

[125] K. T. Morin, J. L. Dries-Devlin, and R. T. Tranquillo, "Engineered Microvessels with Strong Alignment and High Lumen Density Via Cell-Induced Fibrin Gel Compaction and Interstitial Flow," *Tissue Engineering Part A*, Nov. 2013.

[126] Y.-H. Hsu, M. L. Moya, P. Abiri, C. C. Hughes, S. C. George, and A. P. Lee, "Full range physiological mass transport control in 3D tissue cultures," *Lab Chip*, vol. 13, no. 1, pp. 81–89, 2013.

[127] M. L. Moya, Y.-H. Hsu, A. P. Lee, C. C. Hughes, and S. C. George, "*In Vitro* Perfused Human Capillary Networks," *Tissue Engineering Part C: Methods*, vol. 19, no. 9, pp. 730–737, Sep. 2013.

[128] J. Tien, L. Li, O. Ozsun, and K. L. Ekinci, "Dynamics of Interstitial Fluid Pressure in Extracellular Matrix Hydrogels in Microfluidic Devices," *Journal of Biomechanical Engineering*, vol. 137, no. 9, p. 091009, Sep. 2015.

[129] C. Hajal, L. Ibrahim, J. C. Serrano, G. S. Offeddu, and R. D. Kamm, "The effects of luminal and trans-endothelial fluid flows on the extravasation and tissue invasion of tumor cells in a 3D in vitro microvascular platform," *Biomaterials*, vol. 265, p. 120470, Jan. 2021.

[130] C. D. Edington, W. L. K. Chen, E. Geishecker, T. Kassis, L. R. Soenksen, B. M. Bhushan, D. Freake, J. Kirschner, C. Maass, N. Tsamandouras, J. Valdez, C. D. Cook, T. Parent, S. Snyder, J. Yu, E. Suter, M. Shockley, J. Velazquez, J. J. Velazquez, L. Stockdale, J. P. Papps, I. Lee, N. Vann, M. Gamboa, M. E. LaBarge, Z. Zhong, X. Wang, L. A. Boyer, D. A. Lauffenburger, R. L. Carrier, C. Communal, S. R. Tannenbaum, C. L. Stokes, D. J. Hughes, G. Rohatgi, D. L. Trumper, M. Cirit, and L. G. Griffith, "Interconnected Microphysiological Systems for Quantitative Biology and Pharmacology Studies," *Scientific Reports*, vol. 8, no. 1, p. 4530, Dec. 2018.

[131] X. Meng, Y. Zhu, Y. Chen, Y. Lu, Y. Xu, and J. Cheng, "Conditional siphon priming for multi-step assays on centrifugal microfluidic platforms," *Sensors and Actuators B: Chemical*, vol. 242, pp. 710–717, Apr. 2017.

[132] R. Burger, D. J. Kinahan, H. Cayron, N. Reis, J. Fonseca, and J. Ducree, "Siphon-Induced Droplet Break-Off for Enhanced Mixing on a Centrifugal Platform," *Inventions*, vol. 5, no. 1.

[133] K. T. Morin and R. T. Tranquillo, "In vitro models of angiogenesis and vasculogenesis in fibrin gel," *Experimental Cell Research*, vol. 319, no. 16, pp. 2409–2417, Oct. 2013.

[134] R. Sudo, S. Chung, I. K. Zervantonakis, V. Vickerman, Y. Toshimitsu, L. G. Griffith, and R. D. Kamm, "Transport mediated angiogenesis in 3D epithelial coculture," *The FASEB Journal*, vol. 23, no. 7, pp. 2155–2164, Jul. 2009.

[135] V. S. Shirure, A. Lezia, A. Tao, L. F. Alonzo, and S. C. George, "Low levels of physiological interstitial flow eliminate morphogen gradients and guide angiogenesis," *Angiogenesis*, vol. 20, no. 4, pp. 493–504, Nov. 2017.

[136] C. J. Ochs, J. Kasuya, A. Pavesi, and R. D. Kamm, "Oxygen levels in thermoplastic microfluidic devices during cell culture," *Lab Chip*, vol. 14, no. 3, pp. 459–462, 2014.

[137] A. Poloznikov, "In vitro and in silico liver models: Current trends, challenges and opportunities," *ALTEX*, pp. 397–412, 2018.

[138] M. Busek, S. Grunzner, T. Steege, U. Klotzbach, and F. Sonntag, "Hypoxia-on-a-chip: Generating hypoxic conditions in microfluidic cell culture systems," *Current Directions in Biomedical Engineering*, vol. 2, no. 1, pp. 71–75, Sep. 2016.

[139] M. Busek, S. Grunzner, T. Steege, F. Schmieder, U. Klotzbach, and F. Sonntag, "Design, characterization, and modeling of microcirculation systems with integrated oxygenators," *Journal of Sensors and Sensor Systems*, vol. 5, no. 1, pp. 221–228, Jun. 2016.

[140] P. Kjeldsen, "Evaluation of gas diffusion through plastic materials used in experimental and sampling equipment," *Water Research*, vol. 27, no. 1, pp. 121–131, Jan. 1993.

[141] J. Dobson and M. Taylor, "The permeability of gases through PTFE and other membranes at 25C," *Electrochimica Acta*, vol. 31, no. 2, pp. 231–233, Feb. 1986.

[142] T. Steege, M. Busek, S. Grunzner, A. F. Lasagni, and F. Sonntag, "Closed-loop control system for well-defined oxygen supply in micro-physiological systems," *Current Directions in Biomedical Engineering*, vol. 3, no. 2, pp. 363–366, Sep. 2017.

[143] C. Schmittlein, R. J. Meier, L. Sauer, G. Liebsch, and J. Wegener, "Image-Based Monitoring of Oxygenation in Microfluidic Cell Culture: PreSens Precision Sensing describes how sensor foils can serve as growth substrates and deliver 2D readouts," *Genetic Engineering & Biotechnology News*, vol. 39, no. 1, pp. 87–89, Jan. 2019.